ABSTRACT

Title of dissertation: OPTICAL PROPERTIES OF
A QUANTUM-NOISE-LIMITED
PHASE-SENSITIVE AMPLIFIER

Tian Li, Doctor of Philosophy, 2017

Dissertation directed by: Dr. Paul D. Lett
Joint Quantum Institute,
National Institute of Standards and Technology
and University of Maryland

This dissertation is a summary of investigations on the optical properties of a quantum-noise-limited phase-sensitive amplifier (PSA). The PSA is implemented using four-wave mixing in hot ^{85}Rb vapor based on a double-Λ atomic scheme.

We experimentally demonstrate the ability of a PSA to pre-amplify quantum correlations in twin light beams produced by a phase-insensitive amplifier (PIA) before degradation due to loss and detector inefficiency. By including a PSA before loss, one is able to preserve the correlations as well as the two-mode squeezing level. We compare the results to simulations employing a simple quantum-mechanical model and find a good agreement.

We have demonstrated that the cross-correlation between the two modes of a bipartite entangled state can be advanced by propagation through a PIA acting as a fast-light medium. The extra noise added by the PIA has been speculated to be the mechanism that limits the advance of entanglement, preventing the mutual

information from traveling superluminally. As an extension of this phase-insensitive, gain-assisted, anomalous dispersion investigation, we explore the advance and delay of information transmitted through the PSA. We start with a two-mode squeezed state created by the PIA and measure the mutual information shared by the correlated quadratures. We then pass one of these two modes through a PSA and investigate the shift of the mutual information as a function of the PSA phase. In the case of a PSA, it is well known that no extra noise will be added to the quadrature with the correct input phase (e.g., the quadrature with the maximal amplification or the maximal deamplification). We find that there is no dispersion-like behavior at these two phases, however, the peak of mutual information could either be delayed or advanced at any other phase. We also observe an almost identical behavior when we input an amplitude modulated signal to the PSA. We are able to explain the physics of this "fast-and-slow-light" type of behavior utilizing a model assuming imbalanced gain on the positive and negative side bands. We obtain a good agreement between the experimental results and the theoretical simulations.

OPTICAL PROPERTIES OF A QUANTUM-NOISE-LIMITED PHASE-SENSITIVE AMPLIFIER

by

Tian Li

Dissertation submitted to the Faculty of the Graduate School of the
University of Maryland, College Park in partial fulfillment
of the requirements for the degree of
Doctor of Philosophy
2017

Advisory Committee:
Dr. Paul D. Lett, Chair/Advisor
Dr. Steven L. Rolston, Co-Advisor
Dr. William D. Phillips
Dr. Gretchen K. Campbell
Dr. Julius Goldhar

Dedicated to my lovely wife, Teng-er.

Acknowledgments

I am deeply appreciative of my thesis advisor Dr. Paul Lett who trained me to be an expert in the field of quantum optics. I am so thankful for his availability whenever I needed some advice on my research. His scientific insights always inspired me. I will always be grateful for his guidance and patience. It has been a great pleasure to work for him, and I feel so fortunate to have been his student.

I also would like to express my sincere gratitude to Professor Kevin Jones who is without a doubt one of the smartest and most generous people I have ever met. I feel a particularly large debt of gratitude towards him for the considerable time and effort he spent in helping me strengthen my intuition about a whole range of topics in physics through lengthy but fruitful conversations. His ideas always had great impacts on my research.

I also owe special gratitude to all current and former group members. I was so fortunate that during my graduate career, I had great opportunities to work with very talented and friendly group members. I have learned a great deal from all of them, especially Dr. Brian Anderson, whose solid set of research skills made himself my role model.

I also sincerely thank my Mom who encouraged me to study in the States after my college graduation. I wholeheartedly thank her for her support and encouragement.

Finally, I would like to thank my lovely wife, Teng-er, for being my greatest source of support and strength throughout these years. She has shown more patience

and trust in me than I would have ever thought possible. It is for this reason that this thesis is dedicated to her. I hope it makes her proud.

Table of Contents

List of Figures

xiv

List of Abbreviations

4WM	Four-Wave Mixing
PIA	Phase-Insensitive Amplifier
PSA	Phase-Sensitive Amplifier
SNR	Signal-to-Noise Ratio
NF	Noise Figure
EPR	Einstein-Podolsky-Rosen
PM	Phase Modulation
AM	Amplitude Modulation
HD	Homodyne Detection
BHD	Balanced Homodyne Detection
LO	Local Oscillator
FWHM	Full Width at Half Maximum
MI	Mutual Information

Chapter 1:   Introduction

As an experimental atomic, molecular and optical physics lab, we devote our-selves to investigating the interactions between light and atoms, in particular, the nonlinear optical properties induced by lasers in an atomic medium. As we learned from our college physics course, a dielectric medium responds to an external applied electric field linearly if the field strength is weak enough.[1] However, if the applied field strength is intense enough, it will excite atomic dipoles to oscillate nonlinearly. The radiated field from the oscillating dipoles will then interact with the applied field, and new fields with new frequencies will therefore be generated. Although nonlinear optical effects had been known as early as the nineteenth century (such as the Pockels and Kerr effects), only DC fields could be produced with enough intensity to reach the regime of nonlinear optical response. Due to this deficiency, nonlinear optics remained unexplored until the classic experiment by Franken and co-workers [1] in 1961 shortly after the demonstration of the first working laser by Maiman in 1960. They demonstrated second-harmonic generation in quartz with the use of a ruby laser. Since then the research of nonlinear optics is ever expanding thanks to the fact that intense applied fields can be easily obtained just by focusing

---

[1]Usually the external applied field is much weaker than the atom's internal field that holds the electrons, however, what is weak enough depends on specific circumstances.

laser beams.

In our lab, we use four-wave mixing, a nonlinear optical effect where interactions between two, or three fields produce two, or one new fields respectively. We use this interaction to create two types of optical amplifiers, i.e., phase-insensitive and phase-sensitive optical amplifiers. If the amplification has no dependence on the phase of the input field, it is referred to as phase-insensitive; if the amplification does depend on the phase of the input field, it is phase-sensitive. Our goal is to study and understand the optical properties of these two types of optical amplifiers both classically and quantum-mechanically.

1.1   Four-wave mixing

The traditional method of modeling an optical material's nonlinear response is to expand the induced polarization as a power series in the electric field strength [2–5]:

$$\vec{P} = \epsilon_o \chi^{(1)} \cdot \vec{E} + \epsilon_o \chi^{(2)} \cdot \vec{E}\vec{E} + \epsilon_o \chi^{(3)} \cdot \vec{E}\vec{E}\vec{E} + ... \tag{1.1}$$

The expansion coefficients $\chi^{(2)}$ and $\chi^{(3)}$ are known as nonlinear susceptibilities in analogy to classical linear electromagnetic theory. This method assumes that the higher order nonlinear susceptibilities grow progressively smaller so that the power series expansion converges to a finite polarization.

The third order nonlinear susceptibility $\chi^{(3)}$ is a fourth rank tensor and is responsible for the four-wave mixing (4WM) processes. In order to understand the 4WM process, a closer examination of the third order nonlinear polarization $\vec{P}^{(3)}$

2

must be made. One possible form of the polarization may be written as

$$P_i^{(3)}(\omega_4, \vec{r}) = \frac{1}{2}\epsilon_o \chi_{ijkl}^{(3)}(-\omega_4; \omega_1, \omega_2, -\omega_3) E_j(\omega_1) E_k(\omega_2) E_l^*(\omega_3) \times$$
$$\exp[i(\vec{k_1} + \vec{k_2} - \vec{k_3}) \cdot \vec{r} - i\omega_4 t] + c.c., \tag{1.2}$$

where i, j, k and l denote any x, y and z electric field component. ω_1, ω_2, ω_3 and ω_4 are the angular frequencies of the four fields and $\vec{k_1}$, $\vec{k_2}$ and $\vec{k_3}$ are the wave vectors of the three input fields. They are related by $k_i = n_i \omega_i / c$, $i = 1, 2, 3, 4$, where n_i is the index of refraction of the medium at frequency ω_i. This nonlinearity describes a coupling between four waves: three input fields and one generated field, each with its own direction of propagation, polarization, and frequency. This expression for the polarization immediately gives insight into the nature of the measured four-wave-mixing signals. Since the physical quantity that is measured by experiment is the field intensity, the observed signal will be proportional to $|\chi^{(3)}|^2$, the product of the three field intensities, and will also be related to a "phase mismatching" factor:

$$\delta\vec{k} \equiv \vec{k_1} + \vec{k_2} - \vec{k_3} - \vec{k_4}. \tag{1.3}$$

Equation (1.2) also implies that efficient coupling between the four waves, i.e., strong fourth field generation, will only occur when energy and momentum are both conserved [2]: $\omega_4 = \omega_1 + \omega_2 - \omega_3$ and $\vec{k_4} = \vec{k_1} + \vec{k_2} - \vec{k_3}$, i.e., $\delta\vec{k} = 0$. The condition that $\delta\vec{k} = 0$ is called "perfect phase matching". In Fig. 1.1, we show the satisfaction of these two conditions schematically.

The use of an atomic medium close to resonance to generate a high $\chi^{(3)}$ nonlin-
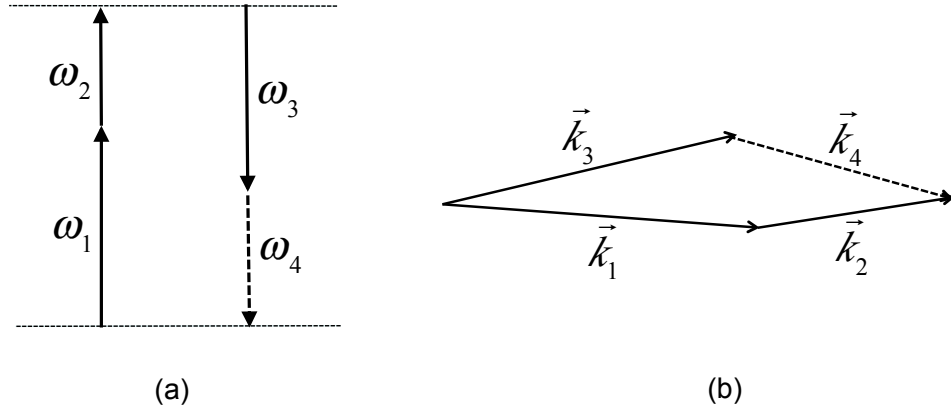
Figure 1.1: Energy (a) and momentum (b) conservation in the 4WM described by Eq. (1.2). ω_i and $\vec{k}_i$, $i = 1, 2, 3, 4$, are the frequencies and wave vectors of the four fields. They are related by $k_i = n_i\omega_i/c$, where n_i is the index of refraction of the medium at frequency ω_i.

earity has been first proposed in the classical regime in a few theoretical papers [6–9] where the atomic medium was described as a two-level system. Since then there have been different approaches to generate 4WM in more complicated level structures, such as the diamond configuration [10, 11] that consists of four levels: a single ground state, two intermediate states, and an upper state.

More recently there have been different theoretical descriptions in which the atomic systems are not described by a two-level atom, but by a 3-level single-Λ or a 4-level double-Λ atomic configuration (see Fig. 1.2), and where the production of 4WM has been studied [12, 13]. In our case, we are interested in using a double-Λ configuration to generate two 4WM processes: the phase-insensitive and the phase-sensitive amplification. Our approach is a consequence of the extraordinarily good results in [14] where the 4WM enabled by a double-Λ scheme has generated high levels of squeezed light, i.e., two beams with relative intensity fluctuations smaller than the shot-noise level.
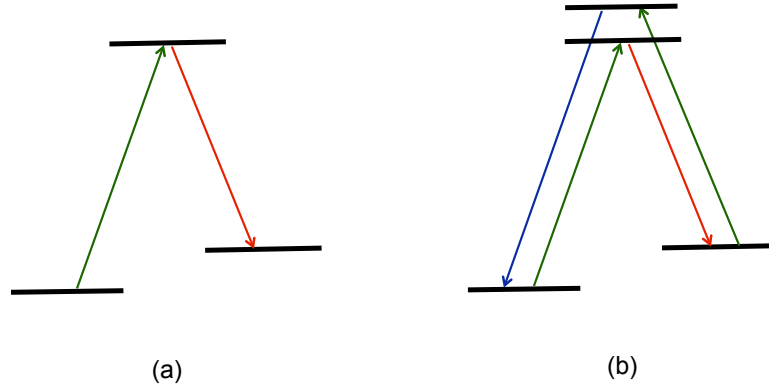
Figure 1.2: The 3-level single-Λ (a) and 4-level double-Λ (b) atomic configurations.
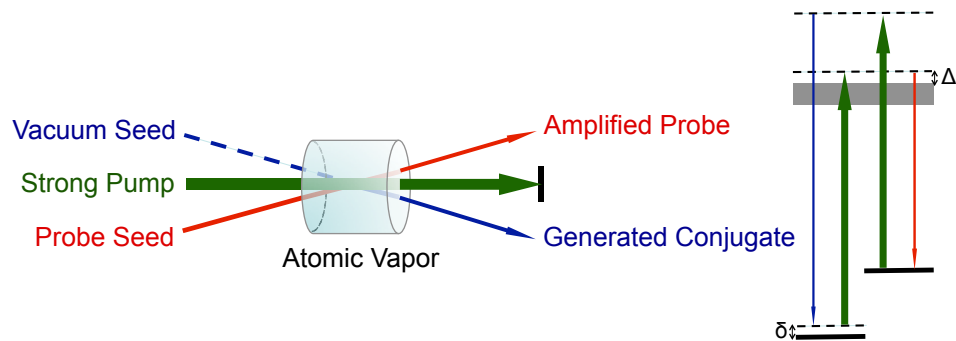
Figure 1.3: Sketch and energy diagram for the phase-insensitive amplification. One of the two input ports is seeded with probe light, the other one is seeded with only vacuum fluctuations. Due to the 4WM interactions, in addition to an amplified probe beam, a conjugate beam of light is also generated. Δ and δ are the one- and two-photon detuning, respectively.

1.2   Phase-insensitive amplifier

Since the first quantum squeezing generation based on 4WM in sodium vapor was demonstrated about 30 years ago [15], different squeezing mechanisms involving atomic vapor have been proposed and experimentally realized [16–22]. Nowadays, the 4WM-based phase-insensitive amplifier (PIA), constructed using an atomic vapor, has been proven to be an effective and reliable source of two-mode squeezed

states and continuous-variable entanglement[2]. It has become an extremely useful tool in the quantum capabilities toolbox world wide [14, 23–33].

Figure 1.3 contains the sketch and the energy diagram of this 4WM-based PIA scheme where a strong pump beam and a weak probe beam are crossed in an atomic vapor. Two photons are converted from the strong pump beam into "twin" photons emitted into the spatially separated probe and conjugate modes as a result of the momentum conservation (see the energy diagram in Fig. 1.3). The output probe beam is thus amplified and the amplification is independent of the phase of the input probe field. The atomic ground state coherence largely suppresses the excess noise due to the spontaneous emission, which is the limiting factor of many atomic-vapor-based squeezing generation schemes.

This 4WM based PIA scheme has been successfully implemented in a number of applications in atomic-based quantum memories and precision measurements, such as an optically tunable delay for entangled beams of light with Einstein-Podolsky-Rosen (EPR) levels of entanglement [25], the generation of high-purity narrow-band single photons [34] and the realization of an SU(1, 1) quantum interferometer with high phase sensitivity [35–37]. In our lab, we use this 4WM based PIA not only as a source of the two-mode squeezed state but also a gain-assisted anomalous dispersion medium.

---

[2]The two-mode squeezed states and continuous-variable entanglement will be discussed later.

1.3 Phase-sensitive amplifier

Unlike the phase-insensitive amplification, which inevitably adds extra noise to the input signal due to the simultaneous amplification of the input vacuum fluctuations [38] as shown in Fig. 1.3, the possibility for a phase-sensitive noiseless amplification was first demonstrated theoretically by Caves [39]. The idea of this phase-sensitive amplification is sketched in Fig. 1.4(b). Since the first experimental demonstrations of phase-sensitive noiseless amplification of temporal optical signals for continuous-wave [40] and for pulsed optical signals [41] in 1993, optical parametric phase-sensitive amplification has been intensively investigated both theoretically and experimentally. The noiseless amplification feature [38, 39] of the phase-sensitive amplifier (PSA) is extremely attractive for a variety of fields including optical communications [42, 43], quantum information processing [44, 45], and image amplification [46–49].

The single-mode PSA sketch is shown in Fig. 1.4(b). When inputting a signal in the correct quadrature component, the PSA amplifies both the signal and the noise in the quadrature, but deamplifies the noise in the orthogonal quadrature. By amplifying one quadrature and deamplifying the orthogonal quadrature, the PSA preserves the statistical properties of the noise in each quadrature of the input state, but alters the overall statistics. It is possible to amplify a signal encoded in one quadrature component of a nonclassical state of light using an optical PSA, without degrading the quantum features in that quadrature.

To date, most PSAs were implemented based on parametric processes in optical
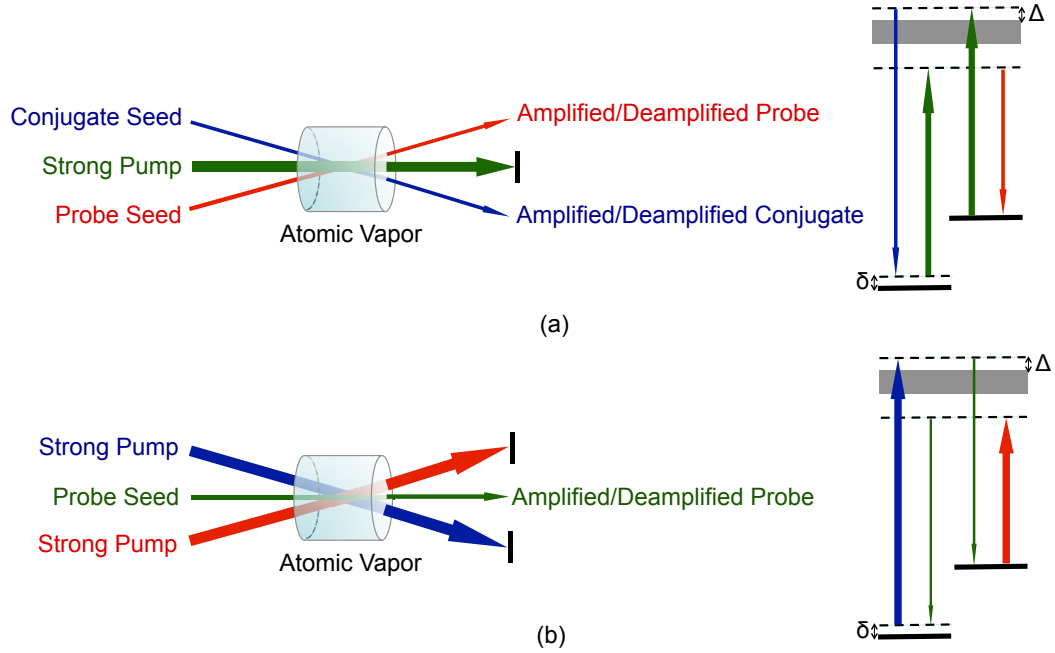
Figure 1.4: Sketches and energy diagrams for the phase-sensitive amplification. (a) Two-mode PSA: both of the two input ports are seeded with beams of light. Due to the 4WM interactions, the output probe and conjugate beams of light are amplified or deamplified depending on the phase of the input beams. (b) Single-mode PSA: the roles of beams played in (a) are swapped so that there is only a single input port for the probe seed. The output of the probe beam is amplified or deamplified depending on the phase of the input beams. Δ and δ are the one- and two-photon detuning, respectively.

fibers [50–56] partially due to their capability of supporting high signal gain if one launches the input fields into highly nonlinear fibers and lets them propagate for a long distance. There are also a few PSAs that were enabled by nonlinear crystals based on type I phase-matching conditions [46–48, 57]. In our lab, phase-sensitive amplification is implemented by 4WM in atomic vapor. Previous work in our group has demonstrated the noiseless amplification of mutliple spatial modes [49] and the generation of single-beam quadrature squeezed states [58] by use of this PSA.

1.4 Fast and slow light

It is well known that the group velocity of a narrow-band optical pulse traveling in a dielectric medium with an index of refraction n can be written as [59]

$$v_g = \frac{c}{n + \omega \frac{\partial n}{\partial \omega}},\qquad(1.4)$$

where c is the speed of light in vacuum. We emphasize the fact that the expression for group velocity of an optical pulse is evaluated at the carrier frequency of the pulse.

Equation 1.4 is very suggestive: the group velocity is given by the speed of light in vacuum divided by a term that includes both the index of refraction and the derivative of the index. Accordingly, the denominator is often referred to as the group index of refraction n_g and can assume values that are larger or smaller than unity, giving rise to "slow" and "fast" light, respectively.

Over the past years, many experiments have demonstrated the ability to manipulate the group velocities of optical pulses propagating through atomic vapors [60–63]. In particular, much work has been done to understand fast-light phenomena associated with anomalous dispersion (i.e., $\partial n/\partial \omega < 0$), which can give rise to group velocities that are greater than the speed of light in vacuum (or even negative) [64]. It is of no surprise that, although an optical pulse may propagate faster than the speed of light in vacuum, the information contained in the pulse will never travel superluminally [65–67]. Although the experiments in [65–67] were

conducted to investigate the propagation of information in fast-light media and the conclusion drawn was the information cannot travel faster than the speed of light in vacuum, they didn't specify what limits the speed of information. A point of view is that it is the quantum noise that limits the information velocity to values less than c [68]. Although noise may have affected the experimental results in [65–67], these experiments were not conducted in a regime where quantum noise necessarily played a crucial role.

To this end, we have studied in the quantum noise regime how the anomalous dispersion associated with phase-insensitive gain affects the propagation of information. We find that the cross-correlation between the two modes of a bipartite entangled state (i.e., the probe mode and conjugate mode in Fig. 1.3) can be advanced by propagating through a PIA acting as a fast-light medium and, the extra noise added by the PIA has been speculated to limit the advance of entanglement, preventing the information from traveling superluminally [29, 68]. In the case of a PSA, however, it is well known that no extra noise will be added for the quadrature with the correct input phase (e.g., at the maximal amplification and the maximal deamplification). It is therefore of natural interest to extend our investigation to explore the advance and delay of information transmitted through a PSA.

1.5   Outline

In this thesis, we utilize a PIA to prepare two-mode quantum correlations in the form of photon-number-difference squeezed optical beams, i.e., twin beams. We

then use one mode of the generated two-mode squeezed state as the input to our PSA. We make use of the PSA as an optical phase-modulation quantifier, a quantum optical pre-amplifier and an "apparent" fast and slow light device in three different experiments. The investigations of optical properties of the PSA in each experiment are the main contents of this thesis. This thesis is structured as follows:

Chapter 2 is devoted to the basic quantum mechanics of the linear optical amplifiers, both PIA and PSA. We deduce gain and noise properties for both PIA and PSA. Introduction of some quantum features, such as two-mode squeezed state, entanglement, quadrature squeezed state, is also given. Finally, phase-space representations of both the phase-insensitive and phase-sensitive amplification are illustrated for a better understanding of the amplifiers' optical properties.

In Chapter 3, we describe the effects of input phase and amplitude modulation on the output of a quantum-noise-limited PSA realized in atomic rubidium vapor. We investigate the dependence of phase modulation (PM) on the alignment of an acousto-optical modulator in an optical beam and demonstrate a novel approach to quantifying PM by using the PSA as a diagnostic tool. We then use this method to measure the alignment-dependent PM of an optical chopper which arises due to diffraction effects as the chopper blade passes through the optical beam.

In Chapter 4, we demonstrate the ability of a PSA to pre-amplify quantum correlations in twin light beams before degradation due to loss and detector inefficiency. We use a PIA realized in atomic rubidium vapor to generate bright beams in a two-mode squeezed state. One of these two modes then passes through a PSA to noiselessly pre-amplify the state before loss is intentionally introduced. We demon-

strate that the two-mode squeezing can largely be preserved under these conditions.

In Chapter 5, we implement a fast-and-slow-light experiment using a PSA as the "dispersive" medium. We first use the mutual information contained in a bipartite entangled state produced by a PIA as the input signal to a PSA. We study the timing of the peak and leading edge of the mutual information as a function of PSA phase. We show that there is no dispersion-like[3] behavior at the two phases where the PSA yields the maximal amplification and maximal deamplification. On the other hand, the peak of mutual information could either be delayed or advanced at any other phase. As opposed to the behavior of the peak, the leading edge of the mutual information is always bounded by the reference case recorded without the presence of the PSA. We then use an amplitude modulated classical beam as the input signal to the PSA. We compare the results from these two different inputs and demonstrate the similarities between them. To explain the physics, we provide a theoretical model with distributed gain on the carrier as well as on both the positive and negative side bands but with distributed loss only on the negative side band, which gives good agreement with the experimental results.

Finally, Chapter 6 provides the summary and outlooks for possible future investigations.

---

[3]In our case, this behavior is described as the frequency-dependent gain or loss as opposed to the frequency-dependent index of refraction in the usual fast-and-slow-light effects.

Chapter 2: Quantum mechanics for linear optical amplifiers

2.1 Introduction

As described by Caves [39], a linear optical amplifier is an optical amplifier whose output signal is linearly related to its input signal. Concerning the gain and noise characteristics, all linear amplifiers can be divided into two categories: phase-insensitive amplifiers (PIA), whose gain and noise are independent of the phase of the input signal, and phase-sensitive amplifiers (PSA), whose gain and noise are phase dependent. As we shall see later, the former amplification process inevitably adds extra noise to the input signal, while with the latter one it is possible to noiselessly amplify[1] an input signal. In this chapter, a simple quantum-mechanical model starting from a generic four-wave mixing (4WM) Hamiltonian in the interaction picture is provided to derive the gain and noise properties of both the PIA and the PSA.

---

[1]In this thesis, noiseless amplification refers to an amplification process where the input signal-to-noise ratio is preserved.

2.2 Four-wave mixing

Let us first consider the 4WM based on a double-Λ configuration depicted in Fig. 2.1.

This 4WM process involves three modes, a, b and c, which are conventionally referred to as the probe, conjugate and pump respectively. It is a cycle that annihilates a pump photon, creates a probe photon, annihilates another pump photon and then creates a conjugate photon; or vise versa, two photons, one from the probe and the other from the conjugate, are converted into the pump mode. This is evident when examining the simplified phenomenological interaction Hamiltonian [69, 70],

$$\hat{H}_I = i\hbar\chi\hat{c}^2\hat{a}^\dagger\hat{b}^\dagger + (-i)\hbar\chi^*\hat{c}^{\dagger 2}\hat{a}\hat{b}, \tag{2.1}$$

where χ is the effective interaction strength that depends on the third-order nonlinear susceptibility $\chi^{(3)}$ and the path length of the interaction L. Most 4WM experiments use very bright pump modes to drive the nonlinear medium, therefore, it is safe to treat the pump mode c as classical. The interaction Hamiltonian in Eq. 2.1 can then be rewritten as:

$$\hat{H}_I = i\hbar\xi e^{i\theta}\hat{a}^\dagger\hat{b}^\dagger + h.c., \tag{2.2}$$

where ξ is the strength of interaction that depends not only on the third-order nonlinear susceptibility and the path length of the interaction but also the intensity
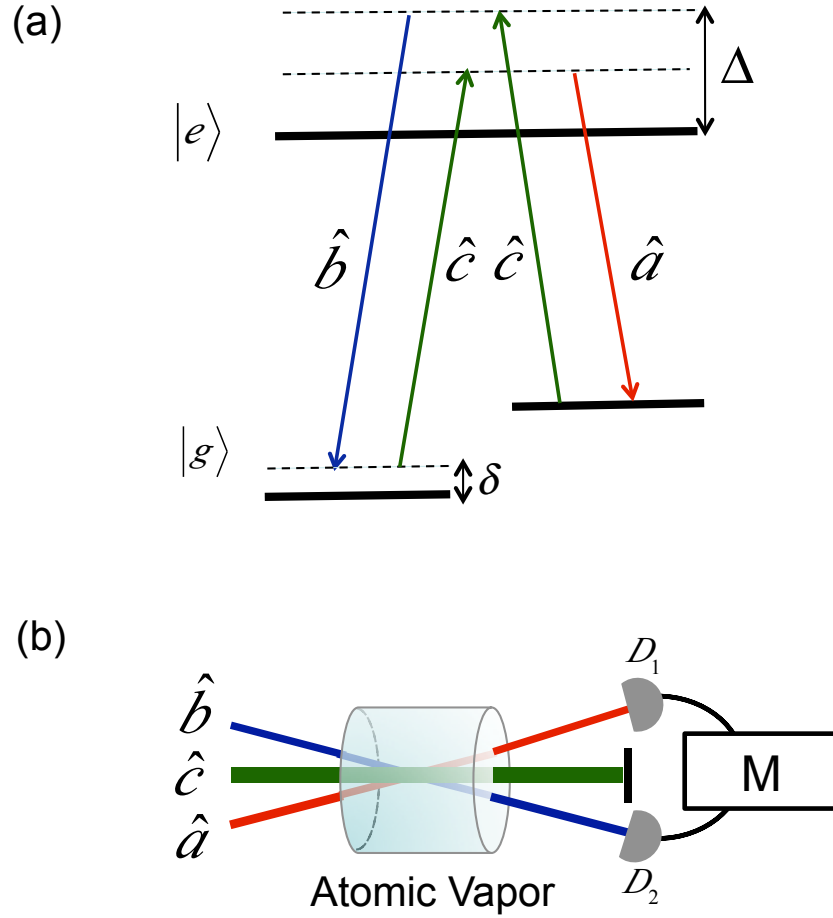
Figure 2.1: (a). 4WM based on a double-Λ configuration. The atomic level scheme is comprised of two ground states and one excited state and three input modes a, b and c. Δ is the one photon detuning. δ is the two-photon detuning. (b). Experimental realization of the 4WM. Three inputs are crossed at the center of the atomic vapor with a small relative angle to fulfill the phase matching condition as depicted in Fig.1.1(b). D_1 and D_2 are two detectors which may be intensity detectors or homodyne detectors. M denotes the processing of the data.

of the pump. Since the third-order nonlinear susceptibility is a function of atomic resonances, ξ thus has dependence on Δ and δ labeled in Fig. 2.1(a) as well. $\theta = 2\phi_c$, where ϕ_c is the phase of the pump field, without loss of generality, it is treated as 0.

From Eq. 2.2 together with the equation of motion for operators in the interaction picture,

$$\frac{d\hat{O}}{dt} = \frac{1}{i\hbar}[\hat{O}, \hat{H}_I], \tag{2.3}$$

where $\hat{O}$ denotes any mode operator in the 4WM process, one is able to obtain the time evolutions for operators $\hat{a}$ and $\hat{b}^\dagger$:

$$\frac{d\hat{a}}{dt} = \xi e^{i\theta}\hat{b}^\dagger,$$
$$\frac{d\hat{b}^\dagger}{dt} = \xi e^{-i\theta}\hat{a}. \tag{2.4}$$

It is trivial to solve this set of differential equations with respect to the input operators $\hat{a}$ and $\hat{b}^\dagger$:

$$\hat{a}(t) = (\cosh\xi t)\hat{a} + (e^{i\theta}\sinh\xi t)\hat{b}^\dagger,$$

$$\hat{b}^\dagger(t) = (\cosh\xi t)\hat{b}^\dagger + (e^{-i\theta}\sinh\xi t)\hat{a}. \tag{2.5}$$

Define $r = \xi T$, where T is the interaction time and it is related to the path length of interaction L by $T = L/v_g$, where v_g is the group velocity. Then the final operators after the 4WM are

$$\hat{a}_f = (\cosh r)\hat{a} + (e^{i\theta}\sinh r)\hat{b}^\dagger,$$

$$\hat{b}_f^\dagger = (\cosh r)\hat{b}^\dagger + (e^{-i\theta}\sinh r)\hat{a}. \tag{2.6}$$

16

Recall that for a generic linear amplifier, the input-output relation can be written as

$$\hat{a}_{out} = \mu \hat{a}_{in} + \nu \hat{b}_{in}^\dagger, \qquad (2.7)$$

where $\hat{a}_{in}$ and $\hat{b}_{in}$ are the annihilation operators of the input modes, and $\hat{a}_{out}$ is the annihilation operator after the amplification process. The complex transfer coefficients μ and ν are related to the gain and other details of the amplification process and must satisfy $|\mu|^2 - |\nu|^2 = 1$ in order to satisfy the commutation relations of the output field. Comparing Eqs. 2.6 with Eq. 2.7, we conclude that the 4WM process is linear amplification.

The experimental realization of the 4WM is sketched in Fig.2.1(b), where three inputs are crossed in an atomic vapor with a relatively small angle in order to fulfill the phase matching condition as depicted in Fig.1.1(b). When the probe port a is seeded with a coherent field and the conjugate port b is seeded with vacuum, the 4WM process acts as a PIA [14, 23]. When the probe and conjugate ports are seeded with coherent fields simultaneously, the amplifier turns into a PSA. In the following sections we will use Eqs. 2.6 to derive the gain and noise characteristics for both the PIA and the PSA.

2.3   Phase-insensitive amplifier

2.3.1   Two-mode intensity difference squeezing

We now can model a PIA as a linear amplifier described by Eqs. 2.6 with a coherent state input $|\alpha\rangle$, $\alpha = |\alpha|e^{i\phi_i}$, where ϕ_i is the input phase, seeding mode a, and mode b is only fed by vacuum fluctuations. In this case the input state can be viewed as $|\alpha, 0\rangle$. It is then straightforward to calculate the mean output photon number $\langle \hat{n}_a \rangle \equiv \langle \hat{a}_f^\dagger \hat{a}_f \rangle$ and the photon-number variance $\Delta \hat{n}_a^2 \equiv \langle \hat{n}_a^2 \rangle - \langle \hat{n}_a \rangle^2 \equiv \langle \hat{a}_f^\dagger \hat{a}_f \hat{a}_f^\dagger \hat{a}_f \rangle - \langle \hat{a}_f^\dagger \hat{a}_f \rangle^2$ with this input state $|\alpha, 0\rangle$:

$$\langle \hat{n}_a \rangle = |\alpha|^2 \cosh^2 r + \sinh^2 r, \tag{2.8}$$

$$\Delta \hat{n}_a^2 = \frac{1}{2}[-1 + (1 + 2|\alpha|^2)\cosh 2r]\cosh^2 r. \tag{2.9}$$

If we define $G_{\mathrm{PIA}} = \cosh^2 r$ and assume an input coherent state that is sufficiently bright, e.g., $|\alpha|^2 \gg 1$, Eqs. 2.8 and 2.9 could be simplified to

$$\langle \hat{n}_a \rangle = |\alpha|^2 \cosh^2 r = G_{\mathrm{PIA}} \langle \hat{n}_{in} \rangle, \tag{2.10}$$

$$\Delta \hat{n}_a^2 = |\alpha|^2 \cosh^2 r \cosh 2r = G_{\mathrm{PIA}}(2G_{\mathrm{PIA}} - 1)\Delta \hat{n}_{in}^2, \tag{2.11}$$

since for a coherent state input seeding mode a, $\Delta \hat{n}_{in}^2 \equiv \langle \hat{n}_{in} \rangle = |\alpha|^2$. It is clear that

there is no input phase ϕ_i dependence either in the gain or in the noise expression.

In the same manner, one is able to calculate the mean output photon number $\langle \hat{n}_b \rangle \equiv \langle \hat{b}_f^\dagger \hat{b}_f \rangle$ and the photon-number variance $\Delta \hat{n}_b^2 \equiv \langle \hat{n}_b^2 \rangle - \langle \hat{n}_b \rangle^2 \equiv \langle \hat{b}_f^\dagger \hat{b}_f \hat{b}_f^\dagger \hat{b}_f \rangle - \langle \hat{b}_f^\dagger \hat{b}_f \rangle^2$ with the input state $|\alpha, 0\rangle$ for the b mode:

$$\langle \hat{n}_b \rangle = |\alpha|^2 \sinh^2 r + \sinh^2 r, \tag{2.12}$$

$$\Delta \hat{n}_b^2 = \frac{1}{2}[1 + (1 + 2|\alpha|^2) \cosh 2r] \sinh^2 r. \tag{2.13}$$

With the assumption of $|\alpha|^2 \gg 1$, they are further simplified to

$$\langle \hat{n}_b \rangle = |\alpha|^2 \sinh^2 r = (G_{\mathrm{PIA}} - 1)|\alpha|^2, \tag{2.14}$$

$$\Delta \hat{n}_b^2 = |\alpha|^2 \sinh^2 r \cosh 2r = (G_{\mathrm{PIA}} - 1)(2G_{\mathrm{PIA}} - 1)|\alpha|^2. \tag{2.15}$$

In the quantum optics community, people refer to the output probe and conjugate modes n_a and n_b as "twin beams"[2].

The noise of the intensity difference $\hat{n}_{\mathrm{diff}} = \hat{n}_a - \hat{n}_b = \hat{a}_f^\dagger \hat{a}_f - \hat{b}_f^\dagger \hat{b}_f$ of the twin beams is

$$\Delta \hat{n}_{\mathrm{diff}}^2 = \frac{1}{4}[(-1 + 3|\alpha|^2) + (1 + |\alpha|^2) \cosh 4r] - \frac{1}{2}(1 + |\alpha|^2) \sinh^2 2r \cos 4\phi_c. \tag{2.16}$$

---

[2]In addition to the correlated intensity fluctuations, "twin beams" also implies their phase fluctuations are anti-correlated.

For simplicity and without the loss of generality, we set the pump phase $\phi_c = 0$, then the above expression is reduced to

$$\Delta \hat{n}_{\text{diff}}^2 = |\alpha|^2. \tag{2.17}$$

The shot noise level of the twin beams is just the sum of Eq. 2.10 and Eq. 2.14:

$$\Delta \hat{n}_{\text{snl}}^2 = (\cosh^2 r + \sinh^2 r)|\alpha|^2 = (2G_{\text{PIA}} - 1)|\alpha|^2. \tag{2.18}$$

We define the two-mode intensity-difference squeezing in dB to be

$$\text{SQZ}_{\text{diff}} = 10 \log_{10}\left(\frac{\Delta \hat{n}_{\text{diff}}^2}{\Delta \hat{n}_{\text{snl}}^2}\right) = 10 \log_{10}\left(\frac{1}{2G_{\text{PIA}} - 1}\right). \tag{2.19}$$

In Fig. 2.2 we plot the two-mode intensity difference squeezing as a function of G_{PIA}. More squeezing can be achieved with greater PIA gain.

Achievements of good two-mode intensity difference squeezing have been reported in [14, 23].

2.3.2 Continuous-variable quantum entanglement

Since this 4WM scheme has manifested itself as a reliable source of not only two-mode squeezed states and but also continuous-variable quantum entanglement [25, 26], its joint quadrature noise properties are therefore worthy of being derived as well.

Let us now consider the noise properties of the output mode quadratures.
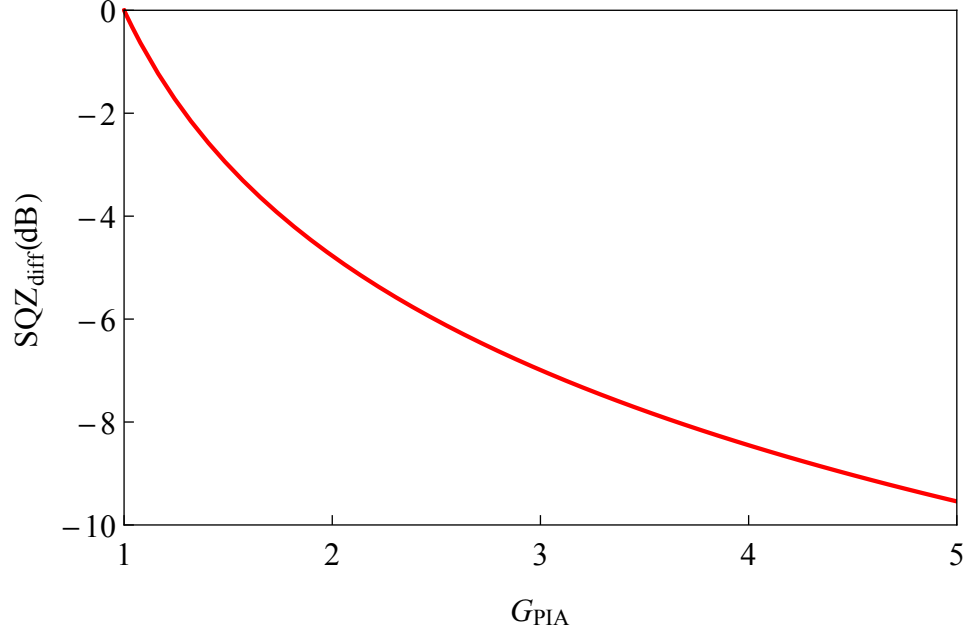
Figure 2.2: Two-mode intensity difference squeezing as a function of G_{PIA}.

Define the amplitude quadrature of the output probe mode as $\hat{X}_a = (\hat{a}_f + \hat{a}_f^\dagger)/2$, then the mean and variance of the quadrature $\langle \hat{X}_a \rangle$ with the input state $|\alpha, 0\rangle$ is

$$\langle \hat{X}_a \rangle = |\alpha| \cos \phi_i \cosh r = \sqrt{G_{\text{PIA}}} \langle \hat{X}_i \rangle, \tag{2.20}$$

$$\Delta \hat{X}_a^2 = \frac{1}{4} \cosh 2r = (2G_{\text{PIA}} - 1)\Delta \hat{X}_i^2, \tag{2.21}$$

since for a coherent state input seeding mode a, $\langle \hat{X}_i \rangle = |\alpha| \cos \phi_i$ and $\Delta \hat{X}_i^2 = 1/4$. Calculations of the phase quadrature $\hat{Y}_a = (\hat{a}_f - \hat{a}_f^\dagger)/2i$ render similar results to Eqs. 2.20 and 2.21:

$$\langle \hat{Y}_a \rangle = |\alpha| \sin \phi_i \cosh r = \sqrt{G_{\text{PIA}}} \langle \hat{Y}_i \rangle, \tag{2.22}$$

$$\Delta \hat{Y}_a^2 = \frac{1}{4} \cosh 2r = (2G_{\text{PIA}} - 1)\Delta \hat{Y}_i^2, \tag{2.23}$$

since $\langle \hat{Y}_i \rangle = |\alpha| \sin \phi_i$ and $\Delta \hat{Y}_i^2 = 1/4$ for an input coherent state. Notice that, neither the quadrature amplitudes $\langle \hat{X}_a \rangle$ and $\langle \hat{Y}_a \rangle$ nor the noise $\Delta \hat{X}_a^2$ and $\Delta \hat{Y}_a^2$ have a dependence on the input phase ϕ_i, as we expected for a PIA.

For the sake of completeness, we calculate the mean and noise of the output conjugate quadratures $\hat{X}_b = (\hat{b}_f + \hat{b}_f^\dagger)/2$ and $\hat{Y}_b = (\hat{b}_f - \hat{b}_f^\dagger)/2i$ with the same treatment:

$$\langle \hat{X}_b \rangle = |\alpha| \cos(\phi_i + 2\phi_c) \sinh r = \sqrt{G_{\text{PIA}} - 1}[|\alpha| \cos(\phi_i + 2\phi_c)], \tag{2.24}$$

$$\Delta \hat{X}_b^2 = \frac{1}{4} \cosh 2r = (2G_{\text{PIA}} - 1)\Delta \hat{X}_i^2, \tag{2.25}$$

$$\langle \hat{Y}_b \rangle = -|\alpha| \sin(\phi_i + 2\phi_c) \sinh r = \sqrt{G_{\text{PIA}} - 1}[-|\alpha| \sin(\phi_i + 2\phi_c)], \tag{2.26}$$

$$\Delta \hat{Y}_b^2 = \frac{1}{4} \cosh 2r = (2G_{\text{PIA}} - 1)\Delta \hat{Y}_i^2. \tag{2.27}$$

Notice that, because the noise of the input coherent state is independent of $|\alpha|$, the output quadrature noise is also independent of $|\alpha|$, and $\Delta \hat{X}_a^2 = \Delta \hat{Y}_a^2 = \Delta \hat{X}_b^2 = \Delta \hat{Y}_b^2$, the noise on both quadratures of the output probe and conjugate modes are the same.

In order to characterize the entanglement between the output probe and conjugate modes, we need to analyze joint variables. For the case of the electromagnetic field, these variables correspond to the joint quadrature operators $\hat{X}_- = \hat{X}_a - \hat{X}_b$ and $\hat{Y}_+ = \hat{Y}_a + \hat{Y}_b$, which are the joint quadratures of the amplitude difference, $\hat{X}_-$, and phase sum, $\hat{Y}_+$, between the fields. Based on the noise properties of these quadratures, different degrees of continuous-variable entanglement exist. The variance, or noise, of these operators for coherent states sets the standard quantum limit (SQL) of the quadrature fluctuations. The requirement for entanglement is that the states of the two modes cannot be described independently, a property known as inseparability. This property can be quantified with the inseparability parameter $I = (\Delta\hat{X}_-^2)_N + (\Delta\hat{Y}_+^2)_N$, where the N subscript indicates that the variances have been normalized to the corresponding SQL. The state of the two modes is inseparable when $I < 2$ [71], such that having both $\Delta\hat{X}_-^2$ and $\Delta\hat{Y}_+^2$ below the SQL, or squeezed, is a sufficient condition for entanglement.

The joint quadrature variance can be measured using two balanced homodyne detectors (HD). Figure 2.3 is the sketch of the balanced homodyne detector measuring a generalized target state $\hat{t}$.

Each output mode, a_f and b_f, is separately combined with its own local oscillator (LO) field at a 50/50 beam splitter so that one can determine the generalized quadrature for each mode. Then the subtraction or addition is taken to render the measurement of the joint quadrature variance. This is equivalent to a single HD measurement where the joint output mode $\hat{J}_\mp = \hat{a}_f \mp \hat{b}_f$ is combined with a strong

LO field[3] at a 50/50 beam splitter. Specifically, combining $\hat{J}_-$ with a LO field gives the measurement of $\Delta \hat{X}_-^2$. Similarly, combining $\hat{J}_+$ with a LO field gives the measurement of $\Delta \hat{Y}_+^2$. Assume the LO is a coherent state with a coherent amplitude $\beta = |\beta|e^{\varphi_{\text{lo}}}$, then the measured variance of the intensity difference between the two outputs of the beam splitter for the joint output modes $\hat{J}_-$ and $\hat{J}_+$ are

$$\Delta \hat{X}_{J_-}^2 = \frac{1}{2}|\beta|^2(\cosh 2r + \cos 2\varphi_{\text{lo}} \cos 2\phi_c \sinh 2r), \tag{2.28}$$

$$\Delta \hat{X}_{J_+}^2 = \frac{1}{2}|\beta|^2(\cosh 2r - \cos 2\varphi_{\text{lo}} \cos 2\phi_c \sinh 2r), \tag{2.29}$$

where $\Delta \hat{X}_{J_\mp}^2$ denotes the variance of the generalized joint quadrature $\hat{X}_{J_\mp}$. We again are permitted to set the pump phase $\phi_c = 0$ for simplification. Since the SQL of the HD measurement is $|\beta|^2/4 + |\beta|^2/4 = |\beta|^2/2$, the squeezing of the generalized joint quadrature would be

$$\text{SQZ}_{J_-} = 10\log_{10}(\cosh 2r + \cos 2\varphi_{\text{lo}} \sinh 2r), \tag{2.30}$$

$$\text{SQZ}_{J_+} = 10\log_{10}(\cosh 2r - \cos 2\varphi_{\text{lo}} \sinh 2r). \tag{2.31}$$

In Fig. 2.4, we plot SQZ_{J_-} and SQZ_{J_+} as a function of the LO phase φ_{lo} when the PIA gain $G_{\text{PIA}} = \cosh^2 r = 3$. We find that, when $\varphi_{\text{lo}} = \pi/2$, we are measuring

---

[3]Assuming the LO field here is bi-chromatic to work on the joint output modes $\hat{J}_\mp$, since modes $\hat{a}_f$ and $\hat{b}_f$ have different frequencies.
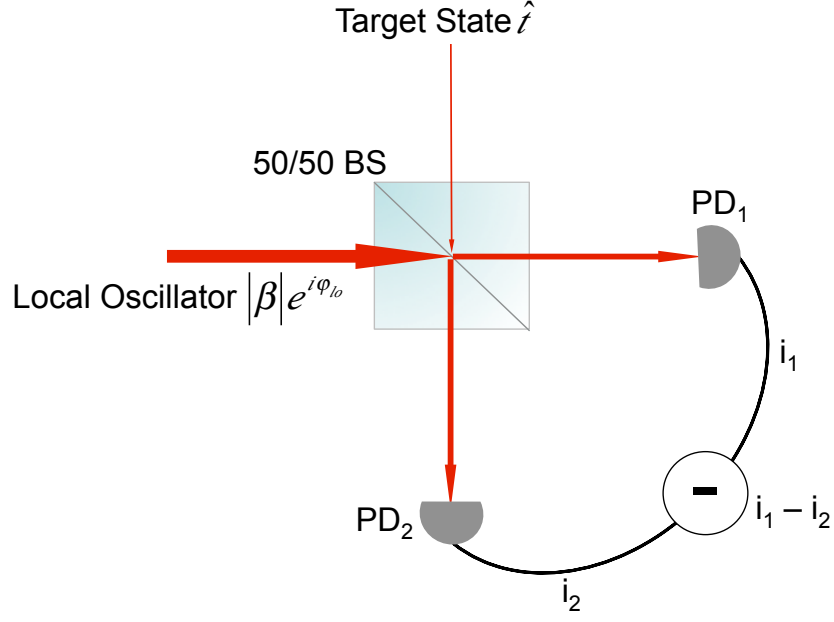
Figure 2.3: Sketch of the balanced homodyne detector measuring a generalized target state $\hat{t}$. The mean and variance of the output photocurrent difference are $i_1 - i_2 = 2|\beta|\langle\hat{X}^\theta\rangle$ and $\Delta(i_1 - i_2)^2 = 4|\beta|^2\Delta(\hat{X}^\theta)^2$, where $\hat{X}^\theta = \hat{t}e^{i\theta} + \hat{t}^\dagger e^{-i\theta}$ and $\theta = \varphi_{\text{lo}} - \pi/2$.

the variance $\Delta\hat{X}_-^2$ of the joint quadrature $\hat{X}_-$ and, when $\varphi_{\text{lo}} = \pi$ we are measuring

the variance $\Delta\hat{Y}_+^2$ of the joint quadrature $\hat{Y}_+$, and they are both squeezed by the

same amount $10\log_{10}(\cosh 2r - \sinh 2r)$. It clearly indicates the existence of the

quantum entanglement between the output probe and conjugate modes.
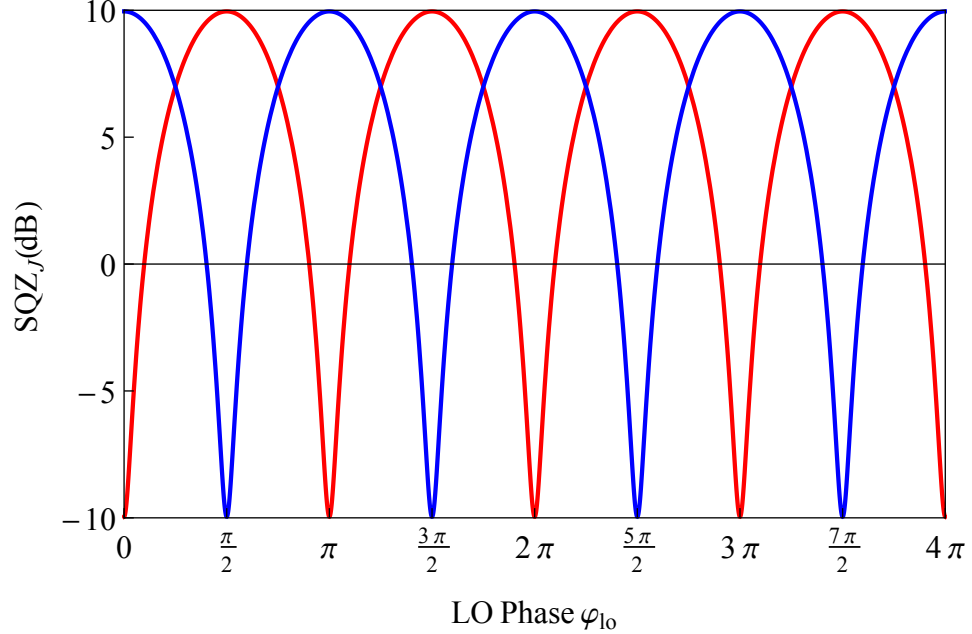
Figure 2.4: Squeezing of the generalized joint quadrature SQZ_{J_-} (blue) and SQZ_{J_+} (red) as a function of LO phase φ_{lo} when $G_{\text{PIA}} = \cosh^2 r = 3$. The minima of the blue curve correspond to the squeezing value of $\Delta\hat{X}_-^2$, while the minima of the red curve correspond to the squeezing value of $\Delta\hat{Y}_+^2$.

2.3.3 Noise figure of the phase-insensitive amplifier

In the noise theory of a classical amplifier, the deterioration of the signal to noise ratio (SNR) as the signal passes through the amplifier is used as a measure of the amplifier noise performance. Following this idea, we define the noise figure (NF) of the optical amplifier as the ratio between the SNR of the input signal (SNR_{in}) and the output (SNR_{out}):

$$NF = \frac{SNR_{\text{in}}}{SNR_{\text{out}}}. \tag{2.32}$$

In general, the amplification process of an input signal does not improve the SNR. This is because the amplifier can not preferentially amplify the signal over the

26

noise. With an amplifier adding no excess noise, we obtain, at best,

$$\text{NF} = 1. \tag{2.33}$$

For a coherent input state with coherent amplitude α and with unity noise size, the $\text{SNR}_{\text{in}} \equiv |\alpha|^2$. By insertion of Eqs. 2.10 and 2.11 into

$$\text{SNR}_{\text{out}} \equiv \frac{\langle \hat{n}_a \rangle^2}{\Delta \hat{n}_a^2}, \tag{2.34}$$

it is then trivial for one to get the NF for the PIA:

$$\text{NF}_{\text{PIA}} = \frac{\text{SNR}_{\text{in}}}{\text{SNR}_{\text{out}}} = \frac{2\text{G}_{\text{PIA}} - 1}{\text{G}_{\text{PIA}}} = 2 - \frac{1}{\text{G}_{\text{PIA}}}. \tag{2.35}$$

In Fig. 2.5, we plot the NF_{PIA} versus G_{PIA}. We observe that the NF_{PIA} is always larger than one when $\text{G}_{\text{PIA}} > 1$. Thus, the PIA always reduces the SNR of an input signal after amplification. Therefore, quantum mechanics imposes a fundamental limit on the performance of a PIA, resulting in the degradation of the SNR, which reaches a factor of 2 (3 dB) at high gains ($\text{G}_{\text{PIA}} \to \infty$). People often refer to this noise property of the PIA as the "3 dB noise penalty".

2.4   Phase-sensitive amplifier

In analogy to PIAs, a generalized PSA can also be modeled as a linear amplifier described by Eqs. 2.6 but with coherent fields seeding both the input modes a and
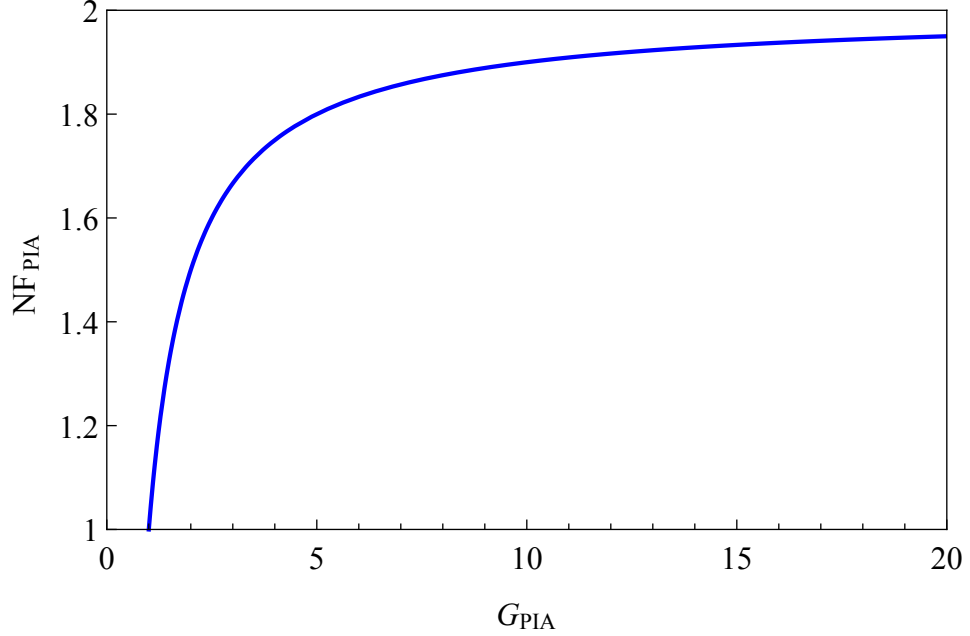
Figure 2.5: Theoretical noise figure of the PIA (NF_{PIA}) as function of the gain (G_{PIA}) (e.g, Eq. 2.35). The relation $NF_{PIA} > 1$ is always true when $G_{PIA} > 1$, which implies the PIA always degrades the input SNR. When $G_{PIA} \to \infty$, $NF_{PIA} \to 2$.

b. In this section we will investigate the gain and noise properties of the PSA under two different conditions: 1. The input modes a and b are fed with two different coherent fields (both of the amplitude and phase are different but with the same frequency); 2. Both a and b are fed with the same coherent field.

2.4.1 Two-mode phase-sensitive amplifier

Let us first assume the input modes a and b are fed with two different coherent fields (but with the same frequency) $|\alpha\rangle$ ($\alpha = |\alpha|e^{i\phi_\alpha}$) and $|\beta\rangle$ ($\beta = |\beta|e^{i\phi_\beta}$) respectively. Then it is easy for one to obtain photon number mean and variances of the

output modes a_f and b_f:

$$\langle \hat{n}_a \rangle = |\alpha|^2 \cosh^2 r + (1 + |\beta|^2) \sinh^2 r + |\alpha||\beta| \sinh 2r \cos(\phi_\alpha + \phi_\beta - 2\phi_c), \quad (2.36)$$

$$\Delta \hat{n}_a^2 = \frac{1}{8}[-1 + 2|\alpha|^2 + 2|\beta|^2 + 4(|\alpha|^2 - |\beta|^2) \cosh 2r + (1 + 2|\alpha|^2 + 2|\beta|^2) \cosh 4r$$

$$+ 4|\alpha||\beta| \sinh 4r \cos(\phi_\alpha + \phi_\beta - 2\phi_c)], \quad (2.37)$$

$$\langle \hat{n}_b \rangle = |\beta|^2 \cosh^2 r + (1 + |\alpha|^2) \sinh^2 r + |\alpha||\beta| \sinh 2r \cos(\phi_\alpha + \phi_\beta + 2\phi_c), \quad (2.38)$$

$$\Delta \hat{n}_b^2 = \frac{1}{8}[-1 + 2|\alpha|^2 + 2|\beta|^2 + 4(|\beta|^2 - |\alpha|^2) \cosh 2r + (1 + 2|\alpha|^2 + 2|\beta|^2) \cosh 4r$$

$$+ 4|\alpha||\beta| \sinh 4r \cos(\phi_\alpha + \phi_\beta + 2\phi_c)]. \quad (2.39)$$

Consider a simpler case where the input coherent states have the same mean number of photons and are sufficiently bright, i.e., $|\alpha|^2 = |\beta|^2 \gg 1$, the above equations can be reduced to

$$\langle \hat{n}_a \rangle = [\cosh^2 r + \sinh^2 r + \sinh 2r \cos(\phi_\alpha + \phi_\beta - 2\phi_c)]\langle \hat{n}_i \rangle, \quad (2.40)$$

$$\Delta\hat{n}_a^2 = \frac{1}{2}[1 + \cosh 4r + \sinh 4r \cos(\phi_\alpha + \phi_\beta - 2\phi_c)]\Delta\hat{n}_i^2, \qquad (2.41)$$

$$\langle\hat{n}_b\rangle = [\cosh^2 r + \sinh^2 r + \sinh 2r \cos(\phi_\alpha + \phi_\beta + 2\phi_c)]\langle\hat{n}_i\rangle, \qquad (2.42)$$

$$\Delta\hat{n}_b^2 = \frac{1}{2}[1 + \cosh 4r + \sinh 4r \cos(\phi_\alpha + \phi_\beta + 2\phi_c)]\Delta\hat{n}_i^2, \qquad (2.43)$$

where $\langle\hat{n}_i\rangle$ and $\Delta\hat{n}_i^2$ are the mean and variance of the input states, and for coherent states with mean number of photons $|\alpha|^2$, $\langle\hat{n}_i\rangle \equiv \Delta\hat{n}_i^2 = |\alpha|^2$.

We now define the gain of the PSA process as

$$G_{\mathrm{PSA}}(\psi) = \cosh^2 r + \sinh^2 r + \sinh 2r \cos\psi, \qquad (2.44)$$

where $\psi = \phi_\alpha + \phi_\beta \mp 2\phi_c$ is the relative input phase[4], $-$ and $+$ are for the modes a and b, respectively. Unlike the PIA, Eq. 2.40 to Eq. 2.43 tell us that the gain and noise of the PSA have a clear dependence on the relative input phase ψ. The maximal value of the PSA gain $G_{\mathrm{PSA}}^{\max} = (\cosh r + \sinh r)^2 = e^{2r}$ occurs at $\psi = 0$, while the minimum value of the PSA gain $G_{\mathrm{PSA}}^{\min} = (\cosh r - \sinh r)^2 = e^{-2r} = 1/G_{\mathrm{PSA}}^{\max}$ occurs when $\psi = \pi$. We plot the behavior of G_{PSA} as function of ψ in Fig. 2.6 when $G_{\mathrm{PSA}}^{\max} = e^{2r} = 5$.

---

[4]Relative to twice the pump phase ϕ_c.
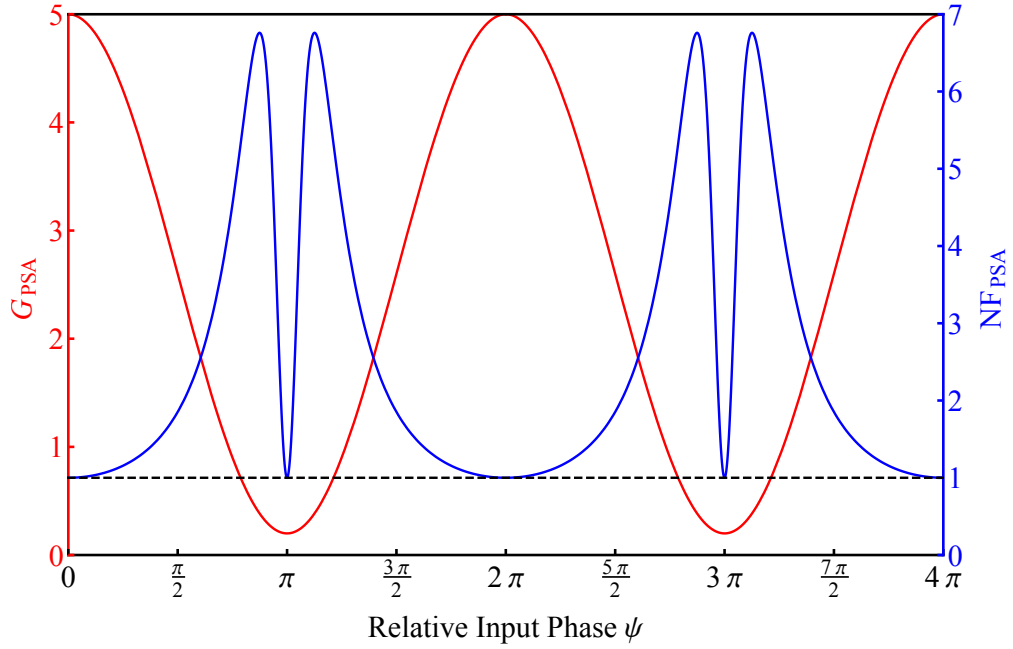
Figure 2.6: Red line: Theoretical gain of the PSA, G_{PSA}, as function of the relative input phase, ψ, (e.g, Eq. 2.44) plotted on the left axis. Blue line: Theoretical noise figure of the PSA, NF_{PSA} as function of the relative input phase, ψ, (e.g, Eq. 2.49) plotted on the right axis. When $\psi = n\pi$, $(n = 0, 1, 2, ...)$, $NF_{PSA} = 1$, which implies the input SNR is preserved after the amplification process.

2.4.2 Noise figure of the two-mode phase-sensitive amplifier

In order to properly characterize the NF of the two-mode PSA, we need to first identify its input and output signals. Notice that, since the PSA has both its input modes a and b seeded with coherent states, we thus should treat modes a and b together as the input signal to the amplifier. To this end, the output signal and noise are

$$\langle \hat{n}_a + \hat{n}_b \rangle = -1 + (1 + |\alpha|^2 + |\beta|^2) \cosh 2r + 2|\alpha||\beta| \cos(\phi_\alpha + \phi_\beta) \cos(2\phi_c) \sinh 2r,$$

$$(2.45)$$

$$\Delta(\hat{n}_a + \hat{n}_b)^2 = \frac{1}{4}[-1 + |\alpha|^2 + |\beta|^2 + (1 + 3|\alpha|^2 + 3|\beta|^2) \cosh 4r + 2(1 + |\alpha|^2 + |\beta|^2) \times$$

$$\cos(4\phi_c) \sinh^2 2r + 8|\alpha||\beta| \cos(\phi_\alpha + \phi_\beta) \cos(2\phi_c) \sinh 4r].$$

$$(2.46)$$

We again take advantage of the assumption of symmetric and bright inputs $|\alpha|^2 = |\beta|^2 \gg 1$ and set pump phase $\phi_c = 0$ to reduce the above equations to

$$\langle \hat{n}_a + \hat{n}_b \rangle = 2[\cosh 2r + \sinh 2r \cos(\phi_\alpha + \phi_\beta)]|\alpha|^2, \qquad (2.47)$$

$$\Delta(\hat{n}_a + \hat{n}_b)^2 = 2[\cosh 4r + \sinh 4r \cos(\phi_\alpha + \phi_\beta)]|\alpha|^2. \qquad (2.48)$$

The NF of the two-mode PSA is readily obtained as

$$\text{NF}_{\text{PSA}} = \frac{\text{SNR}_{\text{in}}}{\text{SNR}_{\text{out}}} = \frac{\cosh 4r + \sinh 4r \cos \psi}{(\cosh 2r + \sinh 2r \cos \psi)^2}, \tag{2.49}$$

where we have used the fact that $\text{SNR}_{\text{in}} = 2|\alpha|^2$. The relative input phase $\psi = \phi_\alpha + \phi_\beta$ since pump phase ϕ_c has been set to 0.

We plot the NF_{PSA} versus the relative input phase ψ in Fig. 2.6 along with the plot of G_{PSA} as function of ψ. We observe that the $\text{NF}_{\text{PSA}}(\psi)$ is minimized and in fact can achieve the limit of $\text{NF}_{\text{PSA}} = 1$ for a value of $\psi = n\pi$, where n is an integer. These values of ψ coincide with both the maximal and minimal values of the PSA gain

$$\text{NF}_{\text{PSA}}(n\pi) = 1, \qquad n = 0, 1, 2, ... \tag{2.50}$$

An interesting result is that this limit ($\text{NF}_{\text{PSA}} = 1$) is independent of G_{PSA}. No matter how large the gain of the amplification process is, one will always have $\text{SNR}_{\text{in}} = \text{SNR}_{\text{out}}$.

This noise characteristic for a PSA, $\text{NF}_{\text{PSA}} = 1$, means that one can amplify an optical signal in the quadrature with the correct input phase without deteriorating its input SNR. This is why this type of linear amplifier is called "noiseless". Nowadays, this unique noise property of the PSA is of great interest to several research fields including optical communications [42, 43], quantum information processing [44, 45], and image amplification [46–49].
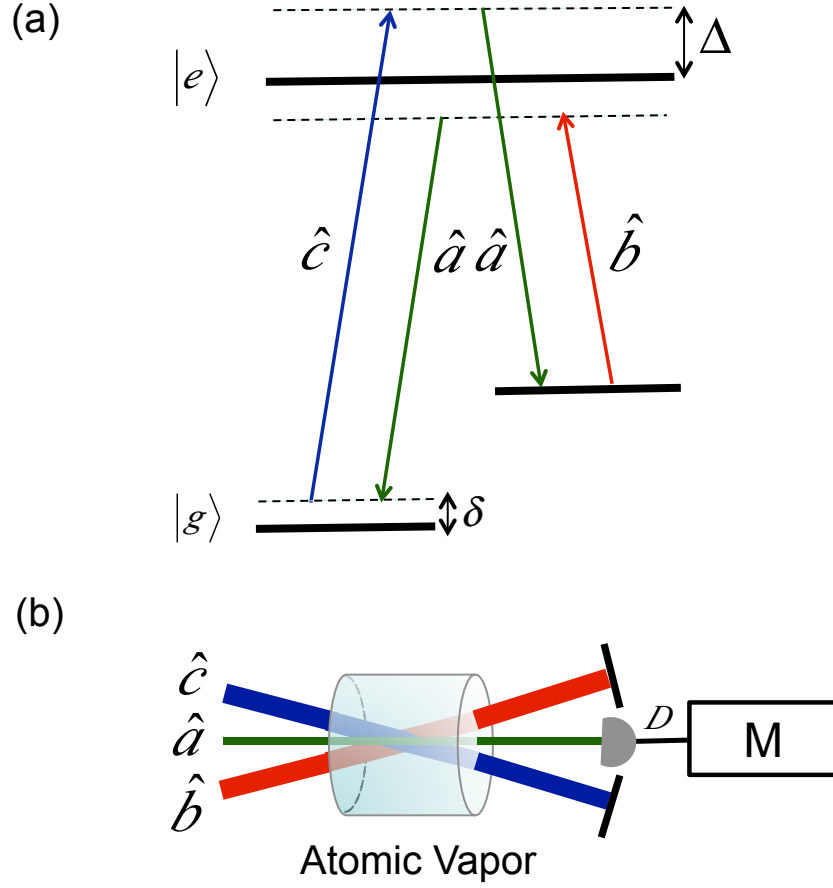
Figure 2.7: Double-Λ configuration (a), and experimental realization (b), of the single-mode PSA. Modes b and c are the pump modes, mode a is the probe mode. Δ is the one photon detuning. δ is the two-photon detuning. D is a detector for the output probe mode which may be intensity detector or homodyne detector. M denotes the processing of the data.

2.4.3 Single-mode phase-sensitive amplifier

Let us now consider reversing the geometric configuration shown in Fig. 2.1: we now pump with two relatively strong modes b and c along the directions of, the probe and conjugate modes in Fig. 2.1 and probe with a weak mode a having the direction of the previous pump. Figure 2.7 is the double-Λ configuration and experimental realization of the single-mode PSA. Notice that, in Fig. 2.7, the fields'

detunings are different than those in Fig. 2.1. As a matter of fact, simply exchanging the roles of the pump and the probe and conjugate beams in Fig. 2.7 does not lead to a properly functioning single-mode PSA. We have found excess noise when the roles of the beams are simply reversed in this manner. This noise is due, at least in part, to extraneous 4WM processes. We have, however, been able to make a properly functioning single-mode PSA by adjusting the operating parameters. In particular, we found it necessary to tune the two pumps, b and c, so that one is above, and the other below, the corresponding atomic resonance as shown in the energy level diagram in Fig. 2.7(a). In this case, the probe mode a is blue of one resonance and red of the other, whereas in Fig. 2.1 it was blue of both resonances.

By treating the strong pump modes b and c as classical and employing the same derivations leading to Eq. 2.6, the input-output relation corresponds to this single-mode PSA can be obtained:

$$\hat{a}_f = (\cosh r)\hat{a} + (e^{i\theta}\sinh r)\hat{a}^\dagger, \tag{2.51}$$

where $\theta = \phi_b + \phi_c$ is the sum of the pump phases.

This type of single-mode PSA is experimentally investigated in this thesis and has been demonstrated as capable of generating multi-spatial-mode single-beam quadrature squeezed states of light [58] as well as noiselessly amplifying images [49].

Using Eq. 2.51 and assuming a coherent state $|\alpha\rangle$, $\alpha = |\alpha|e^{i\phi_i}$, where ϕ_i is the input phase, seeding the input mode a, it is then straightforward for us to get the mean output number of photons $\langle\hat{n}\rangle \equiv \langle\hat{a}_f^\dagger\hat{a}_f\rangle$ and its variance $\Delta\hat{n}^2 \equiv \langle\hat{n}^2\rangle - \langle\hat{n}\rangle^2 \equiv$

$\langle \hat{a}_f^\dagger \hat{a}_f \hat{a}_f^\dagger \hat{a}_f \rangle - \langle \hat{a}_f^\dagger \hat{a}_f \rangle^2$ as

$$\langle \hat{n} \rangle = |\alpha|^2 \cosh^2 r + (1 + |\alpha|^2) \sinh^2 r + |\alpha|^2 \cos(2\phi_i - \theta) \sinh 2r, \qquad (2.52)$$

$$\Delta \hat{n}^2 = \frac{1}{4}[-1 + (1 + 4|\alpha|^2) \cosh 4r + 4|\alpha|^2 \cos(2\phi_i - \theta) \sinh 4r]. \qquad (2.53)$$

With the same treatment of assuming a bright coherent input, i.e., $|\alpha|^2 \gg 1$, we reduce the above equations to

$$\langle \hat{n} \rangle = [\cosh^2 r + \sinh^2 r + \sinh 2r \cos(2\phi_i - \theta)]\langle \hat{n}_i \rangle \qquad (2.54)$$

$$\Delta \hat{n}^2 = [\cosh 4r + \sinh 4r \cos(2\phi_i - \theta)]\Delta \hat{n}_i^2. \qquad (2.55)$$

We now define the gain of the single-mode PSA process as

$$G_{\text{PSA}}(\psi) = \cosh^2 r + \sinh^2 r + \sinh 2r \cos \psi, \qquad (2.56)$$

where $\psi = 2\phi_i - \theta = 2\phi_i - (\phi_b + \phi_c)$ is the relative input phase[5]. Notice that, Eq. 2.56 is identical to the expression, Eq. 2.44, for the gain of the two-mode PSA.

We now study the noise properties of the output mode quadratures. Define the generalized quadrature of the output mode as $\hat{X}_{(\varphi)} = (\hat{a}_f e^{i\varphi} + \hat{a}_f^\dagger e^{-i\varphi})/2$, then the mean and variance of the generalized quadrature $\hat{X}_{(\varphi)}$ with the input coherent

[5]Relative to pump phases sum $\phi_b + \phi_c$.

state $|\alpha\rangle$ is

$$\langle \hat{X}_{(\varphi)}\rangle = [\cos(\phi_i + \varphi)\cosh r + \cos(\phi_i - \varphi)\sinh r]|\alpha|, \qquad (2.57)$$

$$\Delta \hat{X}_{(\varphi)}^2 = \frac{1}{4}(\cosh 2r + \cos 2\varphi \sinh 2r), \qquad (2.58)$$

where we have set the sum of pump phases $\theta = \phi_b + \phi_c = 0$ without loss of generality.

Therefore, one is able to obtain the mean and variances of the amplitude quadrature, $\hat{X} = (\hat{a}_f + \hat{a}_f^\dagger)/2$, and phase quadrature, $\hat{Y} = (\hat{a}_f - \hat{a}_f^\dagger)/2i$, just by assigning $\varphi = 0$ and $-\pi/2$ respectively:

$$\langle \hat{X}\rangle = (\cosh r + \sinh r)|\alpha|\cos\phi_i, \qquad (2.59)$$

$$\Delta \hat{X}^2 = \frac{1}{4}(\cosh 2r + \sinh 2r), \qquad (2.60)$$

$$\langle \hat{Y}\rangle = (\cosh r - \sinh r)|\alpha|\sin\phi_i, \qquad (2.61)$$

$$\Delta \hat{Y}^2 = \frac{1}{4}(\cosh 2r - \sinh 2r), \qquad (2.62)$$

In order to make a succinct expression, from now on, we assign G_{PSA} to denote the maximal PSA gain: $G_{PSA} = G_{PSA}^{max} = (\cosh r + \sinh r)^2 = \cosh 2r + \sinh 2r = e^{2r}$.

Then the above equations can be condensed to

$$\langle \hat{X} \rangle = \sqrt{G_{\text{PSA}}} \langle \hat{X}_i \rangle, \tag{2.63}$$

$$\Delta \hat{X}^2 = G_{\text{PSA}} \Delta \hat{X}_i^2, \tag{2.64}$$

$$\langle \hat{Y} \rangle = \frac{1}{\sqrt{G_{\text{PSA}}}} \langle \hat{Y}_i \rangle, \tag{2.65}$$

$$\Delta \hat{Y}^2 = \frac{1}{G_{\text{PSA}}} \Delta \hat{Y}_i^2, \tag{2.66}$$

where we have used the fact that for an input coherent state with coherent amplitude α and phase ϕ_i, $\langle \hat{X}_i \rangle = |\alpha| \cos \phi_i$, $\langle \hat{Y}_i \rangle = |\alpha| \sin \phi_i$ and $\Delta \hat{X}_i^2 = \Delta \hat{Y}_i^2 = 1/4$. We learn from Eq. 2.63 to Eq. 2.66 that the amplitude quadrature always experiences amplification G_{PSA} , while the phase quadrature always experiences deamplifiction $1/G_{\text{PSA}}$. They are distinct from Eqs. 2.20 to 2.23 for the PIA, where both quadratures undergo the same amplifications not only for the mean but for the variance as well.

2.4.4 Single-mode squeezing

As opposed to the two-mode squeezing enabled by the PIA in Eq. 2.19 and in Fig. 2.2, the single-mode PSA is capable of generating single-mode squeezed states[6], as demonstrated in [58].

We again use a balanced HD detection to measure the single-mode squeezing. The output field $\hat{a}_f$ is combined with a strong LO field at a 50/50 beam splitter. Assume the LO is a coherent state with a coherent amplitude $\beta = |\beta|e^{\varphi_{\text{lo}}}$, then the measured variance of the intensity difference between the two outputs of the beam splitter is:

$$\Delta \hat{X}_g^2 = \frac{1}{4}|\beta|^2(\cosh 2r - \cos 2\varphi_{\text{lo}} \sinh 2r), \qquad (2.67)$$

where $\Delta \hat{X}_g^2$ denotes the variance of the generalized quadrature. Since the SQL of the HD measurement is $|\beta|^2/4$, the squeezing of the generalized quadrature would be

$$\text{SQZ}_g = 10 \log_{10}(\cosh 2r - \cos 2\varphi_{\text{lo}} \sinh 2r). \qquad (2.68)$$

This is the same as measuring the squeezing of the joint quadratures $\hat{X}_-$ and $\hat{Y}_+$ in Eq. 2.30 and Eq. 2.31.

In Fig. 2.8, we plot SQZ_g as a function of the LO phase φ_{lo} when $\cosh^2 r = 3$. We find that, when $\varphi_{\text{lo}} = \pi/2$, the measurement yields the variance of the amplitude quadrature $\hat{X}$ and, when $\varphi_{\text{lo}} = \pi$, the measurement yields the variance of the phase

---

[6]In this thesis, two-mode and single mode squeezing are referred to as two brands of squeezing involving two beams and only one beam respectively. They are not named in terms of spatial modes. As a matter of fact, both types of squeezing could be multi-spatial-mode as demonstrated in [58, 72].
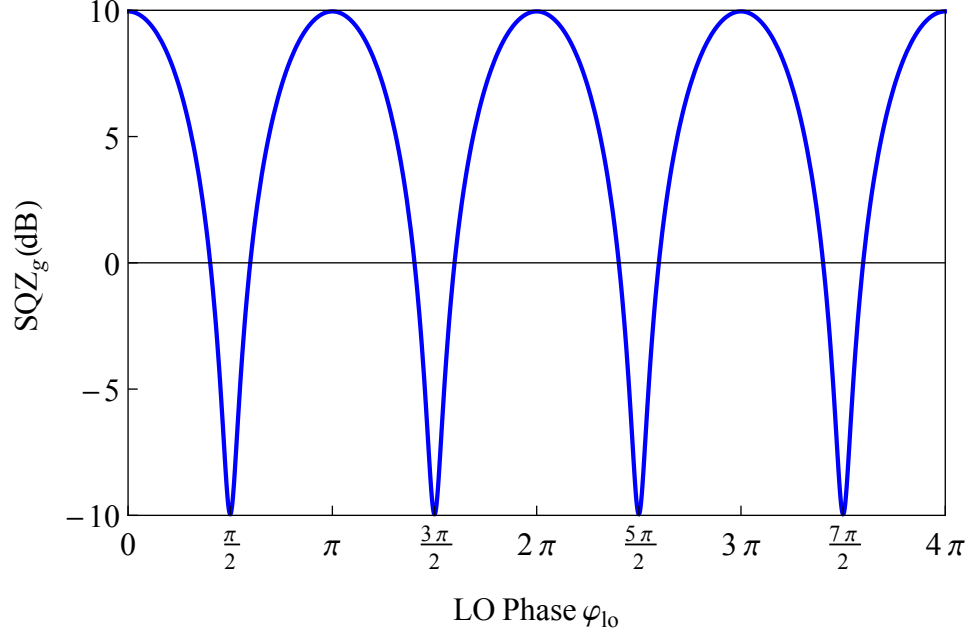
Figure 2.8: Squeezing of the generalized quadrature SQZ$_g$ as a function of LO phase φ_{lo} when $\cosh^2 r = 3$. The minima of the curve correspond to the squeezing value of the amplitude quadrature $\hat{X}$, while the maxima of the curve correspond to the anti-squeezing value of the phase quadrature $\hat{Y}$.

quadrature $\hat{Y}$. It clearly indicates the amplitude quadrature $\hat{X}$ is squeezed, while the phase quadrature $\hat{Y}$ is anti-squeezed by the same amount.

2.4.5 Noise figure of the single-mode phase-sensitive amplifier

From Eqs. 2.54 and 2.55 and $\mathrm{SNR}_{\mathrm{in}} = |\alpha|^2$ for an input coherent state with coherent amplitude α, the NF for the single-mode PSA can be reduced to

$$\mathrm{NF}_{\mathrm{PSA}} = \frac{\mathrm{SNR}_{\mathrm{in}}}{\mathrm{SNR}_{\mathrm{out}}} = \frac{\cosh 4r + \sinh 4r \cos \psi}{(\cosh 2r + \sinh 2r \cos \psi)^2}, \tag{2.69}$$

where $\psi = 2\phi_i - \theta = 2\phi_i - (\phi_b + \phi_c)$ is the relative input phase. This is exactly the same as the NF, Eq. 2.49, for the two-mode PSA. Therefore, if we were to plot

the gain, Eq. 2.56 and the NF of the single-mode PSA as a function of the relative input phase ψ, we have the identical behavior to that shown in Fig. 2.6.

2.5 Phase-space representations of phase-insensitive and phase-sensitive amplification

A more illustrative way of describing the gain and noise characteristics of a PIA and a PSA is to represent them in phase space. The phase-space representation of the phase-insensitive amplification of an input coherent state is depicted in Fig. 2.9 using Eqs. 2.20 to 2.23. Similarly, by using Eqs. 2.63 to 2.66, we depict the phase-space representation of the phase-sensitive amplification of an input coherent state in Fig. 2.10.

In phase space, the quantum noise of a coherent state input is represented by a disk of unit radius surrounding the vector extremity. The edge of the disk represents the $1/e$ isoprobability curve for the possible outcomes of a measurement. The area of the disk is directly given by the Heisenberg uncertainty principle, which for a coherent state obeys the relation:

$$\Delta X \cdot \Delta Y = 1, \qquad (2.70)$$

where X and Y are field quadratures in units of $\sqrt{\hbar\omega/2}$.

In Fig. 2.9, we see that the phase-insensitive amplification amplifies both quadratures by the same amount. All dimensions of the disk are magnified by
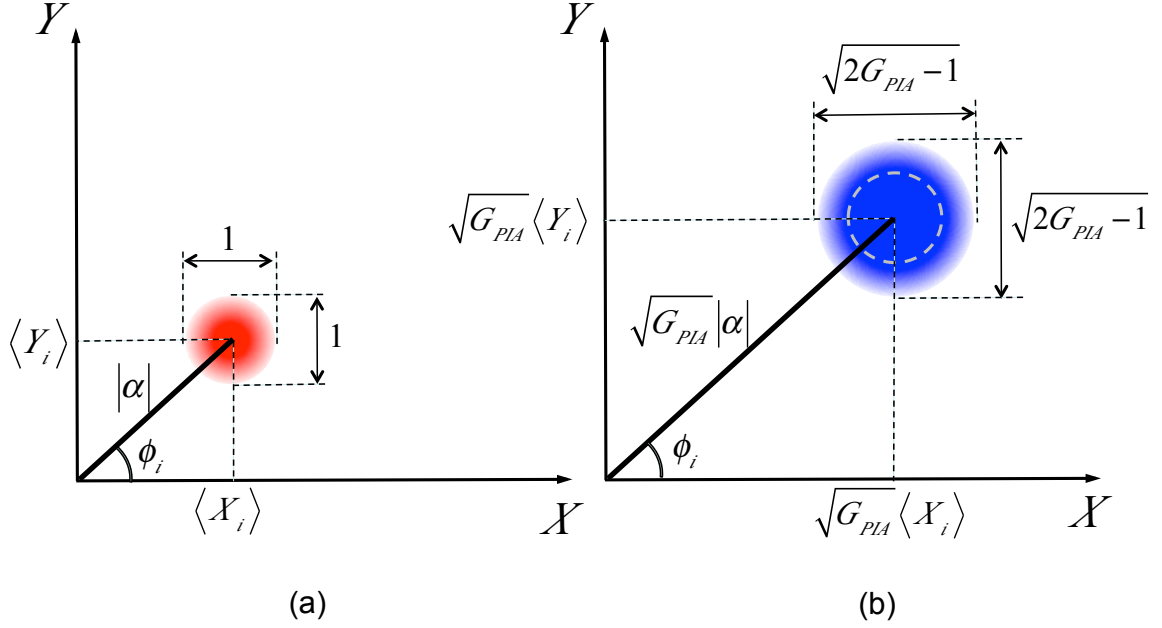
Figure 2.9: Phase-space representation of the phase-insensitive amplification (b) of an input coherent state (a). The dashed white circle in (b) designates the noise size of the input coherent state. $G_{\mathrm{PIA}} = \cosh^2 r$.

the same factor $\sqrt{2G_{\mathrm{PIA}} - 1}$. Thus the noise spot remains a disk (i.e., the noise power is the same in both quadratures), but its area is now larger, indicating that the amplifier has introduced excess noise beyond that required by the Heisenberg uncertainty principle in Eq. 2.70.

Whereas, in Fig. 2.10, when inputting a coherent state with an arbitrary input phase ϕ_i, a PSA amplifies both the mean and the noise in X, or amplitude quadrature but deamplifies the mean and noise in the orthogonal Y, or phase quadrature. By amplifying X quadrature and deamplifying the orthogonal Y quadrature, one distorts the noise spot into an ellipse, in contrast to the PIA configuration. However, in spite of the distortion, the area of the noise spot is unchanged and remains equal to the minimum required by the Heisenberg uncertainty principle.
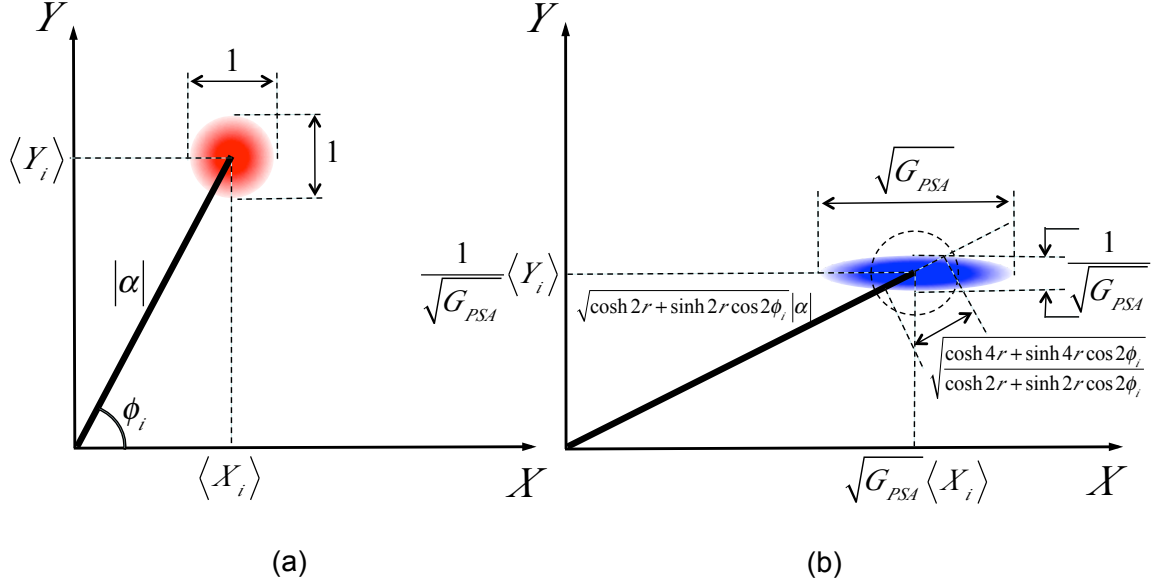
Figure 2.10: Phase-space representation of an arbitrary phase-sensitive amplification (b) of an input coherent state (a). The dashed black circle in (b) designates the noise size of the input coherent state. $G_{\text{PSA}} = e^{2r}$.

The maximal phase-sensitive amplification happens, according to Eq. 2.56, when the input phase $\phi_i = 0$ (again, assuming the input pump phases, ϕ_b and ϕ_c, sum up to 0). This corresponds to the case that only the X, or amplitude quadrature of the input coherent field carries a signal. The phase-space representation of the maximal phase-sensitive amplification of an input coherent state is shown in Fig. 2.11. In this case, we see that the phase-sensitive amplification amplifies both the signal and the noise in the X quadrature but deamplifies the noise in the orthogonal Y quadrature. The area of the noise spot is unchanged and remains equal to the minimum required by the Heisenberg uncertainty principle. The amplification thus operates in the quantum-limited regime. This means that no additional noise is introduced into the signal in the amplified X quadrature, thus resulting in $\text{NF}_{\text{PSA}} = 1$, which is associated with quantum-limited optical amplification.

43

We also plot the phase-space representation of the maximal phase-sensitive deamplification ($\phi_i = \pi/2$) of an input coherent state in Fig. 2.12 for completeness. This configuration has been implemented in our group to generate single-beam quadrature squeezed states with vacuum quadrature squeezing of -3 dB [58].
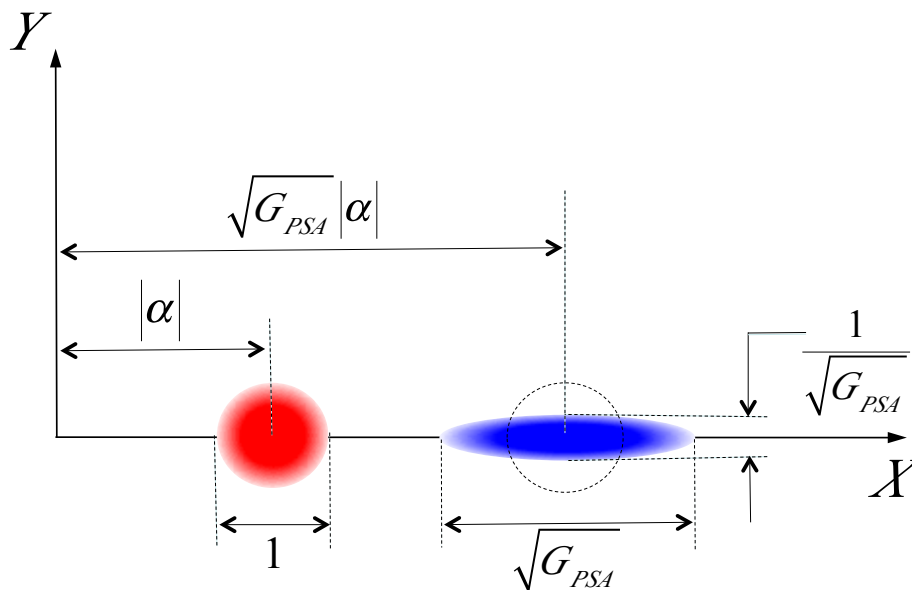
Figure 2.11: Phase-space representation of the maximal phase-sensitive amplification (blue) of an input coherent state (red). The dashed black circle designates the noise size of the input coherent state. $G_{\mathrm{PSA}} = e^{2r}$.
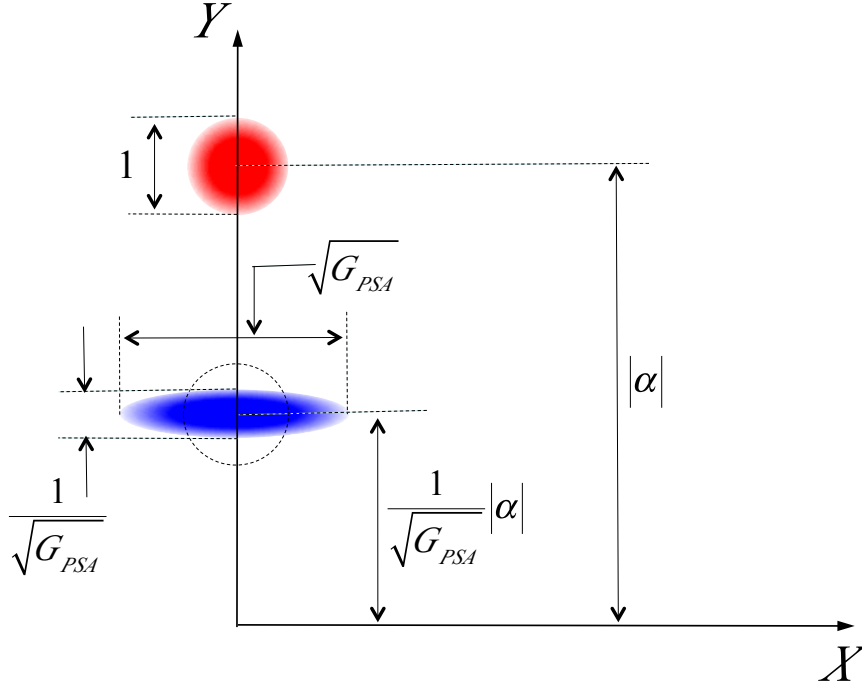
Figure 2.12: Phase-space representation of the maximal phase-sensitive deamplification (blue) of an input coherent state (red). The dashed black circle designates the noise size of the input coherent state. $G_{\mathrm{PSA}} = e^{2r}$.

2.6 Effect of losses

Realistic experiments are subject to sources of optical loss including surface reflections and absorption, as well as effective sources of loss such as imperfect detection efficiency. When one makes a measurement of a quantum state of light, it is important not only to reduce the losses experienced by the state but to understand how these losses affect the measurement. The effect of losses can be modeled by a beam splitter, as shown in Fig. 2.13, with a net transmission of η. In this case, the transformation of the annihilation operator, also known as the input-output relation
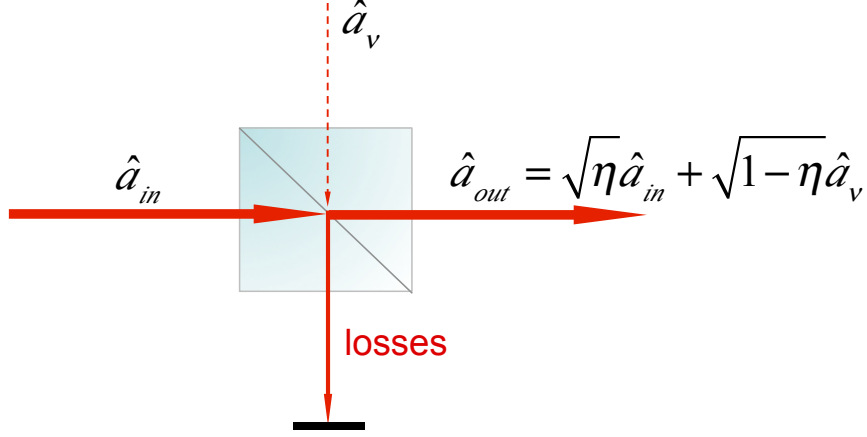
$$\hat{a}_{out} = \sqrt{\eta}\hat{a}_{in} + \sqrt{1-\eta}\hat{a}_v$$

Figure 2.13: Modeling of losses in the path of a beam or in an imperfect detection scheme by a beam splitter with a net transmission of η.

of the beam splitter is

$$\hat{a}_{out} = \sqrt{\eta}\hat{a}_{in} + \sqrt{1-\eta}\hat{a}_\nu, \tag{2.71}$$

where $\hat{a}_{in}$ is the annihilation operator of the quantum state before the losses, $\hat{a}_{out}$ is the annihilation operator associated with the quantum state after the losses, and $\hat{a}_\nu$ represents the annihilation operator of the vacuum noise that is coupled into the unseeded port of the beam splitter.

In order to demonstrate the effect of losses on the measurement of quantum features of a state of light, we take continuous-variable quantum entanglement as an example. We add two beam splitters with transmissions η_a and η_b to the output probe and conjugate modes to mimic the total losses before the detection, as shown in Fig. 2.14. Following the derivations in Section 2.3.2, the squeezing of the generalized quadrature in the presence of losses can be calculated as

$$\mathrm{SQZ}_{J_-} = 10\log_{10}[1 - \frac{\eta_a + \eta_b}{2} + \frac{\eta_a + \eta_b}{2}\cosh 2r + \sqrt{\eta_a}\sqrt{\eta_b}\cos 2\varphi_{\mathrm{lo}}\sinh 2r], \tag{2.72}$$
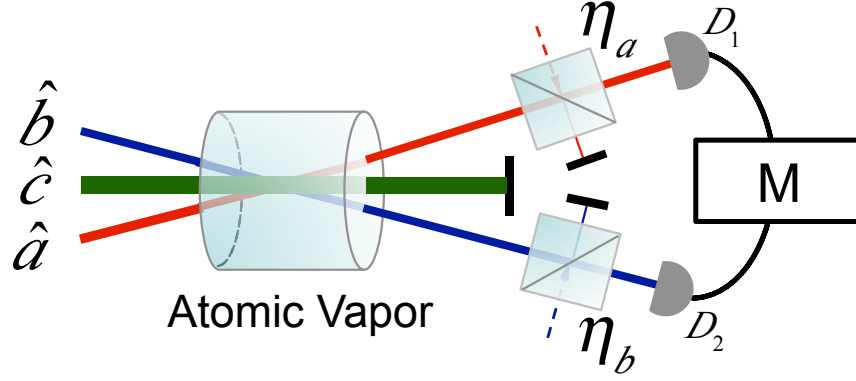
Figure 2.14: Total losses experienced by the output probe and conjugate modes before detection are mimicked by two beam splitters with transmissions η_a and η_b. D_1 and D_2 are two detectors which may be intensity detectors or homodyne detectors. M denotes the processing of the data.

$$\mathrm{SQZ}_{J_+} = 10\log_{10}[1 - \frac{\eta_a + \eta_b}{2} + \frac{\eta_a + \eta_b}{2}\cosh 2r - \sqrt{\eta_a}\sqrt{\eta_b}\cos 2\varphi_{\mathrm{lo}}\sinh 2r]. \quad (2.73)$$

In Fig. 2.15, we plot SQZ_{J_-} and SQZ_{J_+} as a function of the LO phase φ_{lo} when the PIA gain $G_{\mathrm{PIA}} = \cosh^2 r = 3$ with the presence of losses. We have assumed $\eta_a = \eta_b = \eta$ for simplicity. We find that, as we increase the losses, the level of squeezing is degraded accordingly, worsening the level of entanglement as expected. We also notice that, the reduction of the anti-squeezing level is less than the elevation of the squeezing level with the presence of loss, indicating the anti-squeezed joint quadratures $\hat{Y}_-$ and $\hat{X}_+$ are more robust to the loss than the squeezed joint quadratures $\hat{X}_-$ and $\hat{Y}_+$.
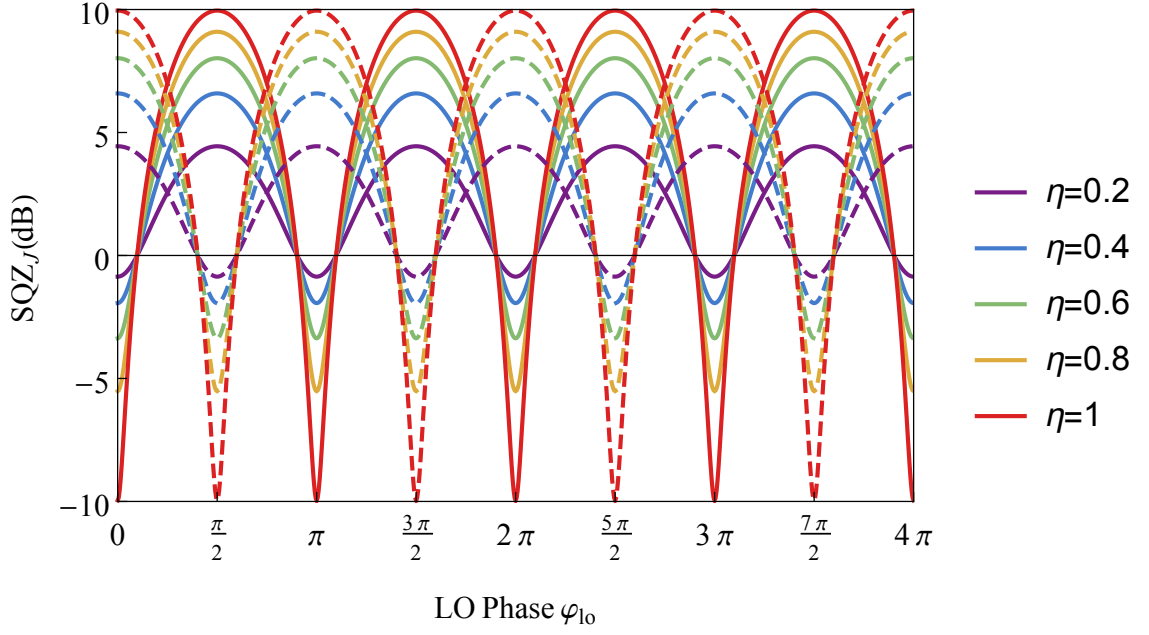
Figure 2.15: Squeezing of the generalized joint quadrature SQZ_{J_-} (dashed) and SQZ_{J_+} (solid) as a function of the LO phase φ_{lo} when the PIA gain $G_{\mathrm{PIA}} = \cosh^2 r = 3$ with the presence of losses $\eta_a = \eta_b = \eta$. The minima of the dashed curves correspond to the squeezing value of $\Delta\hat{X}_-^2$, while the minima of the solid curve correspond to the squeezing value of $\Delta\hat{Y}_+^2$.

Chapter 3: Effect of input phase modulation to a phase-sensitive optical amplifier[1]

3.1 Introduction

Acousto-optical modulators (AOMs) and electro-optic modulators (EOMs) are standard devices used in optics laboratories for frequency-shifting, amplitude-modulating, and phase modulating optical fields [73]. EOMs can provide phase modulation (PM) using the electro-optic response of a crystal, and can provide amplitude modulation (AM) when combined with polarizers. Achieving pure PM or AM using EOMs requires extreme care. Due to effects such as frequency-dependent interference and polarization rotation in birefringent crystals, PM is often accompanied by residual AM and vice versa [74, 75]. Techniques have been developed for combining multiple EOMs to impart an arbitrary mixture of AM and PM on light or to suppress the unwanted modulation [75].

Driving an AOM with modulated radio frequency can also be used to add AM to the output light in either the zeroth or first diffracted order. This method can also introduce some amount of PM to the light due to changes to the index of refraction

---

[1]This chapter is mainly based on the paper "Effect of input phase modulation to a phase-sensitive optical amplifier," *Opt. Express* **24**, 19871 (2016).

in the AOM crystal, such that the optical phase follows the acoustic phase [76, 77]. This situation, however, is rarely discussed. Many experiments and applications using AOMs are either phase-insensitive or otherwise unaffected by residual PM. Nevertheless, certain phase-sensitive processes are affected. Phase modulation from an AOM has been shown to be an experimental difficulty in some optical phase-sensitive amplifier (PSA) experiments [72, 78]. In particular, while the PSA can perform completely noiseless amplification of a particular field quadrature, it can also convert PM to AM, making signal-to-noise ratio (SNR) measurements hard to interpret. It can even lead to apparent increases in the SNR after amplification if inadvertent PM is closely tied to an applied AM signal, as is the case in using many modulation devices.

While AM can be measured with direct detection methods, PM can only be detected using more complicated phase-sensitive or interferometric measurement techniques, and can therefore be difficult to detect and eliminate. Common techniques for measuring the AM and PM of optical beams include homodyne and heterodyne detection [75, 79]. More indirect methods also exist for converting PM to AM such as using differential absorption in a sample [74], reflected light from a cavity [80], phase conjugation methods [81], or Brillouin scattering [82]. Phase modulation is often used in optical communication, such as in phase-shift keying. Signals from phase-shift keying are often demodulated using homodyne or heterodyne techniques and phase sensitive amplifiers have been investigated for regeneration of phase keyed signals [83]. A theoretical and experimental examination of a single-ended coherent receiver based on a phase sensitive fiber parametric amplifier, including a comparison

to a single-ended homodyne detector, has been presented in [84]. Our emphasis in this work is on detecting and quantifying unintended phase modulations introduced by commonly used free space optical modulators.

In this chapter, we explore the effects of PM on the output of an optical quantum-noise-limited PSA, where the phase of the input light is central to amplifier behavior. We study the effects of phase modulation on a PSA both theoretically and experimentally. We introduce a novel method for quantifying the PM depth on an input light field using the PSA as part of a phase-sensitive detector. This method relies on the differing gains of the AC and DC components of the PSA output intensities with a PM input. We compare the results of this method with the results of homodyne detection (HD), a standard method for measuring the quadratures of a light field. We then insert a mechanical chopper in our experiment to amplitude-modulate a laser beam and use our PSA detection method to find PM in this field. We find that this detection method is suitable for detecting phase modulation and that the results for the PSA output match well with our theoretical predictions. We also note that for experiments already employing a PSA, this method allows one to recognize and correct for the presence of PM on the input signal.

3.2   Theoretical predictions

In this section, we provide a classical theoretical framework to describe the effect of PM to the output of a PSA and discuss the possibility of utilizing the PSA itself to quantify the PM. We also derive the theoretical predictions for a homodyne

detection scheme measuring the PM on an input beam of light.

3.2.1 Phase-sensitive amplification

In this subsection we describe the operation of a PSA and predict the effect of phase and amplitude modulation on the outputs. Our optical PSA amplifies or deamplifies an optical waveform with a gain dependent on the phase of the input light. The phase of the input field is relative to two strong pump fields (see Fig. 2.7(b)) that drive the nonlinear process that results in phase-sensitive amplification. Given an input field $E_{\text{in}} = |E_{\text{in}}|e^{i\phi}$, the relationship between the classical input and output field is given by

$$E_{\text{out}} = E_{\text{in}} \cosh r + E_{\text{in}}^* \sinh r, \tag{3.1}$$

where r is the interaction strength of the parametric process derived from the product of the pump power, nonlinear susceptibility, and interaction length [85]. In our case, the phase of the process is defined by $\phi_{\text{PSA}} = 2\phi - (\phi_1 + \phi_2)$, where ϕ_1 and ϕ_2 are the pump phases[2]. Therefore, the output intensity $I_{\text{out}} = E_{\text{out}} \cdot E_{\text{out}}^*$ is a function of input phase ϕ, making the output phase-sensitive. We define the phase-dependent gain of the PSA as $g(\phi) = I_{\text{out}}(\phi)/I_{\text{in}}$. This leads to a maximum of the phase-dependent gain of $G = g(0) = e^{2r}$ and a minimum of $1/G = g(\pi) = e^{-2r}$. Because the gain of the PSA changes with input phase, the output intensity will be affected by the presence of phase modulation on the input beam, and this effect

---

[2]See Section 2.4.3 in Chapter 2 for detailed derivations. There, the phases of the two pumps are denoted by ϕ_b and ϕ_c, and the phase of the probe is denoted by ϕ_i.

must be included.

We now consider the case of a modulated input field. We adopt the definitions used in [79] for an electric field in the rotating carrier frame with both amplitude and phase modulation:

$$E_{\text{in}} = [1 - \frac{A}{2}(1 - \cos \Omega t) + i\frac{P}{2}\cos \Omega t]e^{i\phi}. \tag{3.2}$$

Note that we have set $|E_{\text{in}}| = 1$. Ω is the modulation frequency and A and P are the AM and PM modulation depths respectively with $A \ll 1$ and $P \ll 1$.

This input field has a sine-wave modulation on top of a constant offset, and so we can refer to as the AC and DC components of the field. The intensity of the input field (expanded to the second order of A and P) is

$$I_{\text{in}} = E_{\text{in}} \cdot E_{\text{in}}^* = \frac{1}{8}[8 + A(-8 + 3A) + P^2 - 4A(-2 + A)\cos \Omega t + (A^2 + P^2)\cos 2\Omega t]. \tag{3.3}$$

After the PSA, both the AC and DC components will be amplified or deamplified depending on the input phase ϕ, the intensity of the output field (also expanded to the second order of A and P) is

$$I_{\text{out}} = \frac{1}{8}[8 + A(-8 + 3A) + P^2 - 4(-2 + A)A\cos \Omega t + (A^2 + P^2)\cos 2\Omega t]\cosh 2r +$$

$$\frac{1}{8}\{[8 + A(-8 + 3A) - P^2 - 4(-2 + A)A\cos \Omega t + (A^2 - P^2)\cos 2\Omega t]\cos 2\phi +$$

$$[4P(-2 + A - A\cos \Omega t)\cos \Omega t]\sin 2\phi\}\sinh 2r. \tag{3.4}$$

Since $A \ll 1$ and $P \ll 1$, Eqs. (3.3) and (3.4) can be further simplified to be

$$I_{\text{in}} = 1 - A(1 - \cos \Omega t), \tag{3.5}$$

and

$$I_{\text{out}} = (1 - A + A \cos \Omega t) \cosh 2r + [(1 - A + A \cos \Omega t) \cos 2\phi - \tag{3.6}$$
$$(P \cos \Omega t) \sin 2\phi] \sinh 2r.$$

Due to the presence of PM, the AC and DC components can experience different gains. We define $g^{\text{AC}}(\phi) = I_{\text{out}}^{\text{AC}}(\phi)/I_{\text{in}}^{\text{AC}}$ and $g^{\text{DC}}(\phi) = I_{\text{out}}^{\text{DC}}(\phi)/I_{\text{in}}^{\text{DC}}$, where $I_{\text{in/out}}^{\text{AC}}$ and $I_{\text{in/out}}^{\text{DC}}$ are the AC and DC parts of the input and output intensities, respectively. They are defined as

$$I_{\text{in/out}}^{\text{AC}} = I_{\text{in/out}}^{\max} - I_{\text{in/out}}^{\min}, \tag{3.7}$$

$$I_{\text{in/out}}^{\text{DC}} = \frac{1}{2}(I_{\text{in/out}}^{\max} + I_{\text{in/out}}^{\min}), \tag{3.8}$$

where $I_{\text{in/out}}^{\max}$ and $I_{\text{in/out}}^{\min}$ are the maximum and minimum of the input and output intensities, respectively. For pure AM ($P = 0$), $g^{\text{AC}}(\phi) = g^{\text{DC}}(\phi)$, implying that the AC and DC components of the input intensity will be equally amplified/deamplified at any given input phase. However, this will not be the case when $P \neq 0$, and so we can compare $I_{\text{out}}^{\text{DC}}(\phi)$ with $I_{\text{out}}^{\text{AC}}(\phi)$ to detect and quantify phase modulation.

As an example, see the curves in Fig. 3.1 which show the PSA AC and DC gains for five different input signals, all with the same level of AM but varying levels of PM. In the experiment, the degree of AM modulation is easily determined by direct
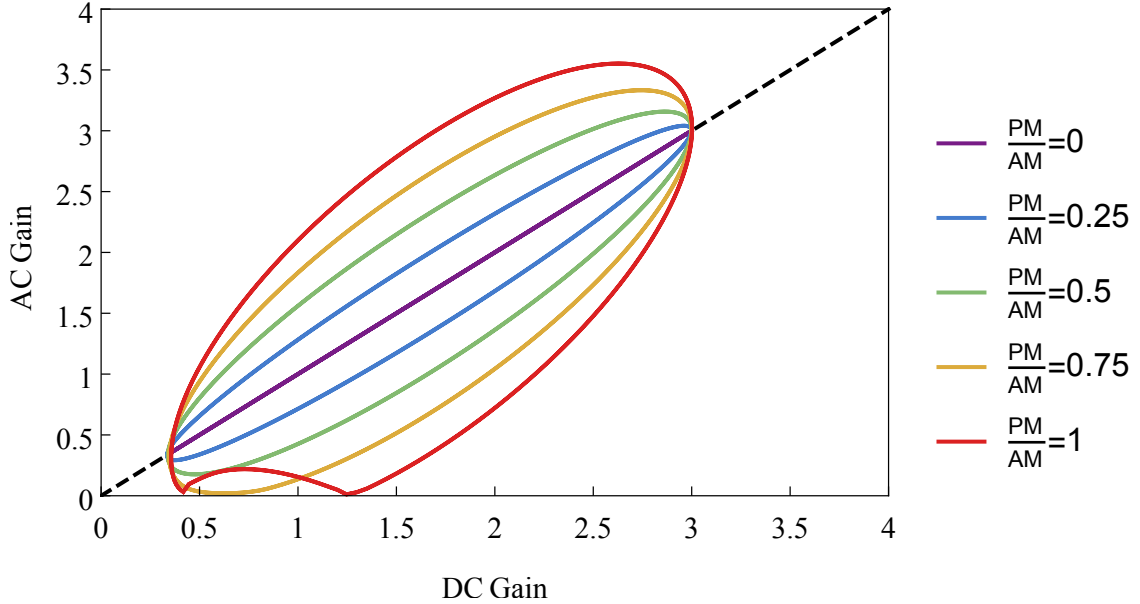
Figure 3.1: PSA theoretical plots: AC gain versus DC gain for an optical signal with a sine wave modulation and amplified in an optical phase-sensitive amplifier. Each plot is parametric with respect to the phase ϕ of the PSA. The different plots are for different mixtures of AM and PM. All curves shown here have $A = 0.16$ and a maximum PSA gain of $G = e^{2r} = 3$.

intensity measurements without the PSA. The goal here is to mimic experimental data (discussed below) from measurements on input signals resulting from slightly different alignments of an AOM, all producing the same level of AM. All five theory curves shown here have $A = 0.16$ and a maximal PSA gain of $G = e^{2r} = 3$.

By letting ϕ range from 0 to 2π, we get a parametric plot of the AC versus DC gains for all phases. Note that if P is zero (the purple curve in Fig. 3.1), we see a straight line with a slope of unity. On the other hand if P is a substantial fraction of A, this implies the presence of PM, and we see an oval as the phase is scanned due to the unequal amplifications of the DC and AC components. For large values of P the oval has negative AC gain values but we simply plot the absolute value.

One might also note that, the apparent maximal AC gain exceeds the set value 3. This is because PSA mixes the two quadratures of the AC components. When P is a substantial fraction of A, in addition to amplifying both quadratures of the AC component, PSA also converts part of phase quadrature to amplitude quadrature, making the apparent maximal AC gain exceed the set value 3. Therefore, by detecting the modulated input and output states of a PSA, we can quantify the amount of phase modulation present by using the size and shape of this oval.

3.2.2 Balanced homodyne measurement

We now consider homodyne measurements of a signal with amplitude and phase modulation. Homodyne detection is the standard phase sensitive technique for measuring the amplitude and phase quadratures of a light field (see Fig. 2.3 in Section 2.3 of Chapter 2). We will use it below to look at the same input signals as were measured by the PSA technique (Fig. 3.1) in order to verify the conclusions drawn from those measurements.

To perform homodyne measurements, the signal beam is combined with a reference local oscillator (LO) field $E_{\mathrm{LO}} = A_{\mathrm{LO}} e^{i\phi_{\mathrm{LO}}}$ on a 50/50 beam splitter, after which a balanced detection of the output intensities is performed. Depending on the phase of the reference beam ϕ_{LO} compared to the signal phase, the homodyne output will be sensitive to either the amplitude or phase of the signal light. For the modulated input state as in Eq. (3.2), it can be shown that the subtracted

photocurrent is proportional to

$$i_{\text{out}}^- = 2A_{\text{LO}}(A-2)\sin(\phi_{\text{LO}}-\phi)+2A_{\text{LO}}[P\cos(\phi_{\text{LO}}-\phi)-A\sin(\phi_{\text{LO}}-\phi)]\cos\Omega t. \quad (3.9)$$

The first term varies with ϕ_{LO} and is independent of the modulation frequency Ω, and will be referred to as the DC level. The second term is dependent on the modulation frequency and will have some AC level.

When the LO phase satisfies $\phi_{\text{LO}} = \phi + n\pi$, where n is an integer, the first term in Eq. (3.9) is 0, and the balanced HD output becomes $i_{\text{out}}^- = \pm 2A_{\text{LO}}P\cos\Omega t$, $+$ and $-$ are for the even and odd n's, respectively. The output is a sine wave at the modulation frequency whose amplitude is determined by only the PM depth P and the LO strength A_{LO}. This is the point where the homodyne detector measures the phase quadrature. At $\phi_{\text{LO}} = \phi + n\pi/2$, it is sensitive to only the amplitude modulation.

Since $A \ll 1$, and for simplicity we set $A_{\text{LO}} = 5 > 1$, the DC level is $20\sin(\phi_{\text{LO}} - \phi)$ and the AC level is $10[P\cos(\phi_{\text{LO}} - \phi) - A\sin(\phi_{\text{LO}} - \phi)]$. In Fig. 3.2, we plot the AC level as a function of the DC level while ϕ_{LO} is scanned over the full range. Note that we have normalized the DC level from -1 to 1. The plots are double valued in general because there are two values of ϕ_{LO} that correspond to the same DC level. The curves plotted here are for the same input signals as in Fig. 3.1, and thus all have the same level of AM ($A = 0.16$).
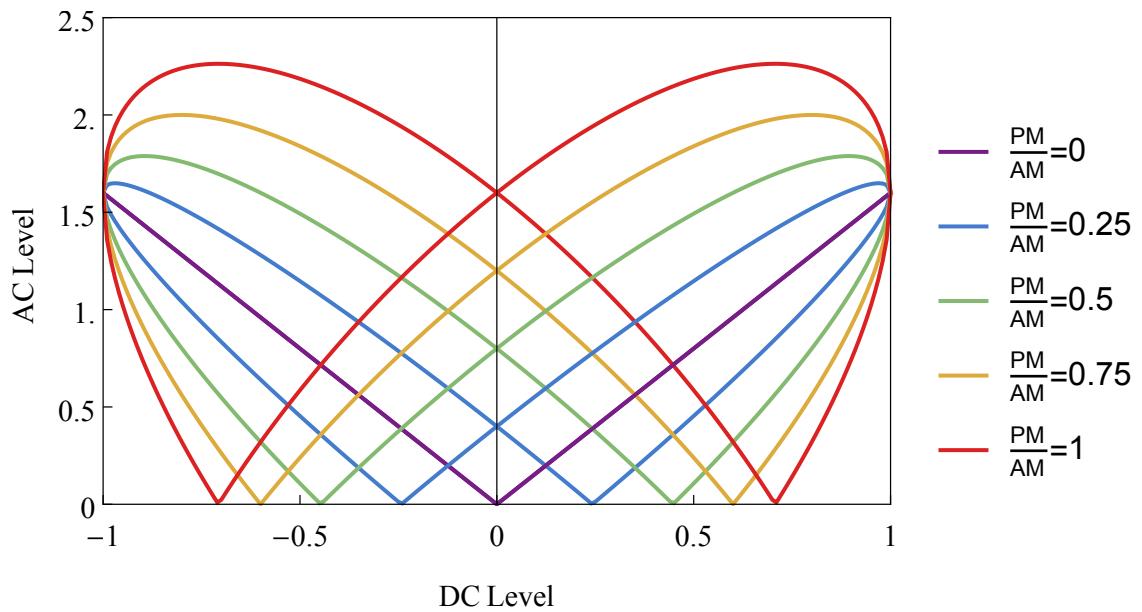
Figure 3.2: Homodyne theoretical plots: AC level versus DC level for an optical signal with a sine wave modulation and measured with a balanced homodyne detector. Each plot is parametric with respect to the phase ϕ_{LO} of the LO. The different plots are for different mixtures of AM and PM. All curves shown here have $A = 0.16$.
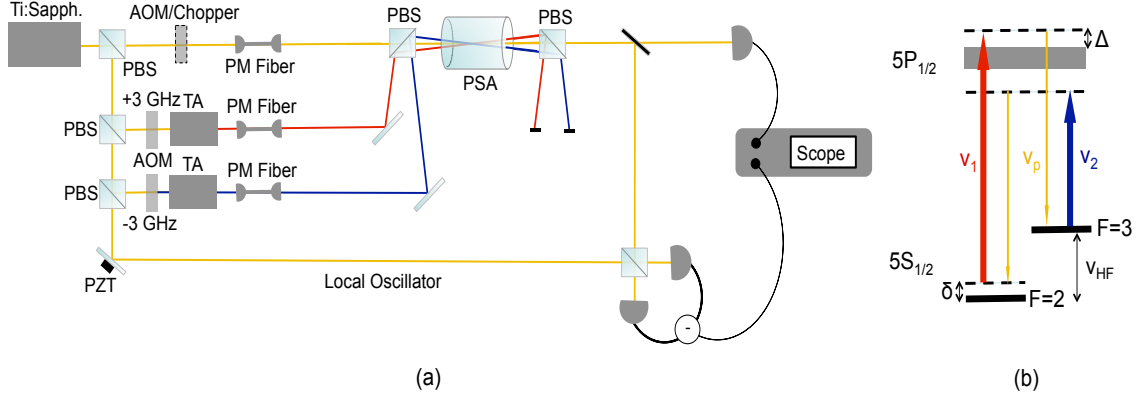
Figure 3.3: (a). Experimental setup. AOM: acousto-optic modulator, TA: semiconductor tapered amplifier, BS: non-polarizing beam splitter, PBS: polarizing beam splitter. (b). Level structure of the D_1 transition of ^{85}Rb and the optical frequencies arranged in the double-Λ configuration. Here ν_1 and ν_2 are the pumps and ν_p is the probe. The width of the excited state in the level diagram represents the Doppler broadened line, Δ is the one-photon detuning, δ is the two-photon detuning, and ν_{HF} is the hyperfine splitting.

3.3 Experimental setup

A diagram of our experiment is shown in Fig. 3.3. The PSA is created through the four-wave mixing (4WM) process in ^{85}Rb vapor. The signal probe beam is detuned from the D_1 line (795 nm) of Rb while two strong pump beams with frequencies ± 3 GHz from the probe intersect it at a small angle within the atomic vapor. We insert either an 80 MHz AOM or an optical chopper into the probe beam path before the PSA cell to modulate the input light. Before being aligned into the PSA vapor cell, the modulated input beam passes through a single-mode polarization-maintaining fiber. The input probe beam after the fiber is 200 μW with a $1/e^2$ beam waist of 250 μm. The pump beams have a $1/e^2$ beam waist of 550 μm and each has a power of 100 mW. The 12.5 mm vapor cell is filled with isotopically pure

^{85}Rb and heated to 87 °C. All the data shown in this chapter is taken with the probe beam blue detuned 1.4 GHz from the center of the $5S_{1/2}$ $F = 3$ manifold to the center of the $5P_{1/2}$ Doppler-broadened transition. The pump beams are created by seeding two 0.5 W tapered amplifiers with light that has been shifted ± 3 GHz using double-passed AOMs. The probe frequency is always centered between the two pumps. The chosen detunings result in a -4 MHz two-photon detuning for the probe and each pump compared to the exact hyperfine splitting of the ground state, in order to compensate for light shifts (see Fig. 3.3(b)).

3.4 Experimental results

We demonstrate, in this section, the experimental results obtained by using the two detection schemes elaborated in prior section to measure the PM introduced by a AOM and by a mechanical chopper to an input beam of light.

3.4.1 Acousto-optical modulator

We have found that when using the AOM to amplitude-modulate a light beam, the amount of (unintended) PM is highly dependent on the AOM alignment relative to the input beam while the degree of AM is not. For present purposes the degree of AM can be determined by direct intensity detection without the PSA or homodyne detector and thus we take it as a fixed parameter in our fits to the PSA and homodyne data. For a given alignment through the AOM, we can switch between detecting the light using HD or sending it into the PSA. The input beam is
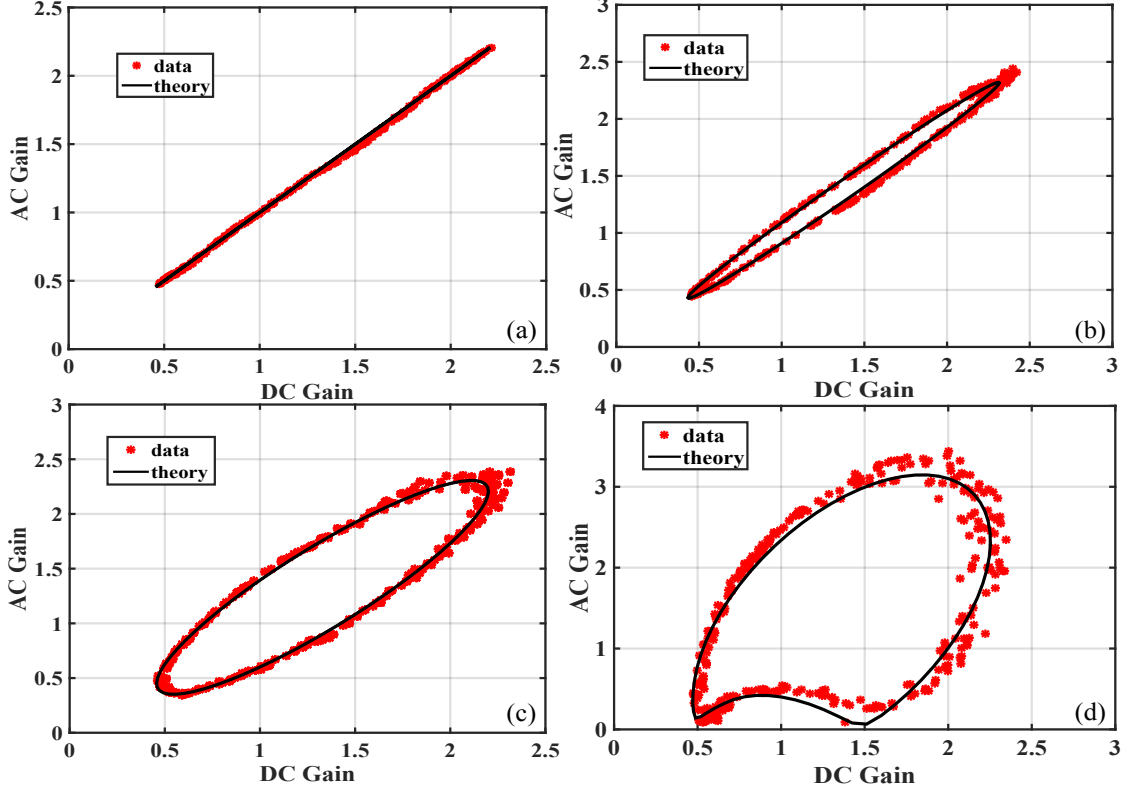
Figure 3.4: PSA results: AC gain versus DC gain for an optical signal modulated with an acousto-optic modulator and amplified in an optical phase-sensitive amplifier. The different plots are for different mixtures of AM and PM due to the AOM alignment. Each plot is parametric with respect to the phase of the PSA. The solid curves are theoretical fits with (a) $P/A = 0.00$, (b) $P/A = 0.11$, (c) $P/A = 0.50$, (d) $P/A = 1.65$.

modulated at 1 MHz with $A = 0.16$.

Figures 3.4 and 3.5 show measurements of PM at four different AOM alignments using the PSA method and HD method respectively. The alignment is changed by moving the horizontal tilt on the AOM. The stars are the experimental data while the solid lines are the theoretical fits using Eqs. (3.1), (3.2) and (3.9).

For the data in Fig. 3.4, the input and pump phases are allowed to drift such that each data point represents a shot of the experiment at a different PSA phase, and therefore a different $g(\phi)$. The PSA measurements give a well-defined shape

61
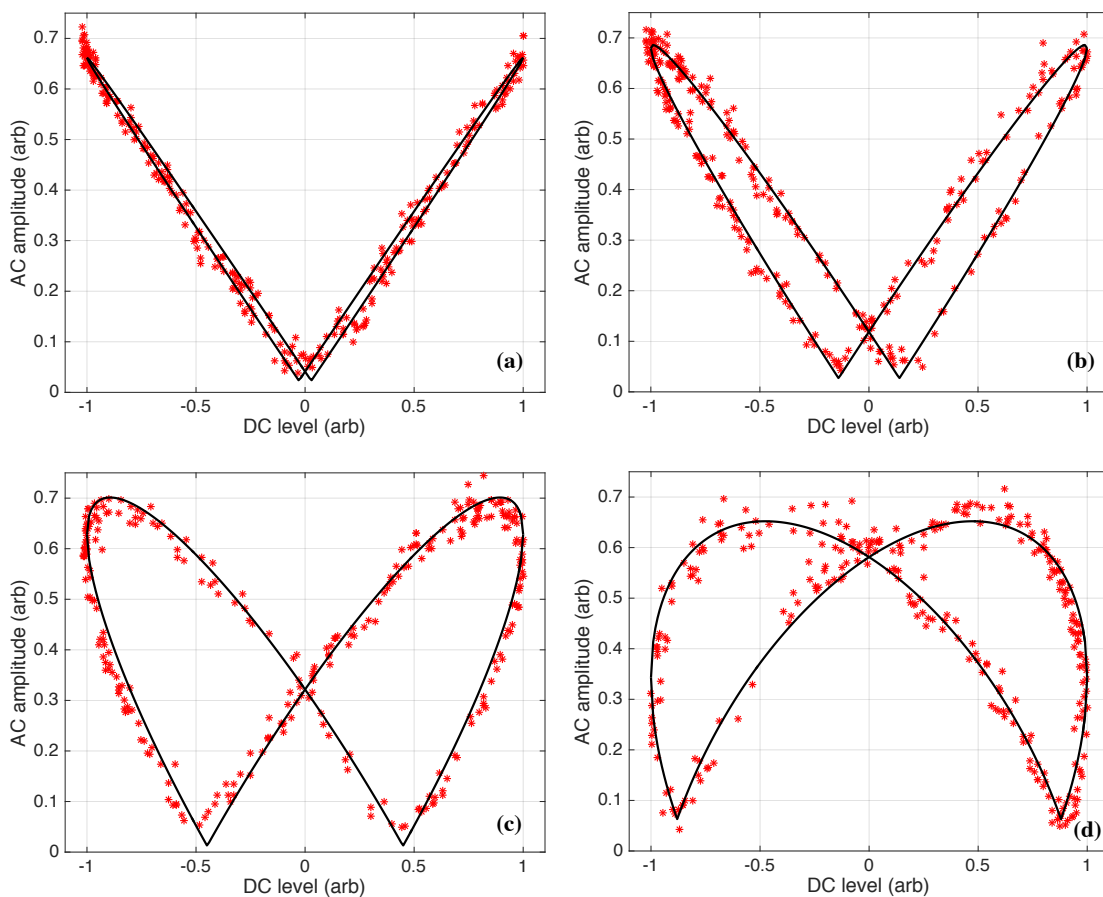
Figure 3.5: Homodyne results: AC level versus DC level for an optical signal modulated with an acousto-optic modulator and measured with a balanced homodyne detector. The different plots are for different mixtures of AM and PM due to the AOM alignment. Each plot is parametric with respect to the phase of the LO. The solid curves are theoretical fits with (a) $P/A = 0.03$, (b) $P/A = 0.14$, (c) $P/A = 0.50$, (d) $P/A = 1.85$.

which is a function of A, P, ϕ, and r. To fit the data, we took a subset of the data that could be plotted using a single-valued function of AC gain as a function of DC gain, rather than a parametric function of ϕ. To get a single valued function, we selected the data points corresponding to a span of π in PSA phase, which can be found by taking all the data points that lie above the line $y = x$ in Fig. 3.4. This data is then fit using the AC gain as a function of DC gain. The uncertainties for these measurements can be found in Fig. 3.6. The uncertainties are 95% confidence intervals from the fits. Due to systematic errors and our initial uncertainty in A, we have put lower bounds on the uncertainties corresponding to 1.5% uncertainty in P/A.

We find that by moving the tilt of the AOM less than one degree, we can change P/A from nearly zero to greater than 0.2. The AM alone is not appreciably changed for any of the data shown. Extremely fine tuning of the angle is required to find the minimum P/A. Unfortunately, aligning for highest diffraction efficiency does not guarantee minimum phase modulation.

In the case of the homodyne measurements, the shapes are a function of P and A from the second term of Eq. (3.9), as well as a scaling factor and a vertical offset. The data in these plots are for same input signals as in Fig. 3.4, and thus all have the same level of amplitude modulation ($A = 0.16$), and a variable level of phase modulation resulting from slight changes in the alignment of the acousto-optic modulator. To perform fits, we took a subset of the data that could be plotted using a single-valued function. To select data points consistent with a single valued function, we selected the data points corresponding to a span of π in LO phase.

Moving along the parametric curve in a single direction, from the minimum DC level to the maximum DC level, constitutes a π phase shift in the LO. Instead of a parametric function of ϕ, we can now plot AC level as a function of DC level and perform a standard fit. The uncertainties for these measurements can be found in Fig. 3.6. The uncertainties are 95% confidence intervals from the fits. Due to systematic errors and our initial uncertainty of A, we have put lower bounds on the uncertainties corresponding to 3% uncertainty in P/A.

By switching between the PSA measurement and the HD measurement without disturbing the AOM alignment, we can compare the two methods. In Fig. 3.6, we plot P/A for the HD measurement versus the PSA measurement. The AOM alignment was adjusted for each point to increase or decrease the amount of phase modulation, and thus the ratio P/A. We find that the PSA and HD method track each other linearly and are in substantial agreement. This shows that measurements with a phase-sensitive amplifier can act as a diagnostic tool for reducing phase modulation on a light field.

3.4.2 Optical chopper

Having confirmed that our analysis of the PSA data is consistent with that based on standard HD measurements, we can now use the PSA results alone. We consider here a common laboratory technique for amplitude modulating a beam, namely a mechanical chopper wheel which alternately blocks and un-blocks a beam. The spatial mode of the beam after the chopper is cleaned with a single mode
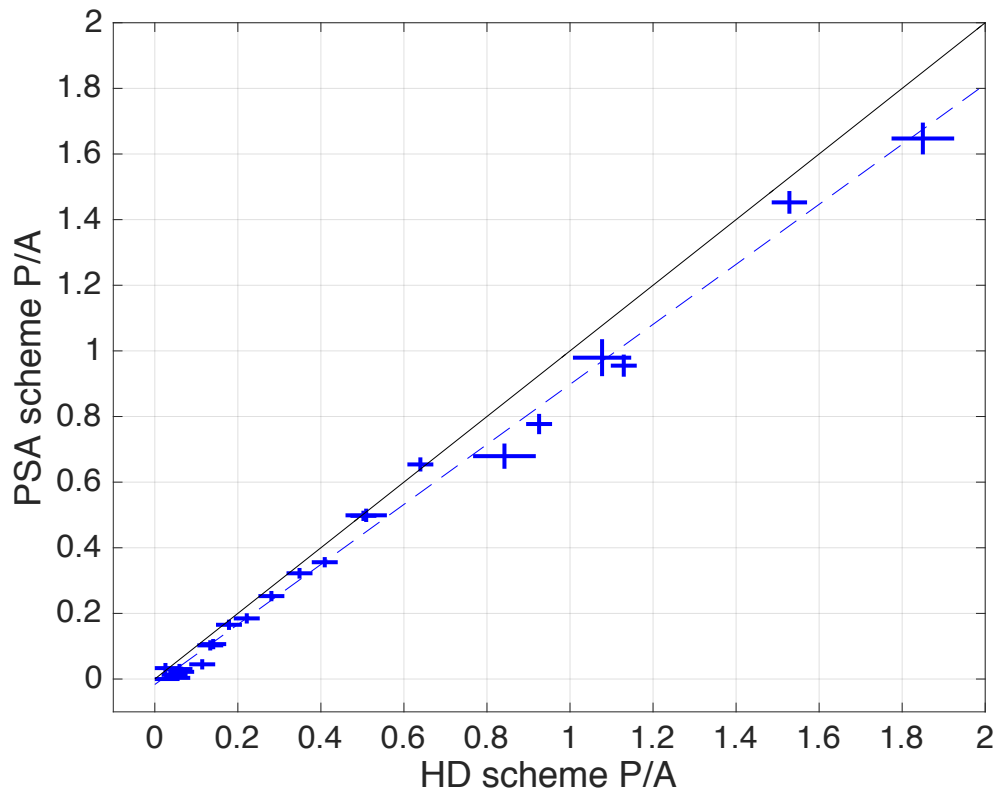
Figure 3.6: Comparison of the ratio of phase to amplitude modulation measured by homodyne detection and measurements of PSA AC and DC amplification. The solid line is $y = x$ and the dashed line is a best linear fit, $y = 0.91x - 0.02$, to the data.

fiber before the beam is sent into the PSA. We find the chopper introduces phase modulation as its blades cut through the beam. It may seem counter-intuitive that a chopper can add PM; however, as the blade passes through the beam, the spatial mode and phase front of the beam are disturbed due to diffraction effects around the blade. As the chopper moves through the beam, the light intensity will change with a transient, well-modeled by the error function.

The intensity as a function of time after a blade moving through a Gaussian beam is given by

$$I_{\text{in}} = \frac{1}{2}[1 + erf(\frac{t-\mu}{\sqrt{2}\sigma})], \tag{3.10}$$

where t is time, μ is the offset and σ is the width of the error function. We use this function to fit the intensity transient of the input beam, as shown in Fig. 3.7, where the thick light blue curve and the dark blue dashed line are the data and fit respectively.

We introduce a simple empirical model for the phase modulation which we can test with the PSA measurements. We assume that any phase modulation introduced to the light follows a Gaussian function in time as the blade traverses across the beam profile, with a width that matches the error function of the intensity:

$$E_{\text{in}} = e^{i\phi}\sqrt{\frac{1}{2}[1 + iPe^{-(\frac{t-\mu}{\sqrt{2}\sigma})^2}][1 + erf(\frac{t-\mu}{\sqrt{2}\sigma})]}. \tag{3.11}$$

In this case, P corresponds to the maximum amplitude of the Gaussian shaped PM. We find the values of μ and σ by fitting Eq. (3.10) to the measured transient
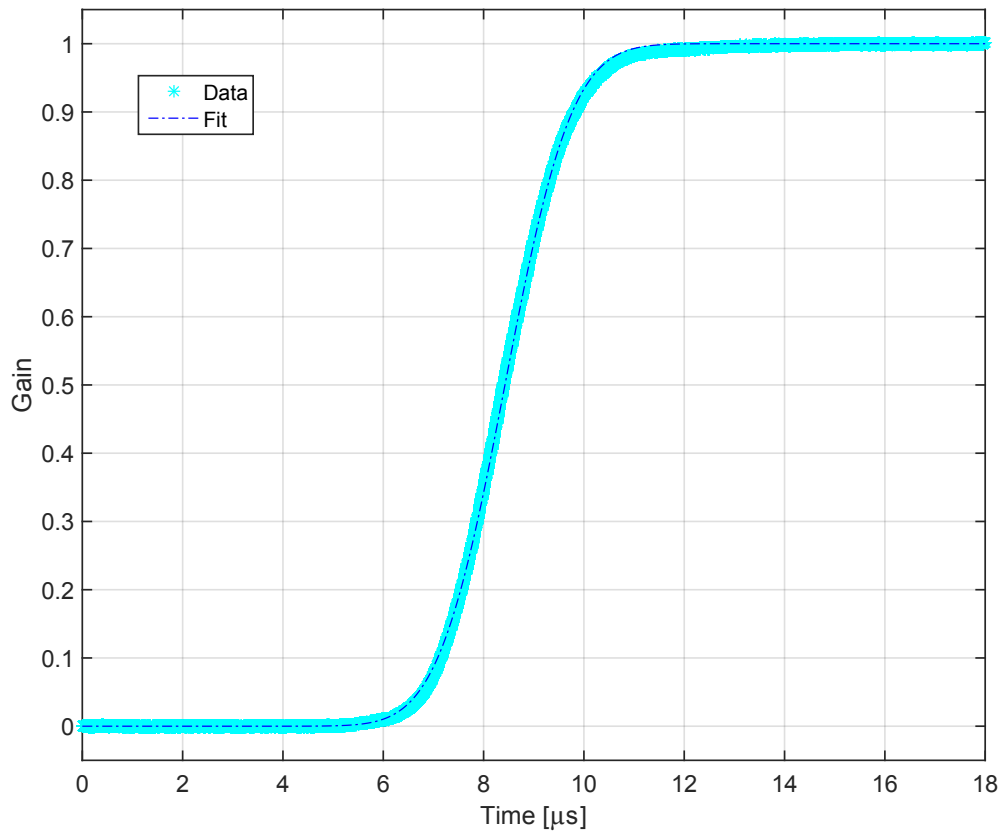
Figure 3.7: Intensity transient data (thick light blue curve) and fit (dark blue dash-dotted line).

intensity of the input beam (see the dashed curves in Figs. 3.8(a) and 3.9(a)). We define the AC part of the PSA output signal as the intensity integrated over the time window during which the transient turns from off to on; from 6 to 11 μs. The AC gain is defined as the ratio of the AC signal with the PSA on to the AC signal with the PSA off. The DC component is the steady state of the intensity after the light is fully unblocked. The DC gain is defined as the ratio of the DC signal with the PSA on to the DC signal with the PSA off. Just as when using an AOM, the discrepancy between AC and DC gain is indicative of the level of PM. This allows us to plot the AC intensity component versus the DC level and extract a PM depth. We believe the deviation between theory and experiment is mostly due to our assumption of the Gaussian form of the PM above and the slight mechanical instability of the chopper from shot-to-shot.

We found that the phase modulation of a chopper depended strongly on the tilt of the chopper blades when they intersected the laser beam. Figures 3.8 and 3.9 show the results of the PSA measurements for two tilts of an optical chopper. Figure 3.8(a) is the measurement when the blades are tilted off-axis by approximately 10 degrees from the beam path, and Fig. 3.9(a) shows the results when the blades intersect the beam path at normal incidence. Figures 3.8(b) and 3.9(b) are theory curves shown as examples to demonstrate curve shapes for the fit parameters and do not necessarily match the PSA phases of the individual data curves shown in Figs. 3.8(a) and 3.9(a). In both cases, the blades are placed within the Rayleigh range of a beam focus. From Fig. 3.10, it is evident that the phase modulation was reduced by setting the chopper to normal incidence, however PM may not be eliminated completely.
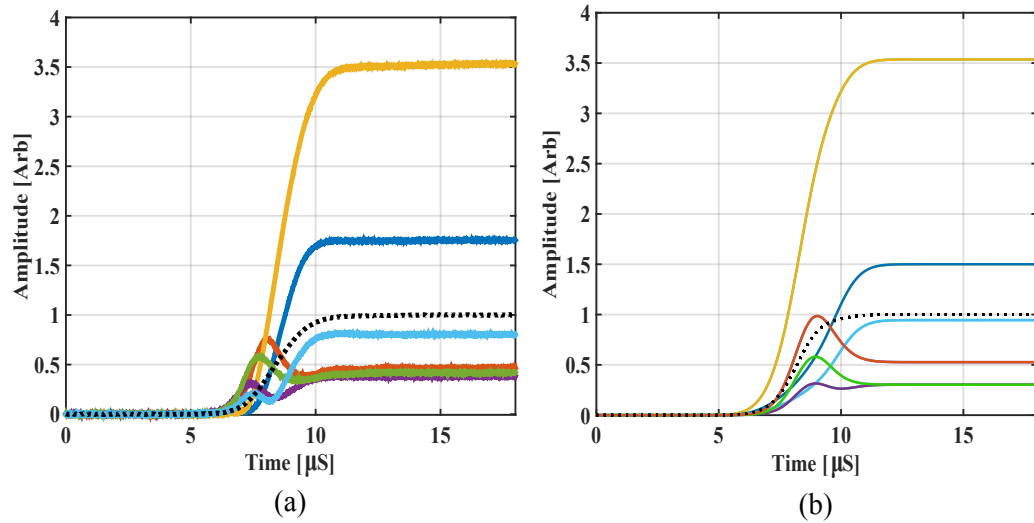
Figure 3.8: PM measurements for a tilted chopper alignment using the PSA scheme. (a) shows the raw data. (b) shows theory curves as examples to demonstrate curve shapes for the fit parameters and do not necessarily match the PSA phases of the individual data curves shown in (a). The dashed black lines are direct intensity detection without a PSA and the other curves are various phases of the PSA.
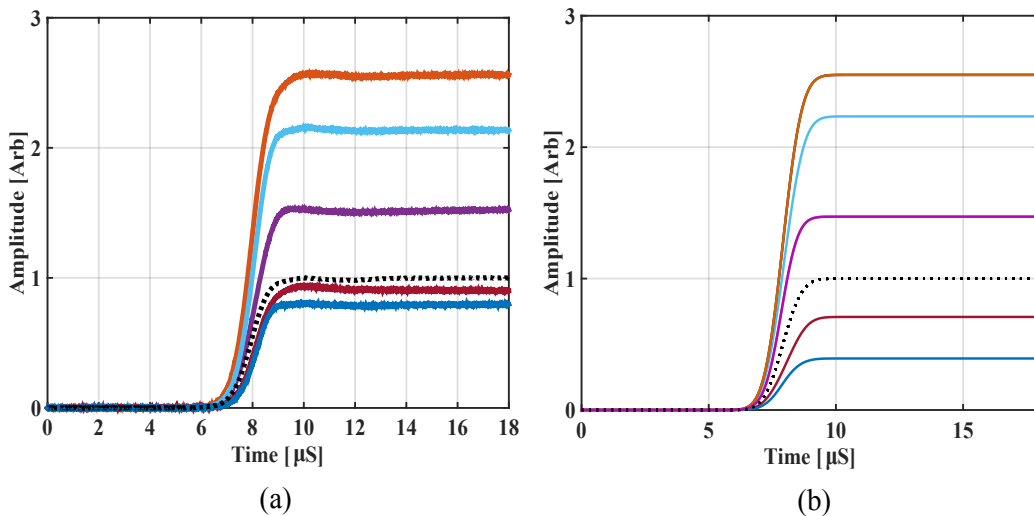
Figure 3.9: PM measurements for the optimal chopper alignment using the PSA scheme. (a) shows the raw data. (b) shows theory curves as examples to demonstrate curve shapes for the fit parameters and do not necessarily match the PSA phases of the individual data curves shown in (a). The dashed black lines are direct intensity detection without a PSA and the other curves are various phases of the PSA.
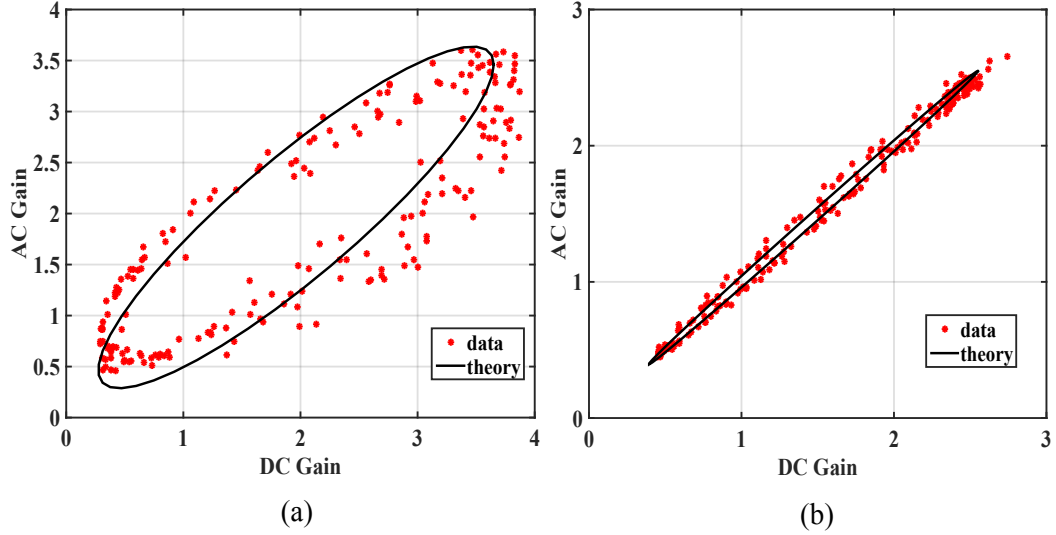
Figure 3.10: AC gain vs. DC gain, as defined in the text, for measuring the PM from a chopper. (a) is for the tilted chopper alignment shown in Fig. 3.8, and (b) is for the optimal chopper alignment shown in Fig. 3.9, respectively. The solid curves are theoretical fits where $P = 0.7$ in (a) and $P = 0.15$ in (b), respectively.

We were unable to reduce the amount of phase modulation below the level shown in Fig. 3.10(b).

3.5   Conclusions

These demonstrations highlight the importance of being able to measure and correct for the presence of unintended phase modulation when employing common amplitude modulation techniques in experiments using phase sensitive amplifiers. We show that PSA signals can be used as a diagnostic tool for quantifying the phase modulation depth of an input signal and are consistent with established homodyne techniques. We find that both AOMs and optical choppers can inadvertently add phase modulation to a light field in addition to the desired amplitude modulation.

This can drastically alter the results in applications using phase-sensitive amplifiers. In each case, the amount of phase modulation can be reduced by adjusting the angle of incidence between the beam path and the modulator. Similar analysis could be carried out using optical PSAs and light modulated by electro-optic devices.

Chapter 4: Improved measurement of two-mode quantum correlations using a phase-sensitive optical amplifier[1]

4.1 Introduction

Nonclassical states of light have a wide range of applications in precision measurements, quantum imaging, optical communications, and quantum information science [86]. A severe limitation in using these quantum states is their sensitivity to loss, because loss adds noise. Specifically, quantum properties of two-mode states, such as continuous variable entanglement or two-mode squeezing, are quickly degraded if one or both modes are subject to loss.

When significant downstream losses are present in a classical communication channel, classical amplifiers can be used before the loss to improve reception. An amplifier cannot increase the signal-to-noise ratio (SNR) of a communication channel, but it can increase the signal strength so that electronic noise in a receiver does not overwhelm the signal. The same concept can be applied to quantum communications. By adding the right kind of quantum-limited amplifier before downstream loss, selected properties of a quantum state can be maintained even in the presence

---

[1]This chapter is mainly based on the paper "Improved measurement of two-mode quantum correlations using a phase-sensitive optical amplifier," *Opt. Express* **25**, 21301 (2017).

of loss.

The most common type of amplifier is a phase-insensitive amplifier (PIA) which amplifies both quadratures of the input channel. A PIA necessarily has an open input port which admits vacuum noise, and in the limit of large PIA gain, the signal will suffer an SNR degradation of 3 dB (see Section 2.3 in Chapter 2 for details). In contrast, a phase-sensitive amplifier (PSA) with no open ports can noiselessly amplify one quadrature of the input. Provided the signal is encoded in the appropriate quadrature, the SNR remains unchanged [87] (see Section 2.4 in Chapter 2 for details).

One form of downstream optical loss is the imperfect quantum efficiency of a photodetector. The concept of using optical amplification to compensate for imperfect detection efficiency has been considered previously. It has been shown theoretically that by pre-amplifying the observed quadrature component of the input electric field, one can compensate for the non-unity detector quantum efficiency in a homodyne detector [88–92]. Experimentally, noiseless optical amplification has been used in the context of quantum non-demolition measurements [42, 43, 93–97]. In these experiments, noiseless amplification was used to overcome downstream propagation losses and non-unity detector quantum efficiency, although in each case the input signal before amplification was classical. Lam *et al.* [98] used an electro-optic feed forward scheme to produce an output state with an SNR close to that of the input state, outperforming a PIA. An amplitude squeezed state was used as the input to the device. Ulanov *et al.* [99] demonstrated using noiseless optical amplification to restore entanglement in the presence of loss in a probabilistic manner in the

photon-counting regime, i.e., entanglement distillation. Alon *et al*. [100] used a PSA to demonstrate phase-sensitive amplification and deamplification of a non-classical, quadrature-squeezed state.

In this paper we report the use of a quantum-limited optical PSA to pre-amplify one mode of a nonclassical two-mode state of light in order to overcome downstream optical losses for that mode. We make a systematic investigation of using a PSA to improve the measurement of correlations and squeezing levels that were present in the input state of light, in particular compensating for various levels of non-unity detector quantum efficiency. While Alon *et al*. [100] demonstrate a proof-of-principle experiment, here we investigate more fully the behavior with respect to varying loss in the system.

4.2   Conceptual diagram

Figure 4.1 shows the conceptual basis of the experiment. The source produces a quantum state with modes a and b whose properties we wish to measure. Measurements made by the detectors are contaminated by vacuum noise coupled in by optical losses (η_a and η_b). These losses include less-than-perfect detector efficiencies. Inserting a PSA in each arm, adjusted to amplify the desired quadrature, allows one to reduce the influence of the vacuum noise coupled in by the optical losses and thus make a better measurement of the quantum properties of the state of modes a and b. Depending on the measurement, the processing of the data may include electronic gain adjustments to compensate for the optical gain introduced by the
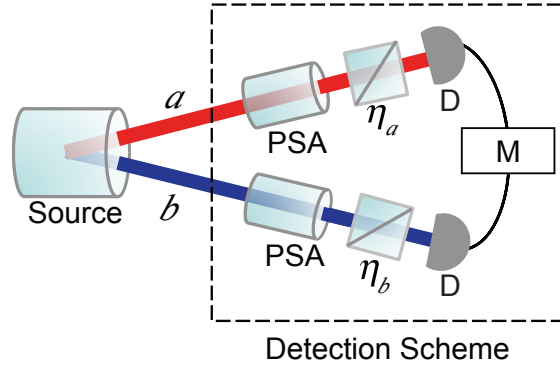
Figure 4.1: Conceptual schematic of the experiment. The source produces two modes a and b that are quantum correlated. The non-unity quantum efficiency of the detection and any other optical losses are symbolized by two beamsplitters with transmission η_a and η_b. D denotes ideal detectors with perfect quantum efficiency. M represents the processing of the detected signals to produce information about the quantum state in modes a and b.

PSAs.

For technical simplicity in our proof-of-principle experiment we use a single PSA and mitigate the effect of losses in only one arm of the apparatus. The detectors D are intensity detectors and the PSA is adjusted to amplify the intensity quadrature of the light in one arm. The quantum properties of the modes a and b which we choose to measure are the correlation coefficient of the optical intensities and the squeezing of the intensity difference between these two modes. To explore the effect of the PSA on these measurements we intentionally introduce a known loss after the PSA and record the effect that this loss has on the measured intensity correlation coefficient and twin-beam noise reduction, or intensity-difference squeezing, between the modes.

4.3 Experimental setup

A detailed description of our experiment is shown in Fig. 4.2(a). In the experiment, we use a PIA as the source. Both the source and the PSA are implemented using four-wave mixing (4WM) in ^{85}Rb vapor. Details of the source are discussed in [101] and of the PSA in [102]. In both cases, the ^{85}Rb atoms are contained in a 12 mm glass cell. The source and PSA cells are heated to 112 °C and 86 °C, respectively. Figure 4.2(b) shows the atomic energy levels and detunings used in the 4WM process of the source. We seed mode a_0 with a weak coherent beam (0.1 mW, 300 μm $1/e^2$ diameter) tuned to the probe frequency ν_p and let mode b_0 be the vacuum. The source is driven by a strong pump (350 mW, 800 μm $1/e^2$ diameter) that can be regarded as classical. The output modes a_i (at the probe frequency ν_p) and b_i (at the conjugate frequency ν_c), are quantum correlated [101]. Losses are modeled by beamsplitters with transmission η_{a1} and η_{b1}. These represent both losses inside the source cell as well as external losses. The calculation of loss (as well as gain) inside the source cell is discussed in the Appendix A. In the absence of the PSA and any intentionally introduced losses, we measure -5.8 dB of intensity-difference squeezing, which is roughly constant over an analysis frequency range of 0.5 MHz to 2.5 MHz.

Probe mode a_i passes through a second ^{85}Rb cell which is pumped by two strong classical pumps, one at ν_1 (the same as the source pump) and the other one at ν_2, approximately 6 GHz downshifted relative to ν_1, as shown in Fig. 4.2(c). The two pump beams (100 mW each, 500 μm $1/e^2$ diameter) and the probe beam are
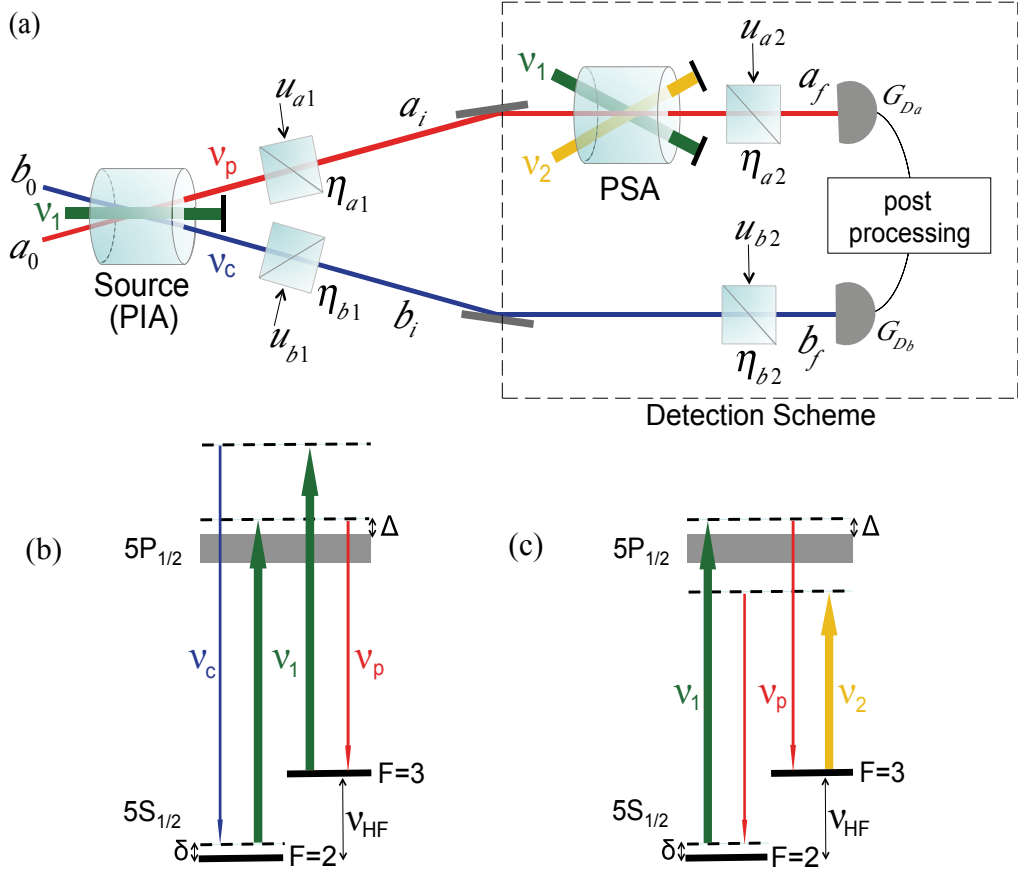
Figure 4.2: Experimental setup and 4WM schemes showing atomic energy levels in ^{85}Rb and laser tunings. (a) Experimental setup. The source (PIA) generates a two-mode squeezed state. η's are the transmissions of beamsplitters that represent losses: η_{a1} is the probe transmission before the PSA and η_{a2} is the probe transmission after the PSA representing all the downstream losses including imperfect detector efficiency. We vary the value of η_{a2} by intentionally introducing extra loss using a half-wave plate and a polarizing beamsplitter. The transmission η_{b2} includes the effect of imperfect detector efficiency on the measurement of the conjugate beam. G_{Da} and G_{Db} are the gains of the probe and conjugate detectors, respectively. (b) 4WM scheme in the source (PIA) cell. ν_p, ν_c and ν_1 are the optical frequencies of probe, conjugate and pump beams, respectively, and $\nu_p + \nu_c = 2\nu_1$. (c) 4WM scheme in the PSA cell. ν_1, ν_2 are the optical frequencies of the two pump beams, and ν_p is the optical frequency of the probe beam, and $\nu_1 + \nu_2 = 2\nu_p$. For both (b) and (c): the width of the excited state in the level diagram represents the Doppler broadened line, Δ is the one-photon detuning, $\delta = -4$ MHz is the two-photon detuning, and $\nu_{HF} = 3.036$ GHz is the hyperfine splitting in the electronic ground state of ^{85}Rb.

in a plane with an angular separation of 0.6 degrees between the pumps. The PSA implemented in this work is the same as in [102–104].

The probe field created in the source is amplified or deamplified in the PSA depending on the PSA phase

$$\phi_{\mathrm{PSA}} = 2\phi - (\phi_1 + \phi_2), \tag{4.1}$$

where ϕ_1 and ϕ_2 are the optical phases of the pump beams and ϕ is the probe optical phase[2]. Assuming that the input signal is encoded in a single quadrature, there are two choices of PSA phase for which the PSA will noiselessly amplify this input quadrature. For one choice, this quadrature intensity experiences a gain G_{PSA} and for the other, it experiences a deamplification $1/G_{\mathrm{PSA}}$. In our experiment we keep ϕ_{PSA} such that the input intensity of the probe beam always sees gain G_{PSA}. Since G_{PSA} is a function of pump power, one photon detuning Δ (see Fig. 4.2(c)), and the number density of ^{85}Rb atoms in the cell, adjusting these parameters allows us to vary G_{PSA}. In the experiment, we change the one photon detuning Δ to obtain different values for G_{PSA}.

All the downstream losses experienced by the probe after the PSA are modeled by a beamsplitter as shown in Fig. 4.2(a). Its transmission η_{a2} is determined by the transmission of the downstream optics including the exit window of the PSA cell, the quantum efficiency of the detector photodiode and an intentionally introduced extra loss from the combination of a half-wave plate and a polarizing beamsplitter.

---

[2]See Section 2.4.3 in Chapter 2 for detailed derivations. There, the phases of the two pumps are denoted by ϕ_b and ϕ_c, and the phase of the probe is denoted by ϕ_i.

An additional contribution to η_{a2} comes from the non-zero electronic noise floor of the detection electronics. The finite separation of the optical noise power from the detector electronic noise floor adds noise equivalent to that of an attenuator whose transmission is $1 - 10^{-\frac{S}{10}}$, where S is the noise power separation in dB [105]. Losses experienced by the conjugate are modeled by a beamspliter with transmission η_{b2}. This includes the less-than-perfect quantum efficiency of the detector photodiode and the finite separation of the conjugate optical noise power from the detector electronic noise floor.

The AC and DC components of the intensities of the two modes a_f and b_f are recorded separately. We post-process the AC time traces by filtering them between 0.5 MHz to 2.5 MHz (3 dB points) using a 4th-order Butterworth band-pass filter with a slope of 80 dB/decade on both the low and high pass edges. The resulting time traces are used to determine the intensity correlation coefficient and the intensity-difference squeezing between the two beams by employing Eqs. (4.10) and (4.11) derived in the following section.

4.4 Model

We use a simple quantum-mechanical model to simulate the experiment. We label the optical field operators for the modes shown in Fig. 4.2(a) as $\hat{a}_{0,i,f}$, $\hat{b}_{0,i,f}$, and $\hat{u}_{a1,a2,b1,b2}$. Since there is no PSA between the two beamsplitters in the conjugate path, we can combine the two beamsplitters into one with transmission $\eta_b = \eta_{b1} \cdot \eta_{b2}$ and operator $\hat{u}_b$ associated with the vacuum field coupling into it. We treat all pump

beams classically. The vectors $\hat{\vec{V}}_0$ and $\hat{\vec{V}}_f$ are the input and output field operators defined by

$$\hat{\vec{V}}_0 = \begin{pmatrix} \hat{a}_0 \\ \hat{a}_0^\dagger \\ \hat{b}_0 \\ \hat{b}_0^\dagger \end{pmatrix} \quad \text{and} \quad \hat{\vec{V}}_f = \begin{pmatrix} \hat{a}_f \\ \hat{a}_f^\dagger \\ \hat{b}_f \\ \hat{b}_f^\dagger \end{pmatrix}. \tag{4.2}$$

The source and PSA can then be described by the matrices

$$\boldsymbol{F_1} = \begin{pmatrix} \cosh r & 0 & 0 & \sinh r \\ 0 & \cosh r & \sinh r & 0 \\ 0 & \sinh r & \cosh r & 0 \\ \sinh r & 0 & 0 & \cosh r \end{pmatrix} \tag{4.3}$$

and

$$\boldsymbol{F_2} = \begin{pmatrix} \cosh s & e^{i\phi_{\mathrm{PSA}}} \sinh s & 0 & 0 \\ e^{-i\phi_{\mathrm{PSA}}} \sinh s & \cosh s & 0 & 0 \\ 0 & 0 & 1 & 0 \\ 0 & 0 & 0 & 1 \end{pmatrix}, \tag{4.4}$$

respectively. Here, r and s are the squeezing parameters which are related to the gains of the source and PSA via $G_{\mathrm{source}} = \cosh^2 r$ and $G_{\mathrm{PSA}} = e^{2s}$. ϕ_{PSA} is the phase of the PSA defined in Eq. (4.1). We keep $\phi_{\mathrm{PSA}} = 0$ such that the intensity gain of the probe beam is always G_{PSA}.

The experiment can then be described by the transformation of field operators

$$\hat{\vec{V}}_f = \boldsymbol{T_2}\left(\boldsymbol{F_2}\left[\boldsymbol{T_1}(\boldsymbol{F_1}\hat{\vec{V}}_0) + \hat{\vec{L}}_1\right]\right) + \hat{\vec{L}}_2, \tag{4.5}$$

where the matrices $\boldsymbol{T_1}$ and $\boldsymbol{T_2}$ describe the transmission of the beamsplitters, and vectors $\hat{\vec{L}}_1$ and $\hat{\vec{L}}_2$ contain the field operators for the vacuum modes coupled in by optical losses:

$$\boldsymbol{T_1} = \begin{pmatrix} \sqrt{\eta_{a1}} & 0 & 0 & 0 \\ 0 & \sqrt{\eta_{a1}} & 0 & 0 \\ 0 & 0 & \sqrt{\eta_b} & 0 \\ 0 & 0 & 0 & \sqrt{\eta_b} \end{pmatrix}, \tag{4.6}$$

$$\boldsymbol{T_2} = \begin{pmatrix} \sqrt{\eta_{a2}} & 0 & 0 & 0 \\ 0 & \sqrt{\eta_{a2}} & 0 & 0 \\ 0 & 0 & 1 & 0 \\ 0 & 0 & 0 & 1 \end{pmatrix}, \tag{4.7}$$

$$\hat{\vec{L}}_1 = \begin{pmatrix} i\sqrt{1-\eta_{a1}}\,\hat{u}_{a1} \\ -i\sqrt{1-\eta_{a1}}\,\hat{u}_{a1}^\dagger \\ i\sqrt{1-\eta_b}\,\hat{u}_b \\ -i\sqrt{1-\eta_b}\,\hat{u}_b^\dagger \end{pmatrix}, \tag{4.8}$$

$$\vec{\hat{L}}_2 = \begin{pmatrix} i\sqrt{1-\eta_{a2}}\,\hat{u}_{a2} \\ -i\sqrt{1-\eta_{a2}}\,\hat{u}_{a2}^\dagger \\ 0 \\ 0 \end{pmatrix}. \tag{4.9}$$

From Eq. (4.5), we can derive the field operators $\hat{a}_f$ and $\hat{b}_f$ and the number operators $\hat{n}_a = \hat{a}_f^\dagger \hat{a}_f$ and $\hat{n}_b = \hat{b}_f^\dagger \hat{b}_f$ for the output modes. $\hat{n}_a$ and $\hat{n}_b$ allow us to calculate the expectation values of quantities such as the intensity correlation coefficient and the intensity-difference squeezing.

The intensity correlation coefficient is calculated from

$$M_{\text{XC}} = \frac{\langle (\hat{n}_a - \langle \hat{n}_a \rangle)(\hat{n}_b - \langle \hat{n}_b \rangle) \rangle}{\sqrt{\Delta^2 \hat{n}_a}\sqrt{\Delta^2 \hat{n}_b}}, \tag{4.10}$$

where $\Delta^2 \hat{n}_a$ and $\Delta^2 \hat{n}_b$ are the variances of the intensities. Since we are only looking at AC components of the signal, $\langle \hat{n}_a \rangle = \langle \hat{n}_b \rangle = 0$.

The intensity-difference squeezing is calculated from

$$M_{\text{SQ}} = -10 \log_{10}\left[\frac{\Delta^2(\hat{n}_a - \hat{n}_b)}{\Delta^2 \hat{n}_{\text{SN}}} \right], \tag{4.11}$$

where $\Delta^2 \hat{n}_{\text{SN}}$ is the shot noise, which is defined as the variance of the intensity difference of two coherent beams having the same intensities as the measured probe and conjugate beams.

Figures 4.3 and 4.4 are theoretical plots calculated from Eqs. (4.10) and (4.11),

respectively for PSA gain of 1, 2, 4 and 100. For simplicity, we assume $\eta_{a1} = \eta_{b1} = \eta_{b2} = 1$ and $G_{PIA} = 3.0$ for both graphs. Note that, in Fig. 4.4 the shot noise is determined by two coherent beams that have the same intensities as the modes a_i and b_i. Since the optical gain of the PSA alters the optical power of the probe, in order to have a consistent power measurement with the mode a_i, for each transmission η_{a2}, we introduce a detector gain, G_d, so that $G_{PSA} \times \eta_{a2} \times G_d = 1$ to compensate for the optical gain of the PSA.

These two graphs clearly indicate that the measurements of both the intensity correlation coefficient and the intensity-difference squeezing are improved when the PSA is present, and greater improvement is achieved with greater PSA gains. One noteworthy fact is that, when the gain of the PSA is sufficiently large (e.g., $G_{PSA} = 100$), these two graphs would basically be two nearly horizontal lines at the intensity correlation coefficient and the intensity-difference squeezing that would be measured by perfect detectors.
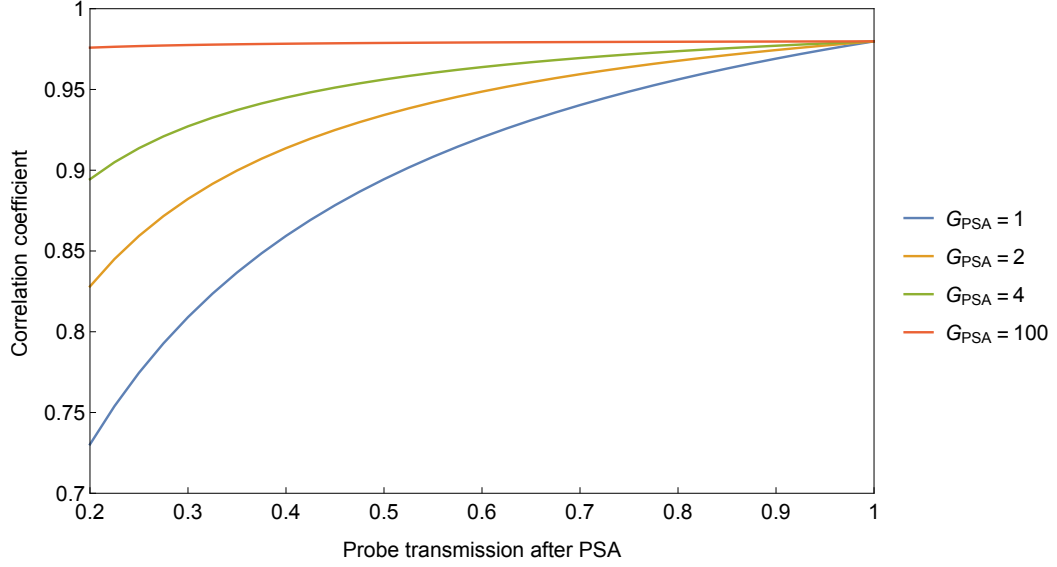
Figure 4.3: Theoretical plots of intensity correlation coefficient as a function of probe transmission η_{a2} after the PSA for different PSA gains, calculated from Eq. (4.10). Other parameters are $\eta_{a1} = \eta_{b1} = \eta_{b2} = 1$ and $G_{\mathrm{PIA}} = 3.0$.
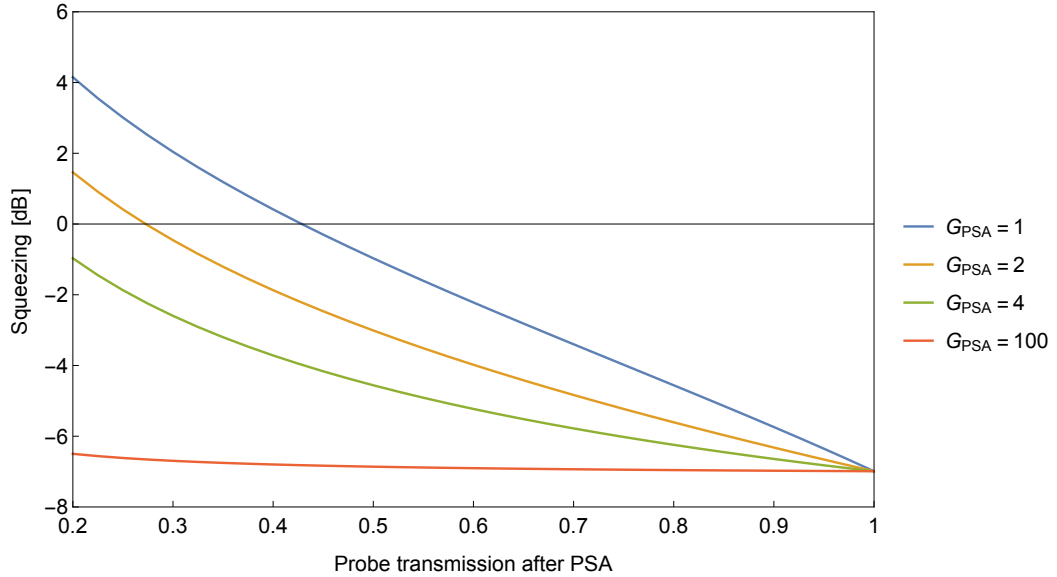
Figure 4.4: Theoretical plots of intensity-difference squeezing as a function of probe transmission η_{a2} after the PSA for different PSA gains, calculated from Eq. (4.11) with detector gain G_d adjustments, so that $G_{\mathrm{PSA}} \times \eta_{a2} \times G_d = 1$ to compensate for the optical gain of the PSA. Other parameters are $\eta_{a1} = \eta_{b1} = \eta_{b2} = 1$ and $G_{\mathrm{PIA}} = 3.0$.

To compare the predictions of this model to measurements requires values of

the various gain and loss parameters. The Appendix A describes how to extract source parameters from auxiliary measurements of beam intensities. The PSA gain and the inserted losses are measured directly. No other fitting parameters are required to generate the theoretical curves shown in the following section.

4.5   Experimental results

We demonstrate, in this section, the experimental results obtained by using the PSA to compensate for the downstream losses including less-than-perfect detection efficiency. We show that, with the presence of the PSA, the measurements of the intensity correlation coefficient and the intensity-difference squeezing are substantially improved even when there is tremendous amount of loss. We also discuss using the PSA to compensate for the downstream losses in the case of two-mode vacuum squeezing in Section 4.5.3.

4.5.1   Intensity correlation coefficient

In Fig. 4.5, we plot the measured intensity correlation coefficient of the probe and conjugate beams as a function of the probe transmission η_{a2} after the PSA. To operate the PSA at different gains, we adjust the one photon detuning Δ (see Fig. 4.2(c)). Since the two 4WM processes share a pump beam, changing the one photon detuning Δ changes the gain of the source, G_{source}, as well. In order to have a consistent preparation of the two-mode squeezed state, we adjust the pump power going to the source so that the intensity-difference squeezing produced by
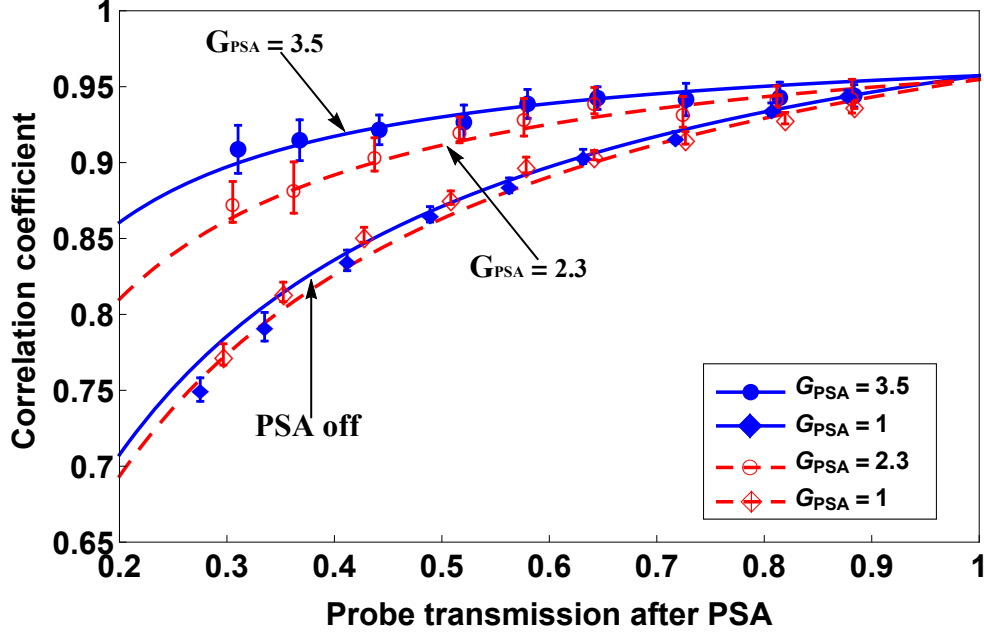
Figure 4.5: Intensity correlation coefficient of the probe and conjugate beams as a function of probe transmission η_{a2}. Blue points and lines are for the source gain $G_{\mathrm{source}} = 3.3$. Red points and dashed lines are for the source gain $G_{\mathrm{source}} = 3.0$. The diamonds (both open and solid) are for the PSA cell removed from the probe path (i.e., $G_{\mathrm{PSA}} = 1$). The circles are for the PSA present with a gain of 2.3 (open circles) and 3.5 (solid circles), respectively. The solid and dashed lines are theoretical predictions calculated from Eqs. (4.5) and (4.10) using the source parameters given in the Appendix A.

the source stays at -5.8 dB. Specifically, for the measurements shown in Fig. 4.5 we

choose $\Delta = 1.4$ GHz and 1.3 GHz to produce a PSA gain of 2.3 and 3.5, respectively.

As we change the detuning, the losses in the source also change, requiring a different

source gain ($G_{\mathrm{source}} = 3.0$ and 3.3, respectively) to maintain the squeezing level (see

Appendix A).

Figure 4.5 shows that adding a PSA increases the measured intensity corre-

lation coefficient. The blue (red) circles show data taken with $G_{\mathrm{PSA}} = 3.5$ (2.3),

and the diamonds show data taken when the PSA is removed (i.e. $G_{\mathrm{PSA}} = 1$).

G_source for each set of data is given in the figure caption. The vertical error bars on the data points are one sample standard deviation statistical uncertainties from 60 time traces. Data sets sharing the same Δ but with the PSA on and off do not share the same transmission values owing to the variation in the optical noise power separations from the detector electronic noise floor [105]. The highest value of the transmission after the PSA is 0.88 (the rightmost open red diamond), which is determined by the optical transmission of 0.99, the detector photodiode quantum efficiency of 0.90, and the loss of 1.6 % associated with a noise power separation of 18 dB from the detector electronic noise floor. Extrapolating to zero loss, the intensity correlation coefficients are 0.955 and 0.957 for $G_\text{source} = 3.0$ and 3.3, respectively. For an ideal source with no losses, the correlation coefficient is related to the squeezing parameter r by $M_\text{XC} = \tanh 2r$. In the limit of large r (high G_source), M_XC approaches one. Figure 4.5 clearly shows that the intensity correlation coefficient is improved when the PSA is present, and greater improvement is achieved with higher G_PSA, e.g., the data points with $G_\text{PSA} = 3.5$ are closer to the correlation coefficient that would be measured with an ideal detector than the ones with $G_\text{PSA} = 2.3$.

4.5.2 Intensity-difference squeezing

In Fig. 4.6 we plot the measured intensity-difference squeezing versus the probe transmission η_a2 after the PSA. The shot noise is measured from the time traces of two coherent beams that have the same intensities as the modes a_f and b_f for each transmission. The squeezing is obtained from the time traces of the measured probe

and conjugate intensities according to Eq. (4.11). In Fig. 4.6, when the PSA is absent ($G_{\mathrm{PSA}} = 1$), we measure a best intensity-difference squeezing of -5.8 dB. As we lower the transmission, we gradually lose the squeezing as expected; at the lowest two transmissions, we lose the squeezing completely. For high transmission values, turning on the PSA destroys the squeezing. When the PSA is on, the probe beam power is amplified by the PSA, which causes a power imbalance between the probe and conjugate beams. Unlike the correlation coefficient, squeezing is affected by changing the relative probe and conjugate powers. As the probe transmission decreases, the power of the probe mode a_f approaches that of the conjugate mode b_f, and squeezing is partially restored.
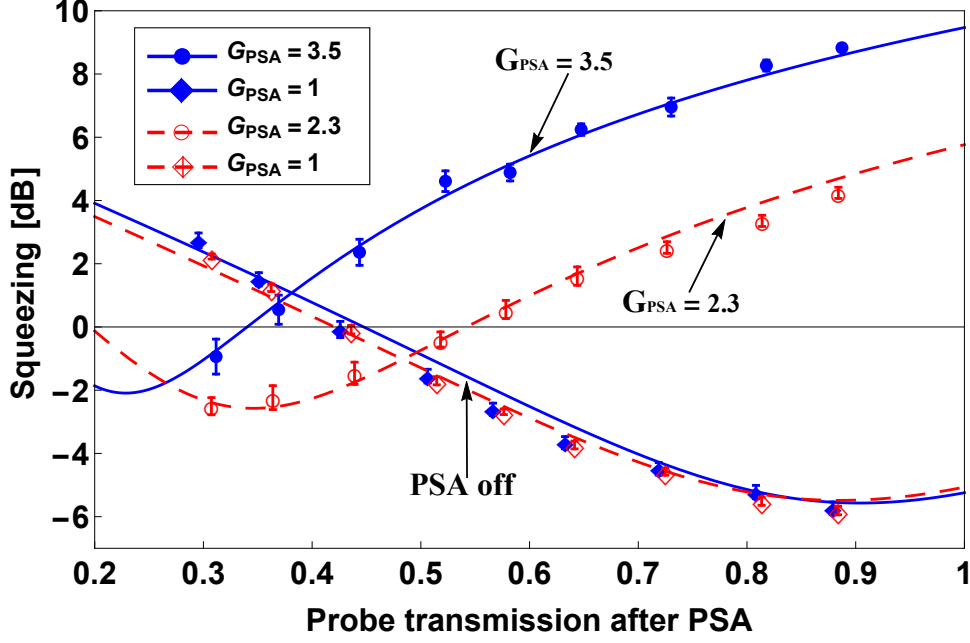
Figure 4.6: Intensity-difference squeezing measured from the time traces of the intensities of modes a_f and b_f, as a function of probe transmission η_{a2}. Blue points and lines are for the source gain $G_{source} = 3.3$. Red points and dashed lines are for the source gain $G_{source} = 3.0$. The diamonds (both open and solid) are for the PSA cell removed from the probe path (i.e., $G_{PSA} = 1$). The circles are for the PSA present with a gain of 2.3 (open circles) and 3.5 (solid circles), respectively. The solid and dashed lines are theoretical predictions calculated from Eqs. (4.5) and (4.11) using the source parameters given in the Appendix A.

The power imbalance between probe and conjugate caused by the PSA can be compensated by adjusting the gain G_{Da} of the probe detector. In particular, by adjusting G_{Da} so that $G_{PSA} \times \eta_{a2} \times G_{Da} = 1$, the probe power is the same as would be measured by an ideal detector in mode a_i. Similarly, we adjust G_{Db} so that $\eta_{b2} \times G_{Db} = 1$. Since we do not vary η_{b2}, G_{Db} is a constant. By performing this gain adjustment, the shot noise is determined by the intensity-difference noise of two shot-noise-limited coherent beams that have the same intensities as the two modes a_i and b_i measured by two ideal detectors, regardless of G_{PSA} or η_{a2}.

By applying the appropriate value of G_{Da} to the measured time traces at each value of η_{a2} and G_{PSA} in Fig. 4.6, we obtain the points in Fig 4.7. With this gain adjustment, points which previously did not show squeezing now do. The larger the G_{PSA} is, the better the improvement in the measured intensity-difference squeezing. For example, without the PSA the squeezing vanishes at approximately 60 % loss, while when $G_{\mathrm{PSA}} = 3.5$, all of the measured points show squeezing and the theory shows that squeezing of -1 dB would still be measured down to even 80 % loss.

The squeezing levels in Figs. 4.6 and 4.7 become positive at small transmission. This is related to the asymmetric treatment of the two modes in the experiment. Both beams have thermal statistics coming from the source. The additional attenuation is present only in one beam and slowly changes this beam's statistics to that of a vacuum coherent state at large attenuation. Thus, even with the detector gain adjustment, the probe beam statistics are different from those of the conjugate beam, which remains a thermal beam, and this gives rise to the anti-squeezing in the intensity-difference.
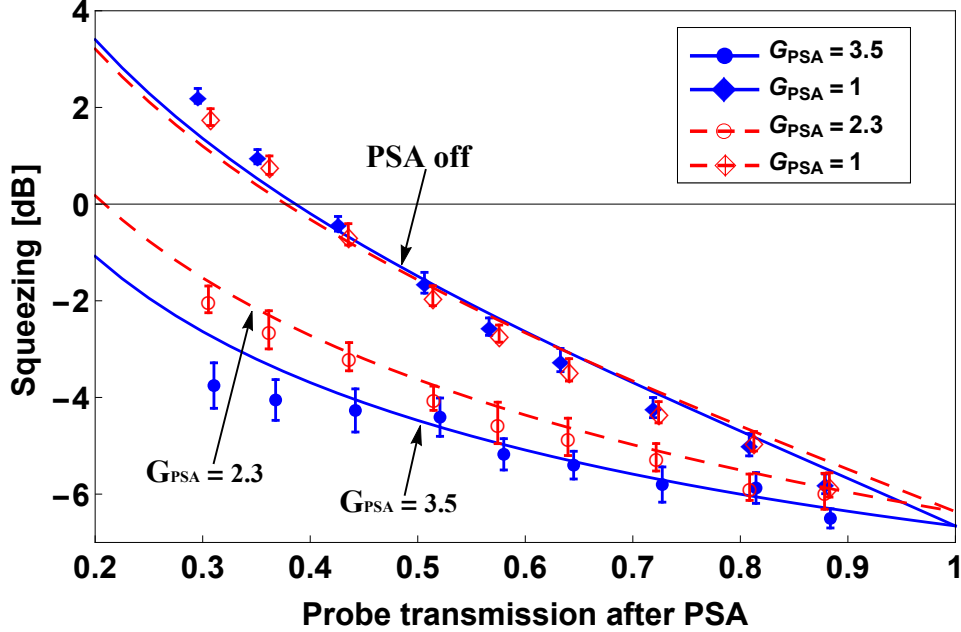
Figure 4.7: Intensity-difference squeezing measured with the detector gain adjustments described in the text. Blue points and lines are for the source gain $G_{\text{source}} = 3.3$. Red points and dashed lines are for the source gain $G_{\text{source}} = 3.0$. The diamonds (both open and solid) are for the PSA cell removed from the probe path (i.e., $G_{\text{PSA}} = 1$). The circles are for the PSA present with a gain of 2.3 (open circles) and 3.5 (solid circles), respectively. The solid and dashed lines are theoretical predictions calculated from Eqs. (4.5) and (4.11) using the source parameters given in the Appendix A.

4.5.3 Two-mode vacuum squeezing

Let us now consider using the PSA to compensate for the downstream losses including less-than-perfect detection efficiency in the two-mode vacuum squeezing configuration. In this experimental arrangement, both of the modes a_0 and b_0 in Fig. 4.2(a) are seeded with the vacuum. The output modes a_i and b_i produced by the PIA make up a two-mode squeezed vacuum state and joint homodyne measurements can be used to measure the noise reduction in the amplitude-difference or

phase-sum quadratures of the light state, as described in Section 2.3.2. Therefore, in Fig. 4.2(a), we replace the two intensity detectors with two balanced homodyne detectors (BHDs) (see Fig. 2.3 in Section 2.3 of Chapter 2) to measure the amplitude quadratures $X_a = (a_f + a_f^\dagger)/2$ and $X_b = (b_f + b_f^\dagger)/2$ of the modes a_f and b_f, respectively. The variance ΔX_-^2 of the joint amplitude-difference quadrature $X_- = X_a - X_b$ is then measured by a spectrum analyzer taking in the electronically subtracted photocurrents from the two BHDs.

The homodyne detection is a common technique for characterizing continuous-variable quantum states. It allows one to observe an arbitrary quadrature. The inclusion of a PSA to overcome the non-unity quantum effeciency of a BHD can then be essentially regarded as a "perfect homodyne detector."

In the experiment, we lock the local oscillator (LO) phase of the probe BHD such that we always detect the quadrature of the probe field that is most amplified by the PSA. We then lock the LO phase of the conjugate BHD relative to the LO phase of the probe BHD such that the spectrum analyzer always measures the joint amplitude-difference quadrature between the probe and conjugate fields.

It is also important to note that each two-mode vacuum squeezing level is found by referencing the measured joint amplitude-quadrature noise level to that found when the probe and conjugate fields output from the PIA cell are blocked. That is, the conjugate BHD will measure the vacuum field shot noise, while the probe BHD will measure the thermal noise resulting from a vacuum state being amplified by the PSA. These are then combined and sent to the spectrum analyzer giving the reference noise level.

In addition to the losses aforementioned in the intensity measurement, for BHD measurement one has to take into account the loss from the less-than-perfect visibility, which we measure to be 92 % and 96 % for the probe and conjugate detectors respectively, and the phase noise of the BHD [106] as well. The phase noise can be estimated according to $N_{\min}^{\mathrm{measured}} = N_{\min} \cos^2 \theta_{\mathrm{rms}} + N_{\max} \sin^2 \theta_{\mathrm{rms}}$, where $N_{\min}^{\mathrm{measured}}$ is the measured joint noise minimum, $N_{\min}$ and $N_{\max}$ are the theoretical noise powers found by calculating ΔX_-^2 and ΔX_+^2, respectively. The phase noise θ_{rms} then becomes a free parameter in the model, which we estimate at a reasonable level of 0.26 radians[3]. Other measured experimental conditions in the two-mode vacuum squeezing configuration are $\eta_{\mathrm{a}1} = 0.74$, $\eta_{\mathrm{b}1} = 0.94$[4], $\eta_{\mathrm{b}2} = 0.90$ and $G_{\mathrm{PIA}} = 4$.

Note that the experimental conditions are very different from those in the bright twin-beam case, as discussed in the previous sections of this chapter. This two-mode vacuum squeezing experiment was performed earlier and the squeezing was not as good as the intensity-difference squeezing. After locking the phases of the LOs to measure the desired joint amplitude-difference quadrature, the best achievable vacuum squeezing is only -1.5 dB in this experiment.

The measured results are shown in Figs. 4.8 to 4.10 for three different gains of the PSA. To obtain different PSA gains, we simply change the PSA cell temperature to have different atomic densities. As expected, the squeezing degrades as the loss in the probe beam is increased. However, when the PSA preamplies the probe field before this loss, we expect higher levels of squeezing even for high loss. Depending

---

[3]The phase noise of this much corresponds to roughly 4 % of the wavelength, which is a reasonable number for the vibration of optics.

[4]The measurement of $\eta_{\mathrm{a}1}$ is much less than $\eta_{\mathrm{b}1}$ is due to the fact that the probe mode is much closer to the atomic resonance than the conjugate mode.

on the amount of loss and the gain of the PSA, some level of the quantum correlations are restored, leading to an expected noise reduction even when there is no squeezing present with the PSA off. At η_{a2} approaching 1, we find that the PSA will actually increase the joint noise level, degrading the squeezing level, as shown by the simulations. This is due to an imbalance in the noise powers of the probe and conjugate beams after the probe has been amplified by the PSA. In principle, this imbalance can be corrected by post-processing the time traces measured by the two BHDs to normalize the results by applying a detector gain to account for the added noise power. However, since the measurements are taken with a spectrum analyzer, no time traces are recorded, this normalization is not carried out in this experiment.
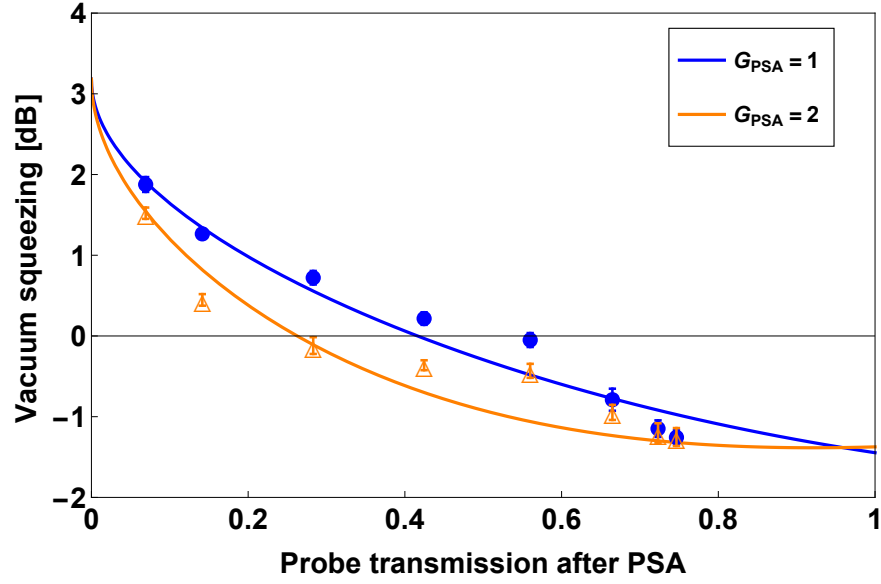
Figure 4.8: Two-mode vacuum squeezing measured from spectrum analyzer as a function of probe transmission η_{a2} after the PSA. The solid blue dots are for the PSA cell removed from the probe path (i.e., $G_{PSA} = 1$). The open orange triangles are for the PSA present with a gain of 2. The solid blue and orange lines are theoretical predictions for $G_{PSA} = 1$ and 2, respectively. Other parameters are $\eta_{a1} = 0.74$, $\eta_{b1} = 0.94$, $\eta_{b2} = 0.90$ and $G_{PIA} = 4$.
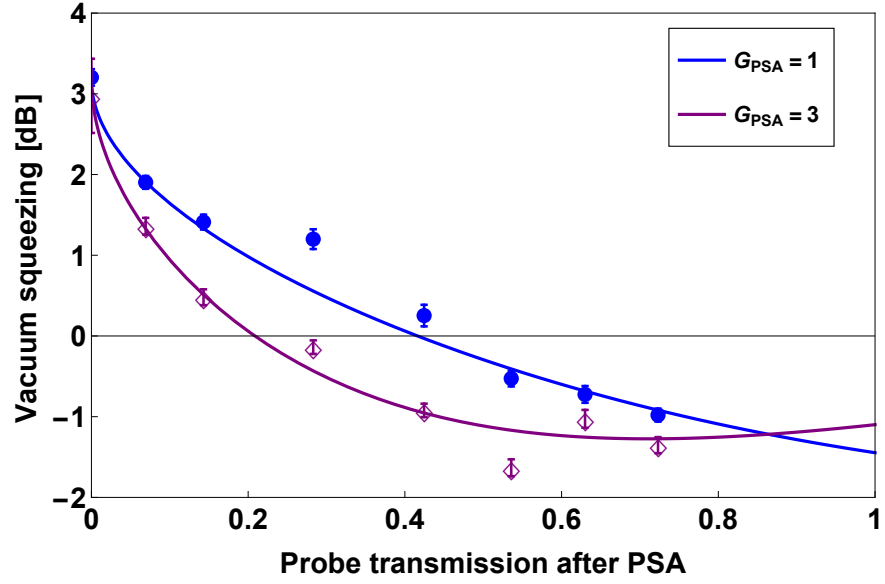
Figure 4.9: Two-mode vacuum squeezing measured from spectrum analyzer as a function of probe transmission η_{a2} after the PSA. The solid blue dots are for the PSA cell removed from the probe path (i.e., $G_{PSA} = 1$). The open purple diamonds are for the PSA present with a gain of 3. The solid blue and purple lines are theoretical predictions for $G_{PSA} = 1$ and 3, respectively. Other parameters are $\eta_{a1} = 0.74$, $\eta_{b1} = 0.94$, $\eta_{b2} = 0.90$ and $G_{PIA} = 4$.
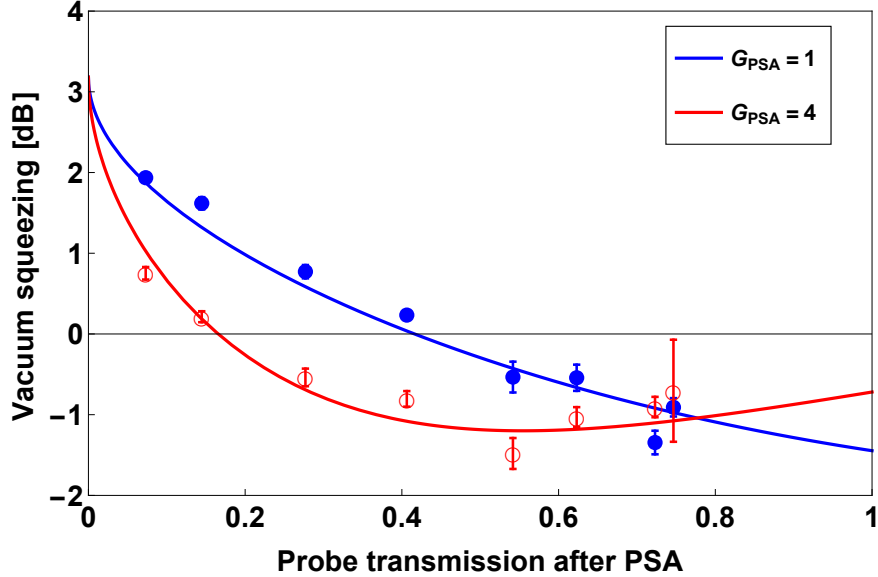
Figure 4.10: Two-mode vacuum squeezing measured from spectrum analyzer as a function of probe transmission η_{a2} after the PSA. The solid blue dots are for the PSA cell removed from the probe path (i.e., $G_{PSA} = 1$). The open red circles are for the PSA present with a gain of 4. The solid blue and red lines are theoretical predictions for $G_{PSA} = 1$ and 4, respectively. Other parameters are $\eta_{a1} = 0.74$, $\eta_{b1} = 0.94$, $\eta_{b2} = 0.90$ and $G_{PIA} = 4$.

4.6   Conclusions

We experimentally demonstrate the use of an optical PSA to reduce the effect of non-unity quantum efficiency of an intensity detector — an important limitation in making continuous variable measurements of quantum states. Use of the PSA allows us to more accurately measure the intensity cross-correlation and intensity-difference squeezing of a two-mode squeezed state. For large PSA gain, the system of a PSA followed by a detector with imperfect quantum efficiency approaches a "perfect detector [94]." We compare experimental measurements taken with various PSA gains and levels of intentionally introduced loss to a simple quantum-mechanical

model and find reasonable agreement.

We also show, in a proof-of-principal experiment, that by including an optical PSA before the downstream loss in a homodyne detection, one is able to make up a "perfect homodyne detector." We demonstrate the use of an optical PSA to restore the squeezing level measured in a two-mode squeezed vacuum state. We find a decent recovery of the measured vacuum squeezing in the presence of substantial loss by including a PSA before the loss.

The type of PSA used here is capable of operating on multiple spatial modes [104], and thus may be useful for overcoming detector efficiency limitations in quantum imaging applications.

Chapter 5:   Mutual information of a two-mode squeezed state propagating through a phase-sensitive optical amplifier

5.1   Introduction

Over the past decade, there has been great interest in tailoring the dispersive properties of optical media with the goal of controlling the speed of pulses of light. Several techniques for dispersion tailoring use optical fields to induce matter-field resonances, which can be designed to exhibit either large normal or anomalous dispersion near the resonances, leading to "slow" or "fast" light pulse propagation, respectively [107]. Potential applications of such optical media include classical and quantum networks [108].

In this chapter, we present experiments that study the effects of the fast and slow light on the propagation of information through an optical medium. We use a phase-insensitve amplifier (PIA) and a phase-sensitive amplifier (PSA) as the dispersive optical media to investigate the timing as well as the transfer fidelity of the information. Before we dive into the details of the experiments, let us first introduce some basic concepts, such as the group velocity and the information velocity, etc.

5.1.1 Group velocity

For the case when the real part of the refractive index $n(\omega)$ varies slowly over the spectral width of the pulse, it is customary to expand the field wave vector in a Taylor series centered on the pulse carrier frequency ω_0. Such an analysis leads to the concept of the group velocity

$$v_g = \frac{c}{(n + \omega \frac{\partial n}{\partial \omega})|_{\omega=\omega_0}} = \frac{c}{n_g},\tag{5.1}$$

where n_g is the frequency-dependent group index [109].

We refer to the quantity $\partial n/\partial \omega$ as the dispersion of an optical material. For typical optical materials, there exist narrow spectral regions where $n(\omega)$ is a decreasing function of frequency (that is, $\partial n/\partial \omega < 0$), resulting in a condition known as anomalous dispersion [110]. When ω_0 is within such a region, n_g can be less than one and can even become negative when the anomalous dispersion is large. This results in "fast light", for which it is possible that the peak of a light pulse may exit the optical material before it passes through the entrance face [111]. The amount of fast-light pulse advancement is largest when v_g is negative and near zero (n_g large and negative).

5.1.2 Information velocity and relativistic causality

In the early 1900s, the possibility of superluminal group velocities ($v_g > c$ or $v_g < 0$) was a great concern to researchers until the work of Sommerfeld and

Brillouin [112]. They used asymptotic analysis[1] to study a step-modulated pulse propagating through a resonant absorber. Sommerfeld found that the front of the pulse (the moment when the field first becomes nonzero) propagates precisely at c, consistent with the special theory of relativity. They noted that the "front velocity," the velocity at which an infinitely sharp step-function-like disturbance of the light intensity propagates, should be used as the velocity of signal transmission, not the group velocity v_g of the light pulse [112, 114].

Brillouin extended Sommerfeld's analysis and found that the pulse breaks up after the front, consisting of two small wave packets (now called precursors — the transient behavior of the propagated field resulting from a discontinuity in the waveform or one of its derivatives) followed by a large wave packet (the "main signal"). The first (second) small packet is known as the Sommerfeld (Brillouin) precursor, which arises from the spectral components of the incident pulse above (below) the resonance and is predicted to have maximum intensity of 10^{-7} (10^{-4}) of the eventual main signal intensity. Brillouin believed that the arrival of the signal should be associated with the arrival of the large-amplitude wave packet because of the smallness of the precursors[2], although Sommerfeld stressed that an extremely sensitive detector should be able to register the front of the pulse and hence measure a propagation speed of c for the signal.

---

[1] For the modern asymptotic theory, see Ref. [113].

[2] Several researchers have identified mistakes in this early work, as reviewed by Oughstun and Sherman [113]. Most notable is the prediction that the precursors are much larger than previously thought; their amplitude can be similar to or larger than the amplitude of the main signal. In fact, Jeong *et al.* [115] demonstrated that precursors can be readily observed using standard experimental apparatus in setups similar to that used in fast-light research. They found that both the Sommerfeld and Brillouin precursors as well as the main signal arrive immediately after the pulse front, which propagates at c.

Another outcome of the discussions in the early 1900s, as recounted in the preface and first chapter of the book by Brillouin [112], was a reformulation of the fundamental postulate of the special theory of relativity. This reformulation states that, rather than limiting the speed of an "object", it is the "information velocity" v_i that is limited by c. Unfortunately, there is no agreed-upon definition of the information velocity [116].

5.1.3 Determine the information velocity

Measuring the information velocity v_i requires an understanding of the fundamental mechanism for information encoding and detection. Chiao and collaborators [114, 116] proposed that new information is encoded on an optical pulse by creating a point that is non-analytic (for example, a discontinuity in the pulse amplitude or its derivatives) and that this point always travels at c regardless of the value of the other velocities associated with the pulse. Essentially, they have generalized Sommerfeld's concept of the front velocity to a non-analytic point of the pulse amplitude, where the front of a step-modulated pulse is an example of a point of non-analyticity. They suggest that the point of non-analyticity is the only part of the pulse representing new information because measurements of the early part of the pulse cannot be used to predict anything about the part of the pulse arriving after the point of non-analyticity, and hence v_i equals the speed of a point of non-analyticity. In other words, a smooth analytic signal is entirely determined by its teeny-tiny front, there is no new information being carried by the peak. Therefore,

if the tiniest front of a smooth pulse determines the entire pulse, we must account for the effect that quantum fluctuations at the front might have on the detection of the pulse.

Experimentally, particularly in the inevitable presence of quantum noise, the non-analytic points of the pulse amplitude such as the pulse front may not convey the full story of what is readily observed in the laboratory. It is thus interesting to consider other operational definitions of a signal, or information, that apply to particular systems. For example, Stenner *et al.* [117] studied the propagation of classical information encoded in bright, actively-shaped optical pulses traveling through a fast-light medium. These experiments showed that the operational information velocity is actually slowed to speeds less than c. Although noise may have affected the experimental results, these experiments were not conducted in a regime where quantum noise necessarily played a crucial role. On the other hand, adopting a definition of signal velocity based on observing a given signal-to-noise ratio, Kuzmich *et al.* [68] showed how quantum noise associated with gain-assisted[3] fast light would be expected to limit the early detection of smooth, narrow-band pulses consisting of only a few photons.

5.1.4   Our approach

Throughout this chapter we adopt an alternative definition of a signal by choosing it to be the random, but strongly correlated quantum fluctuations between

---

[3]Gain-assisted fast or slow light utilizes a gain line rather than an absorption resonance of the medium to render a frequency-dependent group index.

two spatially separated modes of a bipartite entangled state. The two-mode entangled state in this experiment is generated via a four-wave mixing (4WM) based phase-insensitive amplifier (PIA), as described in Section 2.3. The fluctuations in the field quadratures of each individual mode are random, but since the fluctuations are quantum-mechanically correlated, there are more-than-classical "similarities" between the correlated probe and conjugate quadratures, and our signal is defined to be the quantification of these "similarities." Although entanglement cannot be used to signal superluminally [118], it is thought to be an essential resource in quantum information science [119, 120]. Accordingly, the prospect of storing [121] or delaying [25] entanglement has attracted significant interest.

The fluctuations of the probe and conjugate modes are not externally imposed and they present no obvious pulse fronts or non-analytic features to point to as defining the signal velocity. As such, most classically rooted approaches to defining the signal or information content of the individual modes are not readily applicable to this system. Despite the randomness of these fluctuations, information is shared between the modes. We take the "mutual information[4]" between the probe and conjugate modes as our information measure. This removes the ambiguity of defining the arrival time of information about a pulse front arrival time in the presence of noise, quantum or otherwise as well as the finite bandwidth.

---

[4]Two suitable definitions of the mutual information will be given in Section 5.2 and Section 5.4.2.1 below.
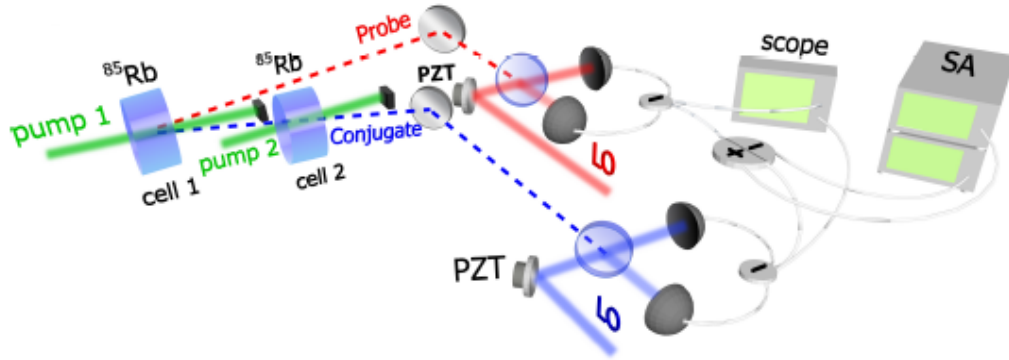
Figure 5.1: Experimental setup of using a second PIA cell as the dispersive medium. The first PIA cell produces a two-mode entangled state. A region of anomalous dispersion for the conjugate is created in a second PIA cell driven by pump 2, whose frequency is independently tunable with respect to pump 1. The quantum mutual information shared by the two modes are characterized by two balanced homodyne detectors followed by two spectrum analyzers (SAs) and an oscilloscope (scope).

5.2   Phase-insensitive optical amplifier as the dispersive medium[5]

We have studied how the dispersion associated with phase-insensitive gain [122] affects the propagation of the quantum mutual information shared by the probe and conjugate fields [29]. This was done by inserting a second PIA cell as the dispersive medium into the path of the conjugate field and driving this 4WM process with a separate pump (see Fig. 5.1).

The quantum mutual information for bipartite Gaussian states[6] is readily accessible via optical homodyne measurements [119, 120] and naturally provides a consistent description of information in the system. We use balanced homodyne detection (BHD) to characterize the quantum mutual information contained in the

---

[5]This section is mainly based on the paper "Quantum mutual information of an entangled state propagating through a fast-light medium," *Nat. Photonics* **8**, 515 (2014).

[6]In this chapter, we restrict ourselves to the Gaussian states.

two-mode entangled state. Specifically, for a general two-mode state this quantity is defined in terms of the von Neumann entropy $S_V(\rho) = \text{Tr}(\rho \log \rho)$ [123]:

$$I(\rho) = S_V(\rho_1) + S_V(\rho_2) - S_V(\rho), \tag{5.2}$$

where $I(\rho)$ is the quantum mutual information; ρ denotes the full state density matrix and ρ_i denotes the reduced density matrix of the two individual modes after the partial trace has been evaluated over the other mode. For the case of a continuous-variable Gaussian state, the calculation of the mutual information involves the symplectic eigenvalues of the standard form and partially-transposed covariance matrix [124, 125], which is given by

$$\gamma_{ij} = \frac{1}{2}\langle \hat{R}_i \hat{R}_j + \hat{R}_j \hat{R}_i \rangle - \langle \hat{R}_i \rangle \langle \hat{R}_j \rangle, \tag{5.3}$$

where $\hat{R}_i \equiv (\hat{X}_i, \hat{Y}_i)$ is the generalized field quadrature, and $i \in \{p, c\}$ (p denotes the probe and c the conjugate). In this standard form, the on-diagonal sub-matrices characterize the individual modes' quadrature fluctuations while the off-diagonal sub-matrices capture the covariances between the two modes' quadrature fluctuations. All of the elements of the sub-matrices can be obtained from the two BHD measurements of the two modes.

Then, from the delay-dependent covariance matrix of two-mode entangled state, we can compute the delay-dependent quantum mutual information.

We show, in Fig. 5.2, that when one mode of the two-mode entangled state

106
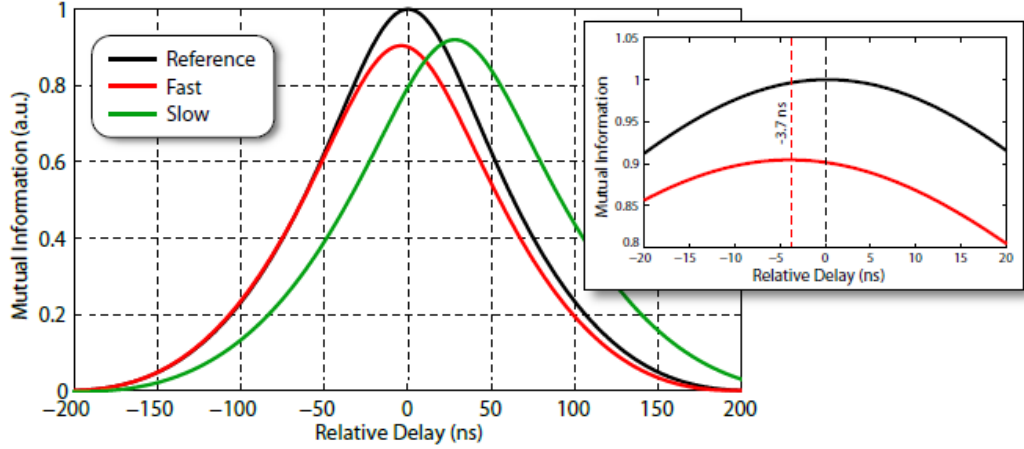
Figure 5.2: Comparison of quantum mutual information between the probe and conjugate as a function of relative delay for fast and slow light. The smooth shape of the curves results from the large amount of data (180 files consisting of 1×10^7 points per file) used to calculate the mutual information. When considering fast-light advancement of the conjugate (red trace), we observe an advance in the peak of the mutual information of 3.7 ± 0.1 ns. The subpanel provides a closer look at the maxima of the mutual information curves for the reference and fast-light cases. There is no statistically significant advance of the leading edge of the mutual information in the case of fast-light propagation. Repeating the same analysis for slow-light propagation of the probe we observe significant delays of both the leading and trailing edges of the mutual information (green trace).

passes through the second PIA cell acting as a fast-light medium, the peak of the quantum mutual information between the modes is advanced, but the arrival of the leading edge is not. We also show that — in contrast — the leading and trailing edges of the mutual information are both delayed when one of the modes propagates through the PIA cell acting as a gain-assisted slow-light medium.

The experiment clearly shows that the mutual information can be delayed. We speculate that the degradation of the mutual information due to added noise

associated with the phase-insensitive gain appears to prevent an advancement of the leading edge.

5.3 Phase-sensitive optical amplifier as the "dispersive" medium — amplitude modulated classical signal as the input

We now consider replacing the second PIA cell with a phase-sensitive amplifier (PSA) as the dispersive medium. As elaborated in Section 2.4, in the case of a PSA, no extra noise will be added for the quadrature with the correct input phase (e.g., at the phases of the maximal amplification and the maximal deamplification). A natural question would then be: *Do PSAs need to keep information velocities $\leq c$ when operating noiselessly[7]?* It is therefore interesting to extend our investigation to explore the advance and delay of the mutual information transmitted through a PSA.

Before we conduct the full experiment which involves a PIA cell followed by a PSA cell, let us first consider a much simpler (and classical) case where the PIA cell is removed and a sinusoidally amplitude-modulated or a pulsed beam of light is directly sent to the PSA cell.

5.3.1 Experimental setup

The experimental details are depicted in Fig. 5.3(a) except that the PIA cell is removed and an 80 MHz acousto-optic modulator (AOM) (the dashed triangle

---

[7]Of course, we hope they do!

in the figure) is inserted in the probe seed beam path to sinusoidally amplitude-modulate or to pulse the input beam of light. The effect of removing the PIA cell is the removal of the conjugate beam. We make our modulation and pulses via the zeroth order of the AOM shifting power away into other AOM orders by modulating the driving rf power. The PSA is created through the 4WM process in ^{85}Rb vapor, as described in Section 2.4. The signal probe beam is detuned from the D$_1$ line (795 nm) of ^{85}Rb while two strong pump beams with frequencies ± 3 GHz from the probe intersect it at a small angle (~ 0.6 degree) within the atomic vapor. Before being aligned into the PSA vapor cell, the amplitude-modulated input beam passes through a single-mode polarization-maintaining fiber. The input probe beam after the fiber is 160 μW with a $1/e^2$ beam waist of 300 μm. The pump beams have a $1/e^2$ beam waist of 500 μm and each has a power of 100 mW. The 12.5 mm vapor cell is filled with isotopically pure ^{85}Rb and heated to 86 °C. All the data shown in the following sections is taken with the probe beam blue detuned between 1.3 GHz and 1.4 GHz from the center of the $5S_{1/2}$ $F = 3$ manifold to the center of the $5P_{1/2}$ Doppler-broadened transition (see Δ in Fig. 5.3(c)). The pump beams are created by seeding two 0.5 W tapered amplifiers (TAs) with light that has been shifted ± 3 GHz using double-passed AOMs. The probe frequency is always centered between the two pumps. The chosen detunings result in a -4 MHz two-photon detuning for the probe and each pump compared to the exact hyperfine splitting of the ground state, in order to compensate for light shifts (see Fig. 5.3(c)).
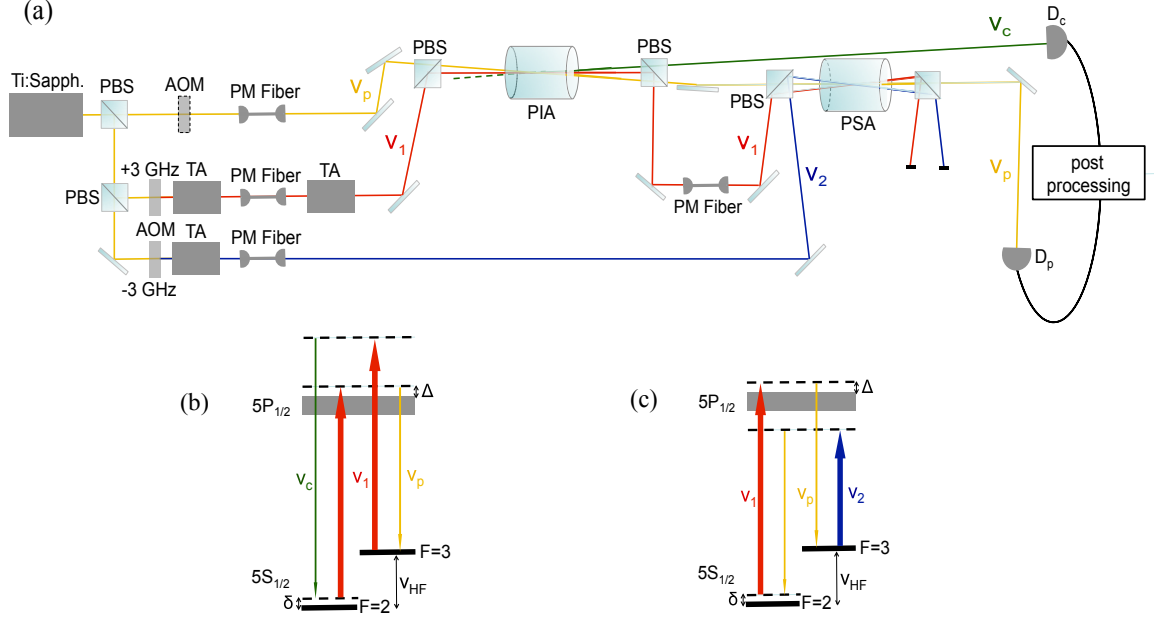
Figure 5.3: Experimental setup and 4WM schemes showing atomic energy levels in ^{85}Rb and laser tunings. (a) Experimental setup. AOM: acousto-optic modulator, TA: semiconductor tapered amplifier, PBS: polarizing beam splitter, PM fiber: polarization-maintaining fiber. The quantum correlated twin beams, probe and conjugate, are generated by the PIA cell. The PSA cell is placed in the probe beam path as the "dispersive" medium. The two intensity detectors D_p and D_c measure the intensity time traces of the probe and conjugate beams, which are post-processed to calculate the mutual information between them. (b) 4WM scheme in the PIA cell. ν_p, ν_c and ν_1 are the optical frequencies of probe, conjugate and pump beams, respectively. (c) 4WM scheme in the PSA cell. ν_1, ν_2 are the optical frequencies of the two pump beams, and ν_p is the optical frequency of the probe beam. For both (b) and (c): the width of the excited state in the level diagram represents the Doppler broadened line, Δ is the one-photon detuning, $\delta = -4$ MHz is the two-photon detuning, and $\nu_{\mathrm{HF}} = 3.036$ GHz is the hyperfine splitting in the electronic ground state of ^{85}Rb.

5.3.2 Experimental results

5.3.2.1 Sinusoidal amplitude modulation

We first use the AOM to sinusoidally amplitude-modulate the input probe beam at 1 MHz with a modulation depth of 0.15. Depending on the input phase, the PSA will amplify or deamplify the input as discussed in Section 2.4. Examples of outputs from inputting this sinusoidally amplitude-modulated probe beam to the PSA are plotted in Fig. 5.4(a). The black curve is the input reference probe beam. The red and blue curves are examples of the amplified (also delayed) and deamplified (also advanced) outputs from the PSA respectively. The green, purple and brown curves are sinusoidal fits to the experimental curves. We can see from these curves that, not only are the amplitudes of the sine waves amplified or deamplified by the PSA, but also the peaks (and valleys) are advanced or delayed with respect to the input reference curve. The phase extracted from individual sinusoidal fit is used to calculate the "delay δt ($\delta t < 0$ means advanced, $\delta t > 0$ means delayed)" according to

$$\delta t = (\frac{\phi - \phi_r}{2\pi})T, \tag{5.4}$$

where ϕ is the phase of the output probe from the PSA, ϕ_r is the phase of the input probe to the PSA and T is the period of the sinusoidal modulation, which is 1 μs.

By calculating the gain, which is defined as the ratio of the output modulation amplitude over the input modulation amplitude, for each output curve, we can get a parametric plot of gain versus δt in Figs. 5.5(a) and 5.5(b). As derived in Section

111

2.4, the PSA gain is a function of the input relative phase among the two pumps and the probe (see Eq. 2.44), for the data in Figs. 5.5(a) and 5.5(b), the pump and probe phases are allowed to drift such that each data point represents a shot of the experiment at a different PSA phase, and therefore a different gain. Data points in Figs. 5.5(a) and 5.5(b) are for the one photon detuning $\Delta = 1.4$ GHz and 1.3 GHz, respectively. The maximal gain in Fig. 5.5(b) is greater than it is in 5.5(a) is therefore simply because the detuning for the data points in Fig. 5.5(b) is closer to the atomic resonance (see Fig. 5.3(c)).

From the plots we can learn that, when the PSA is at its maximal or minimal gain, i.e., the "noiseless" operating conditions, the delays are close to 0; however, at the intermediate gains where the output signal-to-noise ratio is reduced (see the noise figure (NF) curve in Fig. 2.6 in Section 2.4), the outputs can be either advanced or delayed giving rise to nonzero δt's.

5.3.2.2 Gaussian pulsing

We also use the AOM to generate a Gaussian pulse by modulating the zeroth order of the AOM. The full width at half maximal (FWHM) of the Gaussian pulse is 500 ns. The delay δt here is simply $t-t_r$, where t is the time of the peak of the output pulse, and t_r is the peak timing of the input reference pulse. In the same fashion as above for the sinusoidal modulation, we plot examples of amplified (also advanced) and deamplified (also delayed) output pulses along with the input reference pulse in Fig. 5.4(b) and the parametric plots of the gain versus δt in Figs. 5.5(c) and 5.5(d)
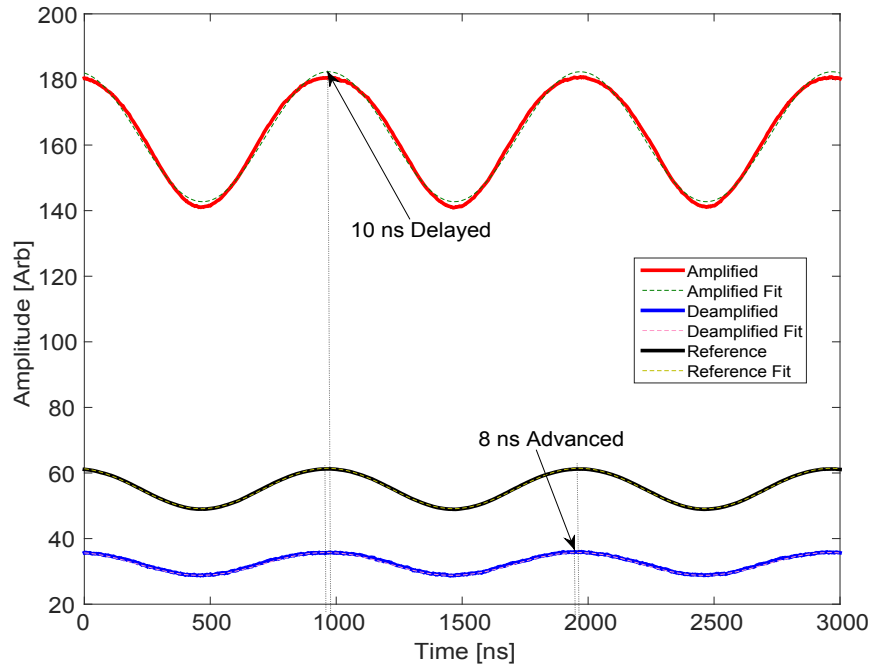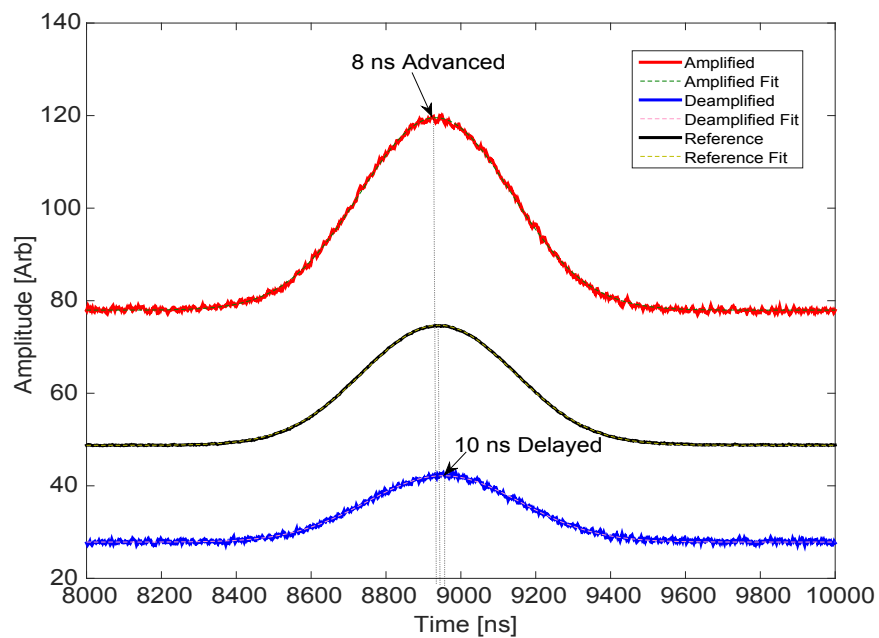
Figure 5.4: Output examples from inputting (a) a sinusoidally amplitude-modulated and (b) a pulsed probe beam to the PSA. The sinusoidal amplitude modulation is at 1 MHz with modulation depth of 0.15. The FWHM of the Gaussian pulse is 500 ns. The black curve is the input reference probe beam. The red and blue curves are the amplified and deamplified outputs from the PSA, respectively. The dashed green, purple and brown curves are (a) sinusoidal and (b) Gaussian fits to the experimental curves, and they are almost completely obscured by the experimental curves.

113

for $\Delta = 1.4$ GHz and 1.3 GHz, respectively. We find the shapes of the plots are similar and the delay and advance are in a qualitative agreement between the cases of sinusoidal amplitude modulation and Gaussian pulsing.

One noteworthy fact is that δt in Fig. 5.5 is not exactly zero when the PSA is at its maximal or minimal gain. As a matter of fact, δt is slightly greater than zero at these two noiseless operation conditions. We attribute this discrepancy to the fact that the reference curve is measured with the beam passing through the cell, but with the pumps blocked. The different optical pumping of the ^{85}Rb atoms under these conditions leads to a phase shift, like a piece of glass, delaying the input by a small amount.

Also note that, in order to completely eliminate the detrimental effect of the phase modulation[8] on the results of the present experiments while using an AOM, we adopt the "AC gain versus DC gain" diagnosis as elaborated in Sections 3.2.1 and 3.4.1. We keep aligning the AOM until the plot of AC gain versus DC gain is a straight line with slope of 1 as shown in Figs. 3.1 and 3.4(a). In this manner, we know that our AOM is producing a (nearly) pure amplitude modulation.

[8]Phase modulation from an AOM has been shown to be an experimental difficulty in some optical PSA experiments [72, 78]. In particular, while the PSA can perform completely noiseless amplification of a particular field quadrature, it can also convert phase modulation to amplitude modulation, making signal-to-noise ratio (SNR) measurements hard to interpret. It can even lead to apparent increases in the SNR after amplification if inadvertent phase modulation is closely tied to an applied amplitude modulation signal, as is the case in using many modulation devices. See Chapter 3 for details.
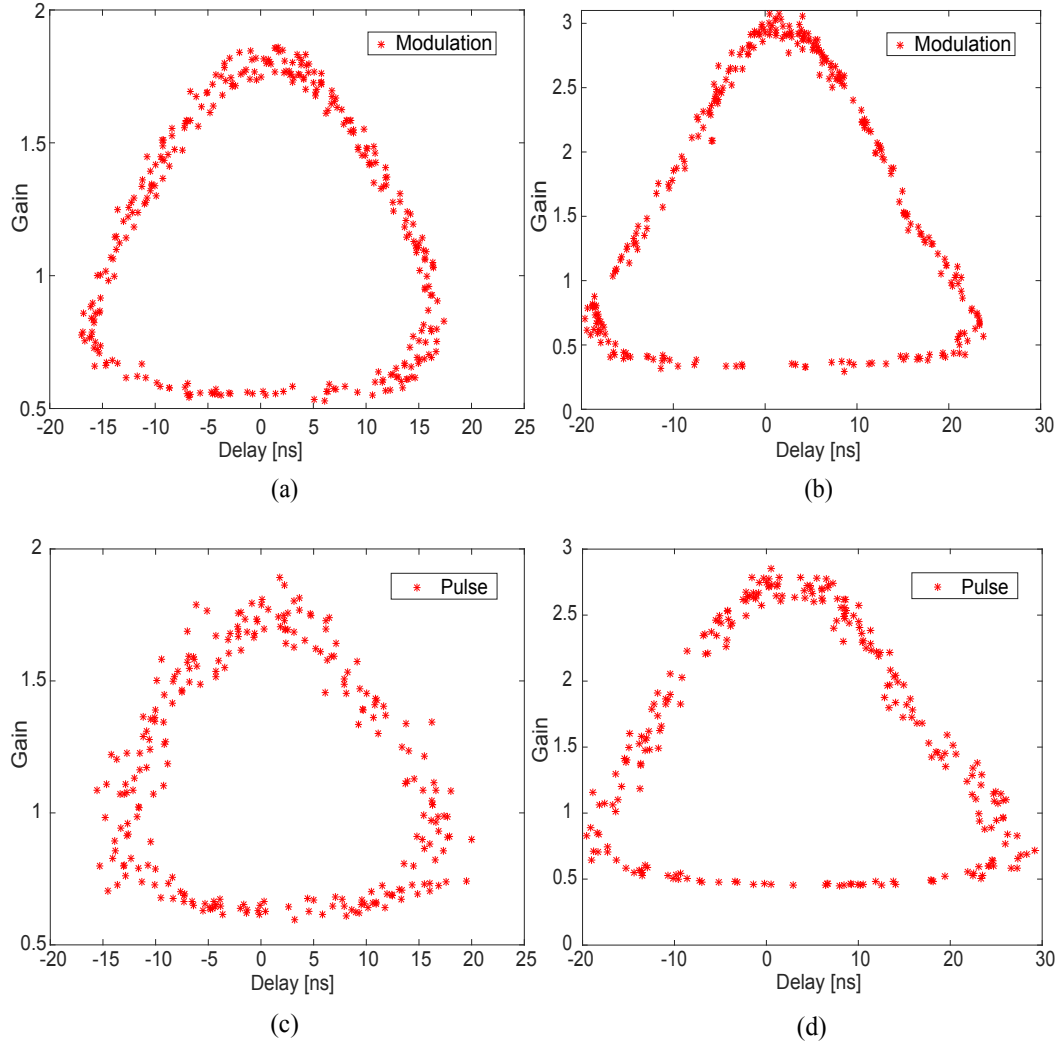
Figure 5.5: Parametric plots of PSA gain versus delay δt for (a) and (b): a sinusoidally amplitude-modulated input beam, and for (c) and (d): a pulsed input beam. Data points in (a) and (c) are for $\Delta = 1.4$ GHz, and data points in (b) and (d) are for $\Delta = 1.3$ GHz. The pump and probe phases are allowed to drift such that each data point represents a shot of the experiment at a different PSA phase, and therefore a different gain (see Eq. 2.44).

5.4 Phase-sensitive optical amplifier as the "dispersive" medium — one mode of a two-mode squeezed state as the input

In the preceding section, we discussed the experiment which involves using amplitude-modulated classical signals as input to a PSA. We found that when the PSA is operating on the noiseless amplification quadrature or noiseless deamlification quadrature, it is "dispersion-less[9]", otherwise it is "dispersion-like." In light of this, we now study a more intricate and interesting case where one mode of a two-mode squeezed state produced by the PIA is input into the PSA. Similar to the experiment outlined in Section 5.2, we investigate the "dispersive" behavior of the mutual information (MI) shared by the two modes by propagating one of them through the PSA.

5.4.1 Experimental setup

The detailed experimental layout is illustrated in Fig. 5.3 with the AOM removed from the probe seed beam path. The PIA cell is held at a temperature of 112 °C and pumped by a strong beam of light (350 mW, 800 μm $1/e^2$ diameter) blue-detuned from the center of the $5S_{1/2}$ $F = 3$ manifold to the center of the $5P_{1/2}$ Doppler-broadened transition (see the one photon detuning Δ in Fig. 5.3(b)). The two-photon detuning for the PIA is δ = -4 MHz. The 4WM process in this cell is seeded by a weak probe beam ($\sim$0.1 mW, 300 μm $1/e^2$ diameter) and generates

---

[9]After we take into account the reference delay at the maximal amplification and maximal deamplification.

bright-beam two-mode squeezed state consisting of an amplified probe beam and a generated conjugate beam[10]. The amplified probe beam is sent through the PSA constructed in the second vapor cell whose experimental details are provided in the prior section (Section 5.3.1). Detectors D_p and D_c are two intensity detectors measuring the intensity time traces of the probe and conjugate beams, whose AC parts are post-processed to calculate the MI between them. The number of points in each time trace is 10^5 with a sampling rate of 2 ns/sample.

5.4.2   Experimental results

We post-process the AC time traces by filtering them between 0.5 MHz to 5 MHz (3 dB points) using a 4th-order Butterworth band-pass filter with a slope of 80 dB/decade on both the low and high pass edges. The AC time traces are further filtered by the detector's roll-off at 4 MHz. The resulting time traces are used to determine the intensity-difference squeezing between the two beams by employing Eq. (4.11) derived in Section 4.4. In the absence of the PSA, we obtain -3.9 dB of intensity-difference squeezing within this bandwidth. One noteworthy fact (which we also have specified in Chapter 4) is that, we actually measure -5.8 dB of intensity-difference squeezing on a spectrum analyzer, and it is roughly constant over an analysis frequency range of 0.5 MHz to 2.5 MHz. The reason for us to enlarge the filtering bandwidth in the present experiment is to have more statistically independent samples. We will be specific on this matter in the next chapter. We use the AC time traces filtered over the same bandwidth used to measure the

---

[10]See Section 2.3.1 for details.

intensity-difference squeezing to calculate the MI.

The one-photon detuning Δ is varied in the experiment to change the PSA gain (See Figs. 5.3(b) and 5.3(c).). As the detuning is changed the PIA pump power is adjusted to keep both the power and the level of squeezing in the twin beams that are used in the measurement constant.

5.4.2.1   Calculation of mutual information

Instead of using the quantum mutual information formulated by Eq. (5.2) in Section 5.2, here we calculate the MI according to its classical definition,

$$I(p;c) = \sum_{1}^{N_p} \sum_{1}^{N_c} P(p,c) \log_2 \frac{P(p,c)}{P(p)P(c)}, \tag{5.5}$$

where $P(p,c)$ is the joint probability obtained by binning the intensities of the probe and conjugate AC time traces. $P(p)$ and $P(c)$ are the marginal probabilities for the intensities of the probe and conjugate AC time traces, respectively. N_p and N_c are the number of bins for the two time traces. We then shift the two time traces relative to each other so that we can get the MI as a function of the time shift, like the ones shown in Fig. 5.2. Since $\log_2$ is used, the MI calculated by Eq. (5.5) is in the unit of bits.

We want to highlight the difference between the two MI definitions given in Eq. (5.2) and Eq. (5.5). The MI definition in Eq. (5.2) has information in both the amplitude and phase quadratures, while the one in Eq. (5.5) has information only in the amplitude (or intensity) quadrature.

To illustrate the calculation of the MI, we plot the joint probability distribution at the *peak* time of the MI between the filtered probe and conjugate AC time traces of intensity in Fig. 5.6. We choose $N_p = N_c = 100$ as an example[11] to resolve fine details of the joint probability distribution.

(a)   (b)
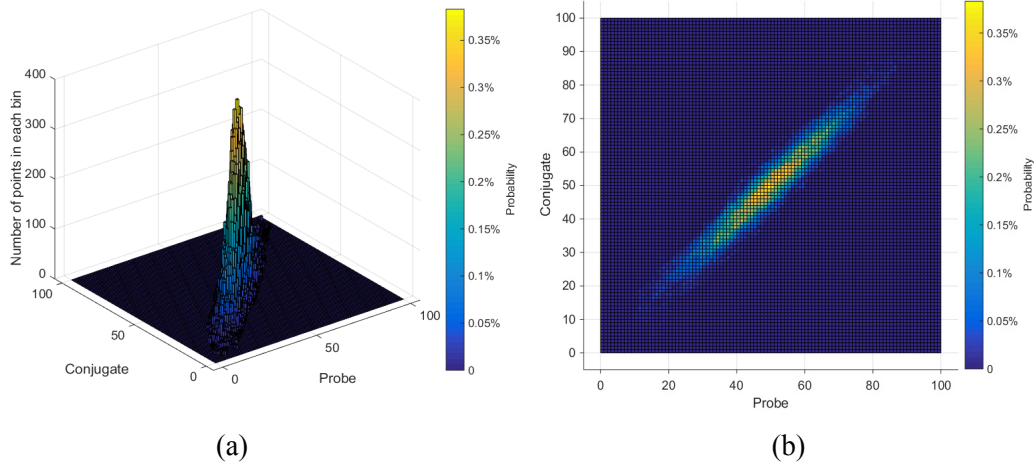
Figure 5.6: Joint probability distribution at the *peak* time of the MI between the filtered probe and conjugate AC time traces of intensity. (a) 2-D histogram of the joint probability distribution. (b) The joint probability distribution.

Figure 5.6(b) is the joint probability distribution $P(p, c)$ of the two modes. The x and y axes are the bin number in the filtered AC time traces for the probe and conjugate beams, respectively. The color bar indicates the probability of each bin. From Fig. 5.6(b), $P(p)$ and $P(c)$ can be calculated by summing up all probabilities of the columns and rows, respectively. Then, the MI at the *peak* time is readily obtained just by plugging $P(p, c)$, $P(p)$ and $P(c)$ into Eq. 5.5.

---

[11]The effect of number of bins on the calculation of MI is discussed in the Appendix B. There, we will show that 100 bins might be an overkill for calculating the MI under current experimental conditions. Therefore, unless stated otherwise, for the rest of the results shown in this chapter we use 30 bins for both the probe and conjugate time traces, which is sufficient for the present purposes.

By shifting the two time traces, we can plot the MI as a function of the time shift. Some examples are shown in Fig. 5.7. In the graph, the dash-dotted gray lines are 30 reference curves when the two PSA pumps are blocked, and the solid black line is their average whose peak value is 1.75 bits. In order to show the fidelity of the information transfer, all the MI peak heights are normalized to the peak of the solid black line. After passing through the PSA, the output probe is amplified or deamplified depending on the relative input phase. For each output (or each phase), we plot the MI as a function of the time shift and color-code it according to the amplification and deamplification of the probe beam as the red and blue in Fig. 5.7, respectively. If the peak timing of the output MI is advanced from the peak timing of the averaged reference MI, it is styled as a solid curve, and if its peak timing is delayed from the reference peak, it is styled as a dash-dotted curve.
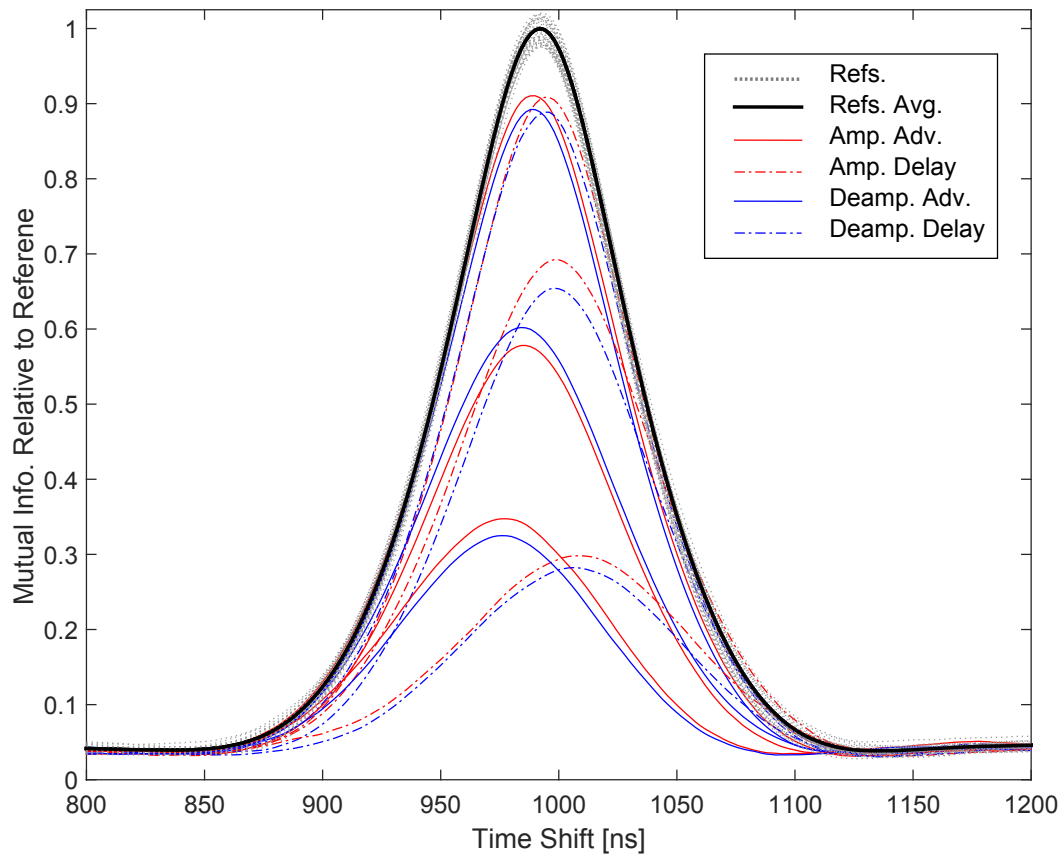
Figure 5.7: Mutual information as a function of the time shift. The dash-dotted gray lines are 30 reference curves when the PSA pumps are blocked and the solid black line is their average whose peak value is 1.75 bits. In order to show the fidelity of the information transfer, all the MI peak heights are normalized to the peak of the solid black line. The amplification and deamplification of the probe beam are color-coded as red and blue, respectively. The solid and dash-dotted line-styles are for the advanced and delayed MI, respectively.

By examining the MI curves in Fig. 5.7, we notice that although the peak of the MI of a bright two-mode squeezed state can be advanced, it is also degraded, and the leading edge is always bounded by the reference one within the experimental uncertainty. This observation is consistent with the red MI curve in Fig. 5.2.

121
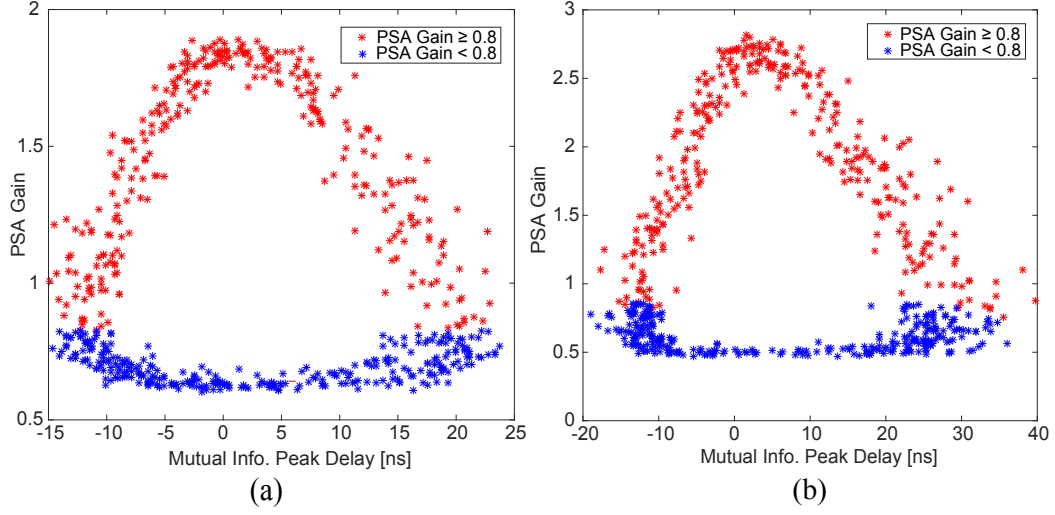
Figure 5.8: Parametric plots of the PSA gain versus the MI peak delay for (a) $\Delta =$ 1.4 GHz and (b) $\Delta = 1.3$ GHz. The red and blue color codes are for the PSA gain ≥ 0.8 and < 0.8, respectively.

5.4.2.2 PSA gain v.s. mutual information peak delay

By sufficiently sampling the probe outputs after passing through the PSA and plotting the MI versus the time shift for each output, as in Fig. 5.7, we are able to obtain a parametric plot of the PSA gain versus the MI peak delay. Figures 5.8(a) and (b) are the parametric plots of the PSA gain versus the MI peak delay for one photon detuning $\Delta = 1.4$ GHz and 1.3 GHz, respectively. In order to have sufficient digitization range[12] to calculate the MI, we take the data separately in two parts: PSA gain ≥ 0.8 and PSA gain < 0.8, which we respectively denote as the red and blue stars in Fig. 5.8. While taking the data with PSA gain < 0.8, we simply zoom in the oscilloscope to enlarge the dynamic range so that we can have enough digitization levels on the deamplified time traces.

It is evident that, in Fig. 5.8, the behavior of the MI of a bright two-mode

---

[12]We use an 8-bit oscilloscope, which has a maximal digitization level of $2^8 = 256$.

squeezed state propagating through the PSA is similar to the prior experiments using amplitude-modulated classical signals as the input to the PSA. In Fig. 5.9, we report all the parametric results together for the comparison. Notice that, the curves in the MI case (e) and (f) are noisier and asymmetric, which can be partially ascribed to the fact that the input probe beam to the PSA has an imperfect spatial profile. In the experiments using classical modulations, the amplitude-modulated input probe beam was out of a fiber and therefore has a perfect Gaussian profile. In the present experiment, however, the input probe beam to the PSA is the one after interacting with the PIA pump beam, which is from a 2 W TA without strict spatial profile cleansing (see Fig. 5.3(a)). It inevitably deviates the spatial profile of the probe beam from a perfect Gaussian, therefore giving rise to a less perfect phase-matching condition than in the experiments using classical modulations.

5.4.2.3 Peak height v.s. peak delay

We also plot the MI peak height as a function of the MI peak delay in Fig. 5.10 by extracting these parameters from Fig. 5.7. We use the same color codes as in Fig. 5.8 and normalize the MI peak heights to the averaged reference one when the PSA pumps are blocked (see the solid black curve in Fig. 5.7) in order to show the fidelity of the information transfer. Data points in the subfigures (a) and (b) are for the one photon detuning $\Delta = 1.4$ GHz and 1.3 GHz, respectively.

We can see from Fig. 5.10 that, when the MI peak heights are close to 1, their corresponding peak delays are close to 0, indicating the PSA is operating *noiselessly*
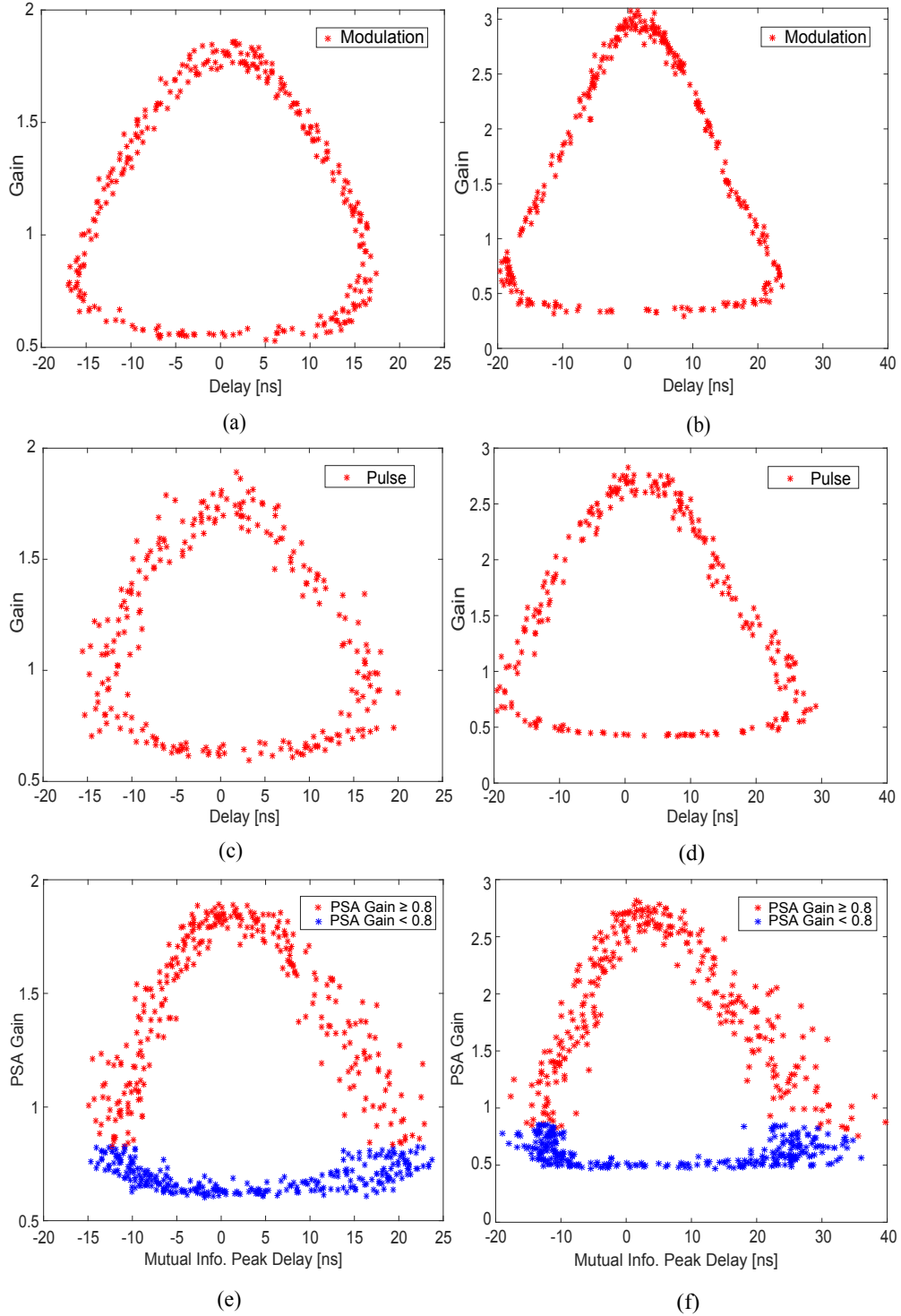
Figure 5.9: Parametric results from inputting (a) and (b): a sinusoidally amplitude-modulated classical signal; (c) and (d): a pulsed classical signal; and (e) and (f): the MI of a bright two-mode squeezed state. Data points in (a), (c) and (e) are for $\Delta = 1.4$ GHz, and data points in (b), (d) and (f) are for $\Delta = 1.3$ GHz. The red and blue color codes in (e) and (f) are for the PSA gain ≥ 0.8 and < 0.8, respectively. Subfigures (a), (b), (c) and (d) are from Fig. 5.5.

in either the maximal amplification or the maximal deamplification condition (see Fig. 5.8). While when the MI peak height is degraded, its peak timing can be either advanced or delayed, and the more the degradation, the more the advancement or delay. We can also learn from the blue stars that, although the PSA deamplifies the probe beam, the MI between the probe and conjugate can still be nearly as high as the reference MI without the PSA.

We speculate that the apparent "dispersive" behavior of the PSA seen in Fig. 5.9 is due to the "mixing of quadratures." Specifically, when the PSA is noiseless, i.e., the entire input signal is encoded in only one of the two "natural" quadratures — the maximally amplifying and maximally deamplifying quadratures, so that the output signal is either purely amplified or deamplified and is at the same quadrature angle as the input, as shown in Figs. 2.11 and 2.12 in Section 2.5, the PSA is also "dispersion-less." However, when the input signal is encoded on a combination of the two"natural" quadratures, the PSA rotates the input signal so that the output signal is a different mix of the two quadratures than at the input, as shown in Fig. 2.10 in Section 2.5. The PSA degrades the MI because of this operation, and in addition it produces the advance and delay that appears to be a "dispersion" effect.
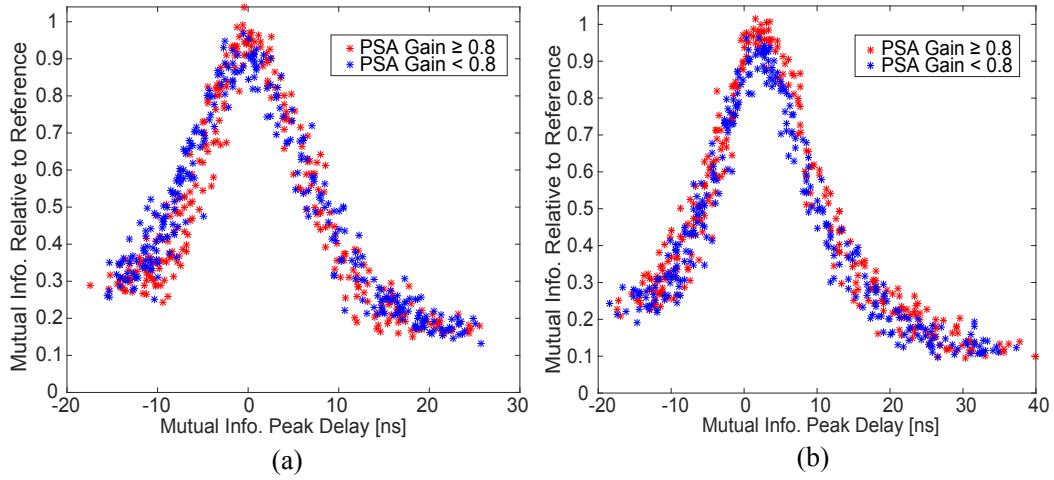
Figure 5.10: MI peak height as a function of the MI peak delay for (a) $\Delta = 1.4$ GHz and (b) $\Delta = 1.3$ GHz. In order to show the fidelity of the information transfer, all the MI peak heights are normalized to the averaged reference one when the PSA pumps are blocked (see the solid black curve in Fig. 5.7). The peak value of the reference MI is 1.75 bits. The red and blue color codes are for the PSA gain ≥ 0.8 and < 0.8, respectively.

5.4.2.4 Proving the MI of the twin beams contains contributions from the quantum correlations

Thus far, we have demonstrated the PSA's ability of advancing and delaying the peak of the MI of a bright two-mode squeezed state. We also have showed that when the PSA is operating noiselessly, it is capable of transmitting almost all the MI that exists in the original two-mode squeezed state, no matter if one of the modes is maximally amplified or maximally deamplified. Since the MI is partially determined by the quantum-mechanically correlated intensity fluctuations of a bright two-mode squeezed state, in this section, let us study how much "quantumness" associated with this MI.

To do this, we remove the PSA and replace the twin beams with two split

126
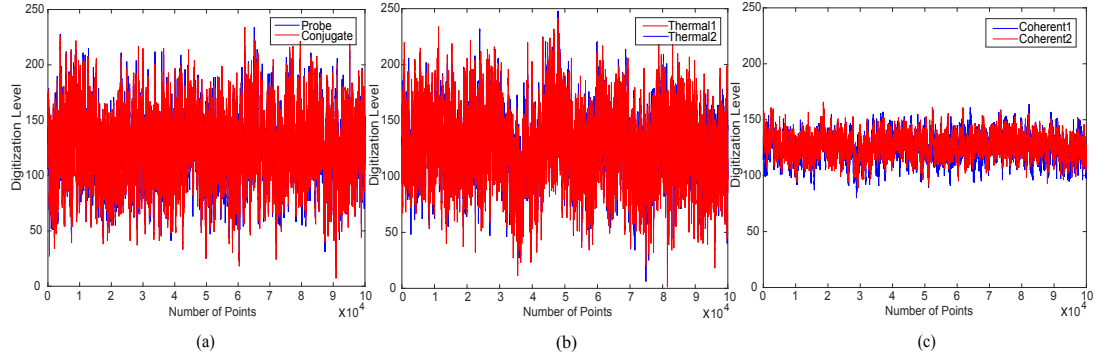
Figure 5.11: Examples of the filtered AC time traces of intensities used to calculate the MI for (a) Twin beams, (b) Split thermal beams and (c) Split coherent beams. All y-axes denote the digitization level ranging from 0 to 250 (the maximal digitization level is 256 from an 8-bit oscilloscope). All three cases share the same DC levels, and the twin beams (a) and split thermal beams (b) share the same AC levels as well.

thermal beams and two split coherent beams and compare the MI among these three cases. The two split thermal beams are from a single thermal beam split by a beamsplitter whose two outputs have the same DC and AC levels as the twin beams. In the same manner, the two split coherent beams are generated from splitting a single coherent beam by a beamsplitter whose two outputs have the same DC levels as the twin beams. Figure 5.11 is an example of the filtered (within 0.5 MHz to 5 MHz where the intensity-difference squeezing resides) AC time traces of these three cases.

An illustrative way to demonstrate the MI of the twin beams contains contributions from the quantum correlations is to bin the intensities of the AC time traces in Fig. 5.11 and compare their joint probability distributions at the *peak* time of the MI. Since the split coherent beams have the same intensities as the twin beams, thus the fluctuations in Fig. 5.11(c) represent the shot-noise level of fluctuations. The resulting joint probability distributions are plotted in Fig. 5.12 for comparison.
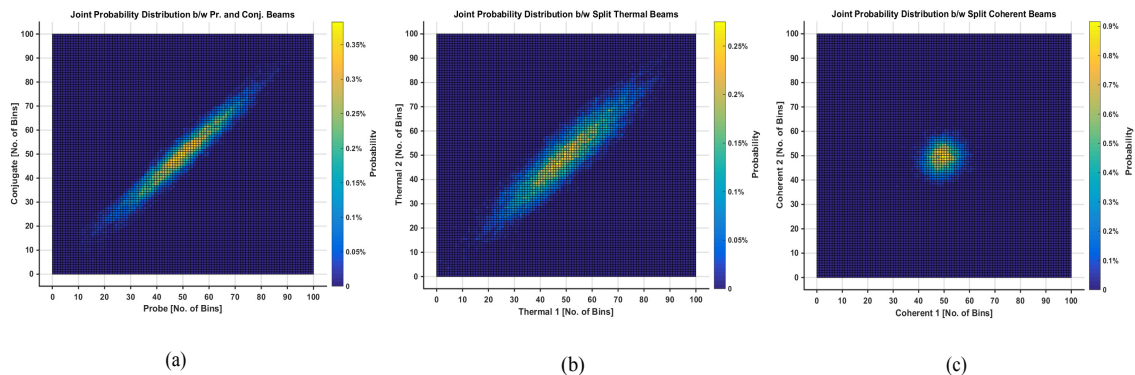
Figure 5.12: Joint probability distributions at the *peak* time of the MI for (a) twin beams, (b) split thermal beams and (c) split coherent beams, obtained by binning the intensities of the AC time traces in Fig. 5.11. The number of bins is 100 in order to resolve fine structures of the joint probability distributions.

Just as in Fig. 5.6, we choose the number of bins to be 100 to resolve fine structures of the joint probability distributions.

We see from Fig. 5.12 that the minor axis of the joint probability distribution of the split thermal beams is equal to the diameter of the joint probability distribution of the split coherent beams, implying all the correlations in the split thermal beams are shot-noise limited. The minor axis of the joint probability distribution of the twin beams, however, is smaller than the diameter of the joint probability distribution of the split coherent beams, manifestly indicating the existence of the sub-shot-noise correlations between the twin beams.

We can also normalize the filtered AC time traces in Fig. 5.11 so that they all have the same standard deviation as one of the twin beams. This normalization takes out the intensity imbalance between the twin beams caused by seeding the 4WM process. Also because of this normalization, for a given choice of bin size,
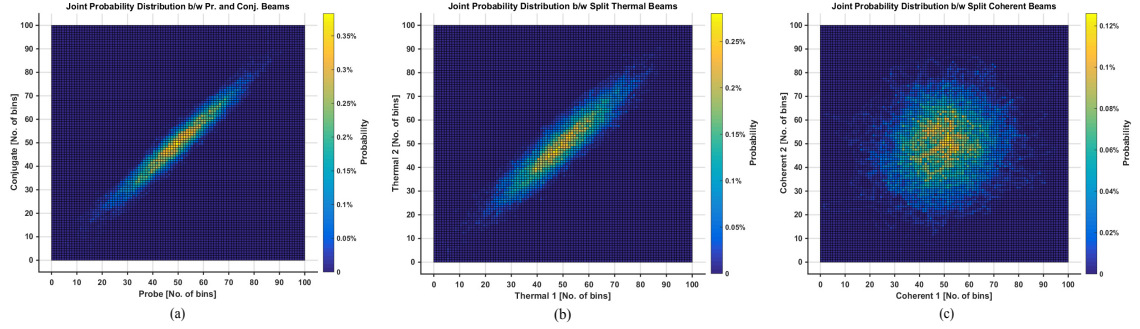
Figure 5.13: Joint probability distributions at the *peak* time of the MI for (a) twin beams, (b) split thermal beams and (c) split coherent beams. The filtered AC time traces are normalized so that they all have the same standard deviation as one of the twin beams.

each beam, no matter if it is a twin beam, a split thermal beam or a split coherent beam, would have the same amount of information, or the Shannon entropy, to be exact (see Appendix B for details). Then we can compare how much MI there is between any pair of beams, with perfect classical copying giving a MI equal to the information (in the Shannon sense, see Appendix B for details) of any one of the individual beams. These joint probability distributions are plotted in Fig. 5.13.

We now calculate the MI for each case and plot them as a function of the time shift in Fig. 5.14 for comparison. Each of the three curves is an average from 50 pairs of time traces. The calculation of the MI is based on the binning method shown in Fig. 5.13, which renders all the individual beams possessing the same amount of information (or the Shannon entropy) of 6.8 bits (see Appendix B for details). We see in Fig. 5.14 that, the twin beams have the most MI, and the extra amount of information acquired when comparing to that of the split thermal beams is due to the quantum correlations shared by the twin beams. The reason that all the MI curves have nonzero baselines is discussed in the Appendix B. The fact that the

MI curves of the twin beams and the thermal beams dip below the baselines is an artificial effect of the filtering. The 10 ns shift between the peaks of the MI curves of the twin beams and the thermal beams is due to the different group velocities for the two beams.

Based on Fig. 5.14, before being input into the PSA, the amount of the MI of the twin beams calculated by Eq. (5.5) is more than one could acquire classically, and the "more-than-classical" amount can be preserved when the PSA operates "noiselessly" (also "dispersion-lessly"). Also, by comparing the data in (e) and (f) with (a), (b), (c) and (d) in Fig. 5.9, we observe that, the "dispersion" of the PSA behaves the same regardless of whether the input is classical modulations or one mode of a two-mode squeezed state.
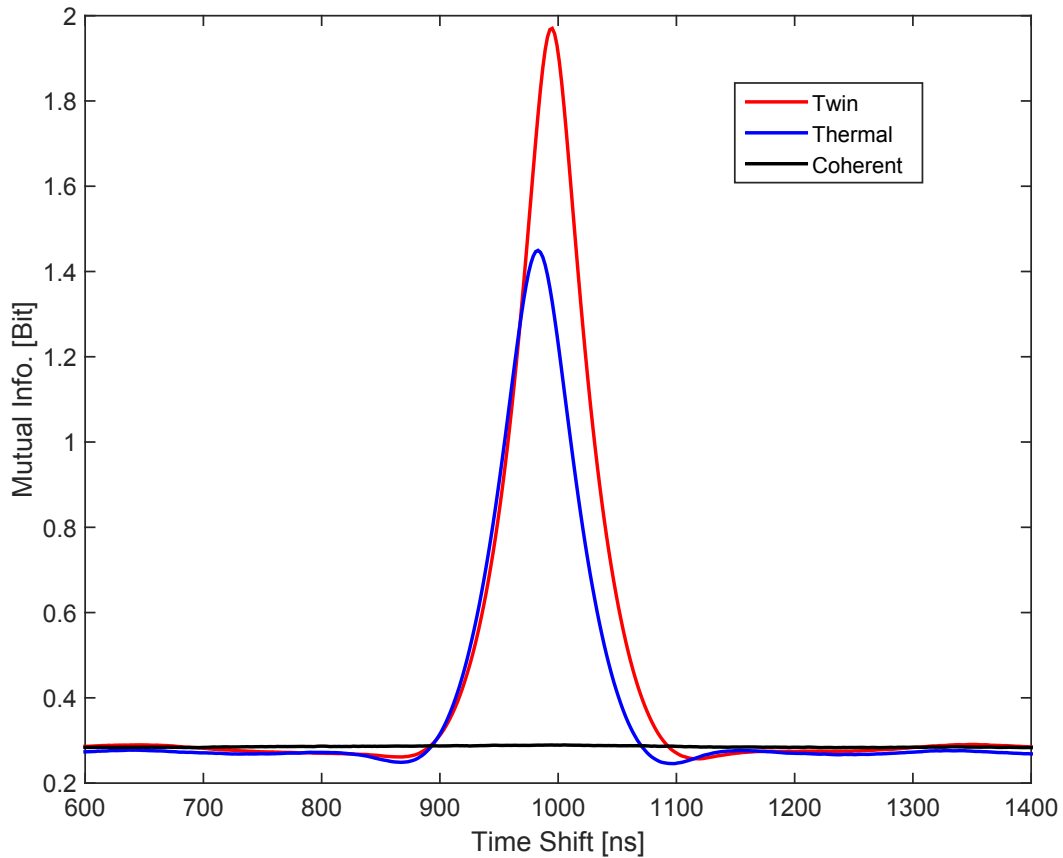
Figure 5.14: MI as a function of the time shift for twin beams (red), split thermal beams (blue) and split coherent beams (black). Each of the three curves is an average from 50 pairs of time traces. The calculation of the MI is based on the binning method shown in Fig. 5.13, which renders all the individual beams possessing the same amount of information (or the Shannon entropy) of 6.8 bits (see Appendix B for details). The reason that all the MI curves have nonzero baselines is provided in the Appendix B. The fact that the MI curves of the twin beams and the thermal beams dip below the baselines is an artificial effect of the filtering. The 10 ns shift between the peaks of the MI curves of the twin beams and the thermal beams is due to the different group velocities for the two beams.

5.5   Theoretical model

In this section, we explore the model that can explain the "dispersion" behavior of the PSA described in the preceding sections. A straightforward approach for us to

physically understand the "dispersion" behavior of the PSA is to measure the gain

line profile and calculate the group velocity from the measurement, as Glasser, *et al.*

did in [126]. In order to measure the gain line of the PSA, we keep the one-photon

detunings of the two pump beams fixed (see Fig. 5.3(c)) and scan the one-photon

detuning of the probe beam generated from a separate laser[13]. We measure the gain

lines with the two-photon detuning δ at +6 MHz, -4 MHz and -14 MHz, and plot

them in Fig. 5.15 alongside their corresponding plots of gain versus delay obtained

from injecting into the PSA a sinusoidally amplitude-modulated signal at 1 MHz and

allowing the PSA phase to drift. Note that there is no obvious change in the plots

of gain versus delay although the overall profiles of the gain lines change noticeably

among these three two-photon detunings.

An important feature of this gain line measurement is the ubiquitous oscilla-

tions. An example is plotted in Fig. 5.16 when the gain line in Fig. 5.15(b) is zoomed

in around 1 MHz. This is due to the fact that the output of the PSA is dependent

on the phase, $\phi_{\mathrm{PSA}} = (\phi_1 - \phi_p) + (\phi_2 - \phi_p)$, where ϕ_1 and ϕ_2 are the optical phases of

the pump beams and ϕ_p is the probe optical phase[14]. Since the probe beam is from

a third laser and when it is tuned away from the center frequency the two pumps

---

[13]As opposed to prior experiments where all the beams are derived from the same laser.

[14]See Section 2.4.3 in Chapter 2 for detailed derivations. There, the phases of the two pumps
are denoted by ϕ_b and ϕ_c, and the phase of the probe is denoted by ϕ_i.
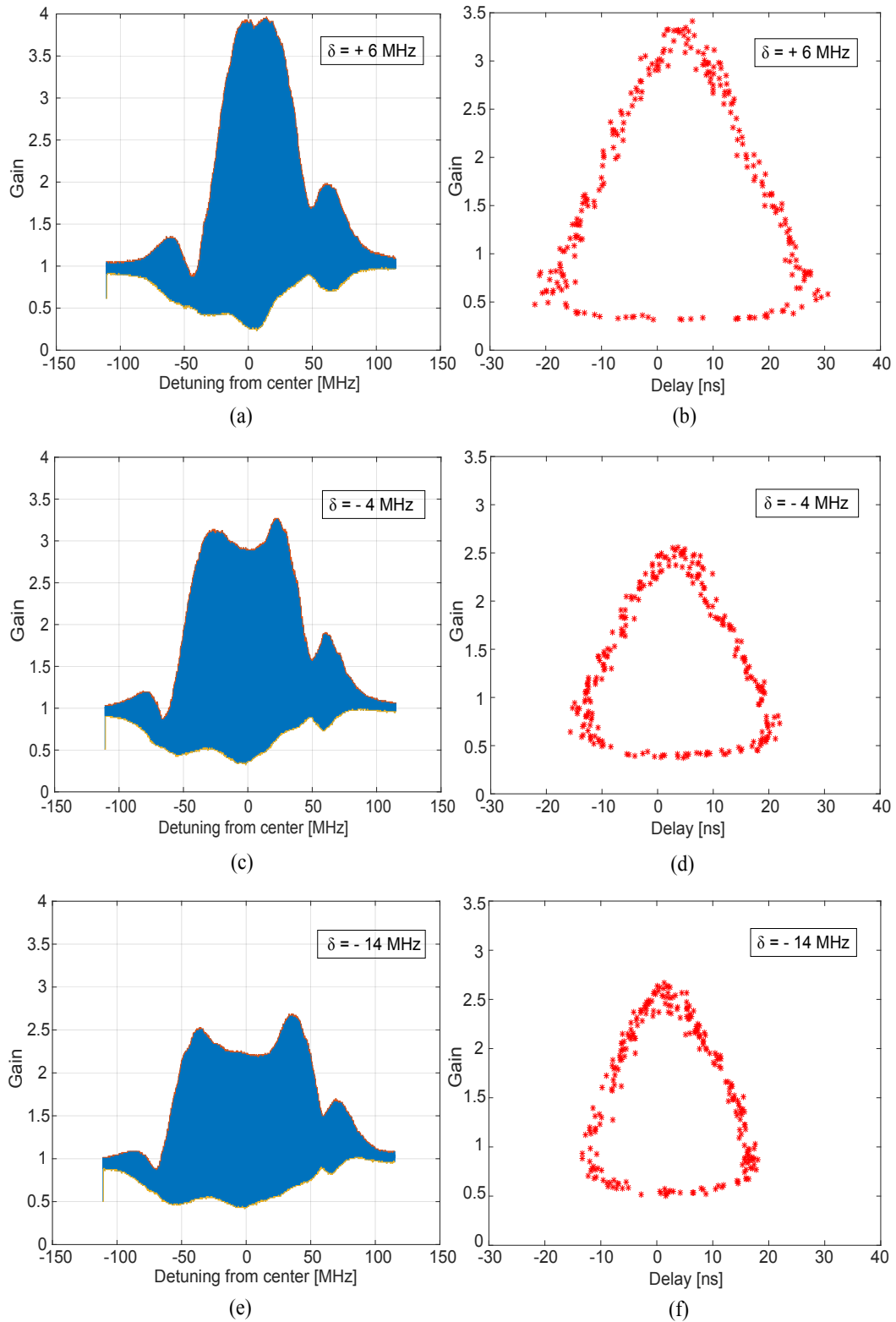
Figure 5.15: Profiles of the gain lines and their corresponding plots of gain versus delay for (a) and (b): δ=+6 MHz, (c) and (d): δ=-4 MHz and (e) and (f): δ=-14 MHz. The plots of gain versus delay are obtained from inputting to the PSA a sinusoidally amplitude-modulated signal at 1 MHz.

(i.e., $\nu_p \neq (\nu_1 + \nu_2)/2$, see Fig. 5.3(a) and (c)), ϕ_{PSA} becomes

$$\phi_{\mathrm{PSA}}(t) = (\phi_1(t) - \phi_p(t)) + (\phi_2(t) - \phi_p(t))$$

$$= [(\frac{\nu_1}{2\pi}t + \phi_1) - (\frac{\nu_p}{2\pi}t + \phi_p)] + [(\frac{\nu_2}{2\pi}t + \phi_2) - (\frac{\nu_p}{2\pi}t + \phi_p)] \qquad (5.6)$$

$$= (\frac{\nu_1 + \nu_2 - 2\nu_p}{2\pi})t + [(\phi_1 - \phi_p) + (\phi_2 - \phi_p)].$$

Obviously, ϕ_{PSA} is now oscillating at the angular frequency of $(\nu_1 + \nu_2 - 2\nu_p)/2\pi$, making the output of the PSA oscillate accordingly, and the further the detuning of the probe frequency from the center frequency of two pump beams, the faster the oscillation of the PSA output. It is therefore difficult for us to determine the group index from the gain line measurement[15]. For the rest of this section, we provide a theoretical model, which does not require the knowledge of the gain line but still gives good agreement with the experimental results.

We consider the simplest case where the input is a sinusoidally amplitude-modulated classical signal (See Section 5.3.2.1), which is composed of a carrier, a positive and a negative sideband in the frequency domain. The essence of this theoretical model is to have distributed (i.e., divide the whole medium into multiple sections) PSA gain on the carrier as well as on both the positive and negative sidebands but to have distributed loss only on the negative sideband.

An input purely amplitude-modulated signal can be written as

$$E_{\mathrm{in}}(t) = [1 + A\cos(\Omega t + \beta)]e^{i\phi}$$
$$= [1 + \alpha e^{i\Omega t} + \alpha^* e^{-i\Omega t}]e^{i\phi}, \qquad (5.7)$$

---

[15]Or maybe the calculation of the gain line is not meaningful at all.
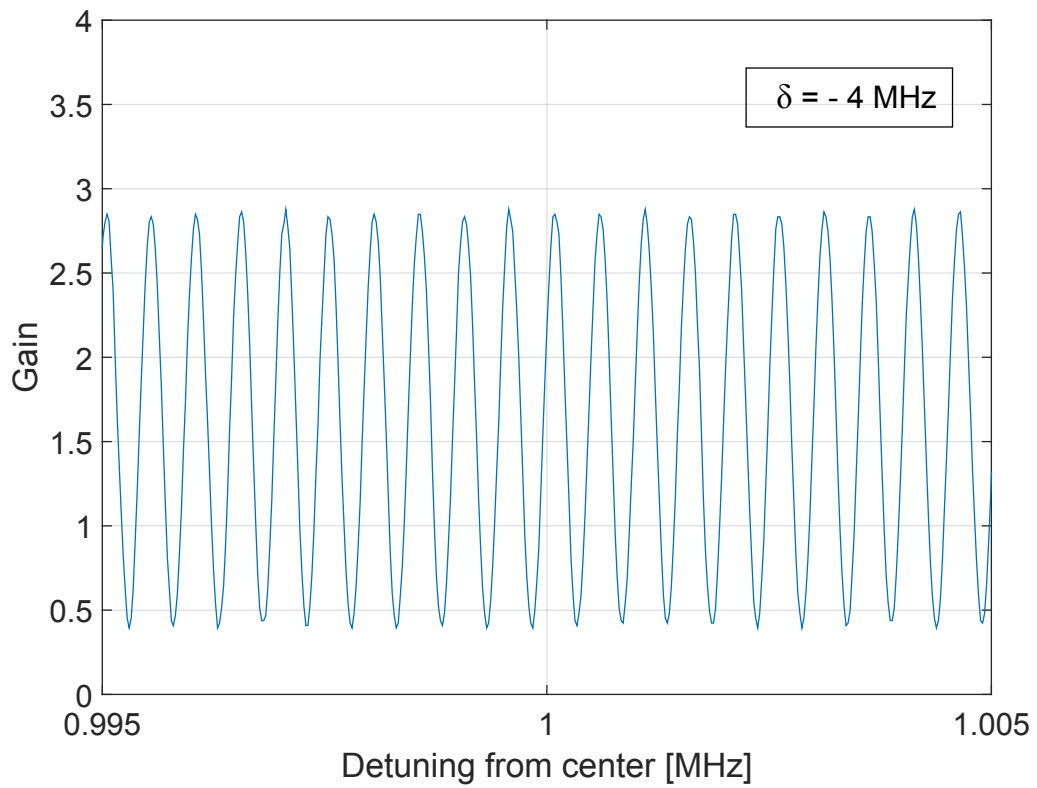
Figure 5.16: A zoomed-in version of the experimentally measured gain line in Fig. 5.15(b) around 1 MHz.

where $\alpha = (1/2)Ae^{i\beta}$, A is the modulation depth, $\Omega = 1$ MHz is the modulation frequency, and ϕ is the phase of the input field. $A = 0.15$ can be well determined experimentally. One can think of the input field in terms of the carrier and two sidebands at $\pm\Omega$. The basic defining equation of the classical phase-sensitive linear amplifier is [85]

$$E_{\text{out}}(t) = E_{\text{in}}(t)\cosh r + E_{\text{in}}^*(t)\sinh r, \qquad (5.8)$$

where the parameter r is related to the maximal gain of the PSA as $G_{\text{PSA}} = e^{2r}$ (See Section 2.4.3).

Since the amplifier is linear (in the electric field) we can consider the effect on each piece of the input field separately. We have considered the carrier (or "DC") part in Chapter 3. The effect of the amplifier on the positive and negative frequency sidebands is

$$E_{\text{out}}^+(t) = \alpha e^{i\Omega t}e^{i\phi}\cosh r + \alpha^* e^{-i\Omega t}e^{-i\phi}\sinh r,$$
$$E_{\text{out}}^-(t) = \alpha^* e^{-i\Omega t}e^{i\phi}\cosh r + \alpha e^{i\Omega t}e^{-i\phi}\sinh r, \qquad (5.9)$$

where $E_{out}^+(t)$ and $E_{out}^-(t)$ are the output fields for the positive and negative sidebands, respectively. From Eq. 5.9, we see that the amplifier mixes the positive and negative sidebands, i.e., the output from the positive frequency input has both positive and negative frequency components and likewise for the negative frequency input. The final electric field, when we reassemble all three pieces (carrier and $\pm\Omega$

sidebands) is

$$E_{\text{out}}(t) = (\cosh r + e^{-2i\phi} \sinh r)(1 + \alpha e^{i\Omega t} + \alpha^* e^{-i\Omega t})e^{i\phi}$$

$$= (\cosh r + e^{-2i\phi} \sinh r)E_{\text{in}}. \tag{5.10}$$

The output field is the same as the input field, multiplied by an overall factor, which, upon squaring to get intensity, gives the AC and DC gain we identified in Chapter 3. Therefore, a purely amplitude-modulated input signal simply gets amplified or deamplified.

In a multimode description of the amplifier one can imagine that the effect of the amplifier depends on the sideband frequency. In particular, if in contrast to the treatment of Eq. (5.10), we imagine that the amplifying medium has a linear index of refraction variation as in the usual fast-and-slow-light case, then one sideband could be shifted slightly ahead in phase and one symmetrically behind in phase (relative to the carrier). Thus the angle β on the output might be different from that on the input. If angle β changes by $\Delta\beta$ in going through the amplifier, then this amounts to a shift in the peak of the modulation envelope relative to the underlying carrier wave:

$$1 + A\cos(\Omega t + \beta) \to 1 + A\cos(\Omega t + \beta + \Delta\beta) = 1 + A\cos[\Omega(t + \tau) + \beta], \quad (5.11)$$

where $\tau = \Delta\beta/\Omega$. Thus the modulation envelope is shifted in time by time τ, which could be either positive or negative. That is the usual fast-and-slow-light effect.

In addition to the above discussion where the carrier and both sidebands only

137

experience gain and no loss, let us consider introducing a small amount of loss to one of the sidebands, and have the gain and loss distributed across the medium[16]. For simplicity, we assume the loss is on the negative sideband. The gain and loss sections can then be described by the matrices

$$\boldsymbol{G} = \begin{pmatrix} \cosh r_n & \sinh r_n \\ \sinh r_n & \cosh r_n \end{pmatrix} \tag{5.12}$$

and

$$\boldsymbol{L} = \begin{pmatrix} 1 & 0 \\ 0 & t_n \cdot e^{i\Delta\beta_n} \end{pmatrix}, \tag{5.13}$$

respectively. Here, r_n is the gain parameter for each gain section, and t_n is the transmission of the negative sideband in each loss section. $\Delta\beta_n$ is the phase shift of the negative sideband relative to the carrier.

We can calculate the output fields of the carrier, E_{co}, and the two sidebands, $E_{so}^{\pm}$ by cascading the gain and loss sections:

$$\begin{pmatrix} E_{co} \\ E_{co}^* \end{pmatrix} = \boldsymbol{G}^N \cdot \begin{pmatrix} E_{ci} \\ E_{ci}^* \end{pmatrix} \quad \text{and} \quad \begin{pmatrix} E_{so}^+ \\ E_{so}^{-*} \end{pmatrix} = (\boldsymbol{G} \cdot \boldsymbol{L})^N \cdot \begin{pmatrix} E_{si}^+ \\ E_{si}^{-*} \end{pmatrix}, \tag{5.14}$$

where $E_{ci} = 1 \cdot e^{i\phi}$, $E_{si}^+ = \alpha e^{i\Omega t} \cdot e^{i\phi}$ and $E_{si}^- = \alpha^* e^{-i\Omega t} \cdot e^{i\phi}$ are the input fields of the carrier, the positive and negative sidebands, respectively. N is the total number of gain and loss sections.

It is straightforward to obtain the relation between r_n and the overall maximal

---

[16]The ideal of describing the nonlinear process by a "distributed gain and loss" model is from the Refs. [127] and [128].

138

gain of the PSA, G_{PSA}, since $G_{\mathrm{PSA}} = (e^{2r_n})^N$, therefore $r_n = \ln G_{\mathrm{PSA}}/(2N)$. It is also easy to calculate the overall phase shift as $\Delta\beta = N\Delta\beta_n$. The overall transmission of the negative sideband, however, is a bit more involved to be characterized. Equation 5.9 tells us that after each section, the PSA mixes the positive and negative sidebands converting one to the other. Although we introduce the non-unity transmission only to the negative sideband for each section, because of the mixing operation of the PSA, both sidebands are actually affected by this non-unity transmission at the output of each section. It is therefore not trivial to assign a transmission or a gain only to a specific sideband.

Gathering the output fields, E_{co} and $E_{so}^{\pm}$, together, we can have the output intensity:

$$I_{out} = (E_{co} + E_{so}^{+} + E_{so}^{-})^2. \tag{5.15}$$

For each phase ϕ of the input field, the output intensity is a periodic function of time (i.e., it is amplitude-modulated like the input) whose peak positions can be used to determine the advance/delay relative to the input reference signal as in Fig. 5.4(a). The PSA gain at each input phase ϕ can be obtained from the gain of the carrier, which is just the output intensity of the carrier, $I_{co} = E_{co} \cdot E_{co}^*$, since the input intensity of the carrier, $I_{ci} = E_{ci} \cdot E_{ci}^* = 1$. Then, by varying the input phase ϕ from 0 to 2π and assigning reasonable values to the free parameters of G_{PSA}, t_n and $\Delta\beta_n$, we are able to make parametric plots of gain versus delay as in Figs. 5.17, 5.18 and 5.19. Without loss of generality, we assume the amplitudes for both the positive and negative sidebands are real ($\beta = 0$ in Eq. 5.7), and we set the total

139

number of gain and loss sections $N = 10$.

For simplicity, in plotting Figs. 5.17 and 5.18, we also set $\Delta\beta_n = 0$. Figure 5.17 is plotted for 3 maximal PSA gains, all with the negative sideband transmission $t_n = 0.95$. Figure 5.18 is plotted for 3 negative sideband losses, all with the maximal PSA gain $G_{\mathrm{PSA}} = 3$.

It can be seen from Figs. 5.17 and 5.18 that, the advance and delay appear to be more prominent with larger G_{PSA} and greater loss on the negative sideband. Greater G_{PSA} also tends to change the shape of the plot while greater loss on the negative sideband only enlarges the horizontal spread but maintains the shape of the plot.
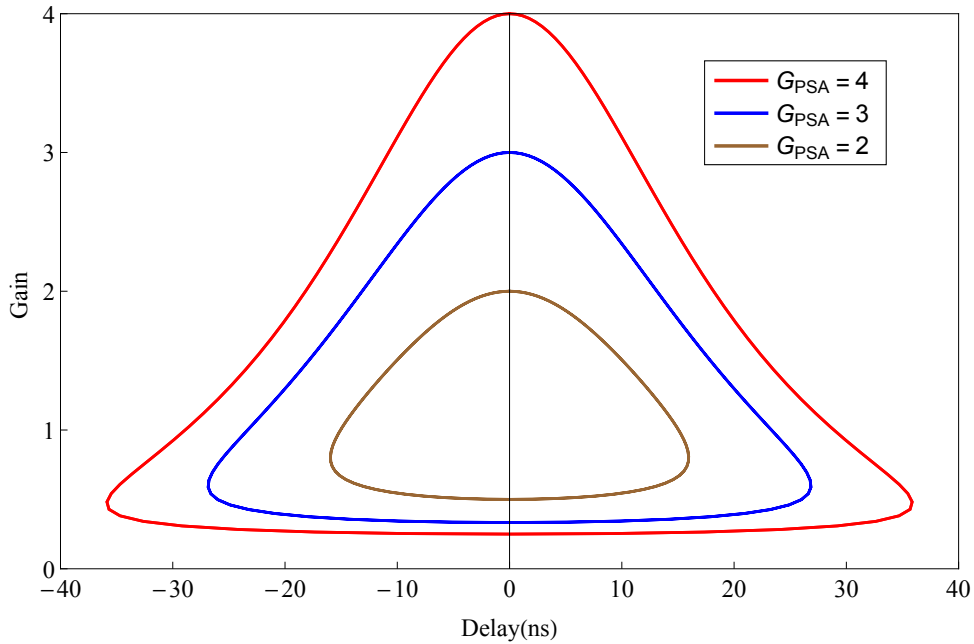
Figure 5.17: Parametric plots of gain versus delay for the maximal PSA gain $G_{\mathrm{PSA}} = 2$ (brown), 3 (blue) and 4 (red), respectively. Other parameters are $t_n = 0.95$, $\Delta\beta_n = 0$ and $N = 10$.
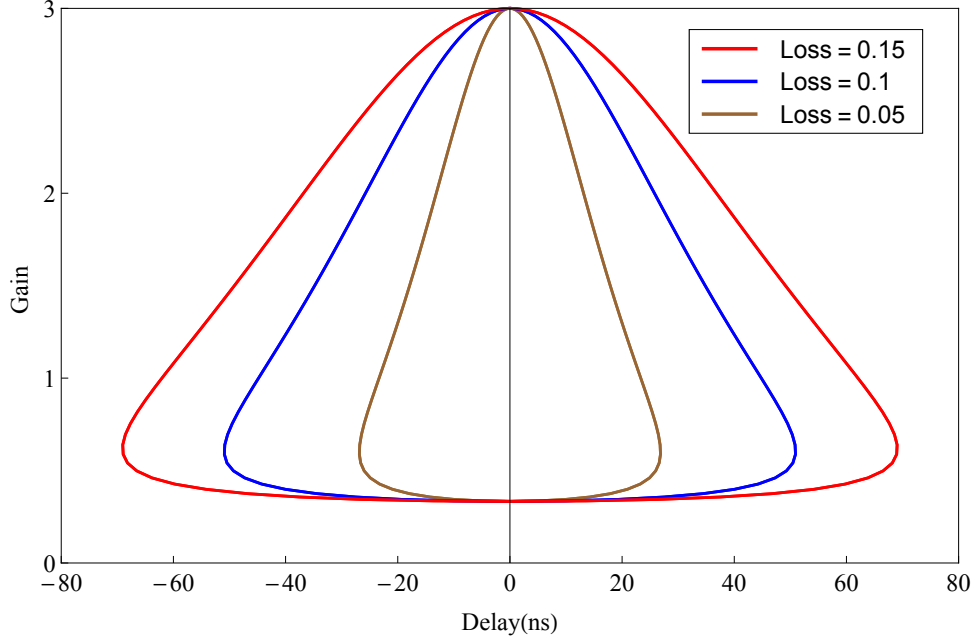
Figure 5.18: Parametric plots of gain versus delay for the negative sideband transmission $t_n = 0.95$ (brown), 0.90 (blue) and 0.85 (red), respectively. Other parameters are $G_{\mathrm{PSA}} = 3$, $\Delta\beta_n = 0$ and $N = 10$.

To examine the effect of the phase shift $\Delta\beta_n$ on the advance and delay, we also plot the parametric plots of gain versus delay for 3 values of $\Delta\beta_n$ in Fig. 5.19. We can learn from these plots that, the phase shift $\Delta\beta_n$ simply moves the overall shape forward or backward in time, as does the phase shift $\Delta\beta$ in Eq. 5.11 in the case of the usual fast-and-slow-light effect.

If we set the transmission of the negative sideband $t_n = 1$ and keep all the rest of the parameters unchanged, Fig. 5.19 becomes Fig. 5.20. This clearly shows that, under our theoretical model, the advance and delay, or the apparent "dispersive" behavior of the PSA is purely due to the imbalanced gain or loss on one of the sidebands. In other words, this "dispersive" behavior can be described as the frequency-dependent gain or loss as opposed to the frequency-dependent index of

refraction in the usual fast-and-slow-light effects.
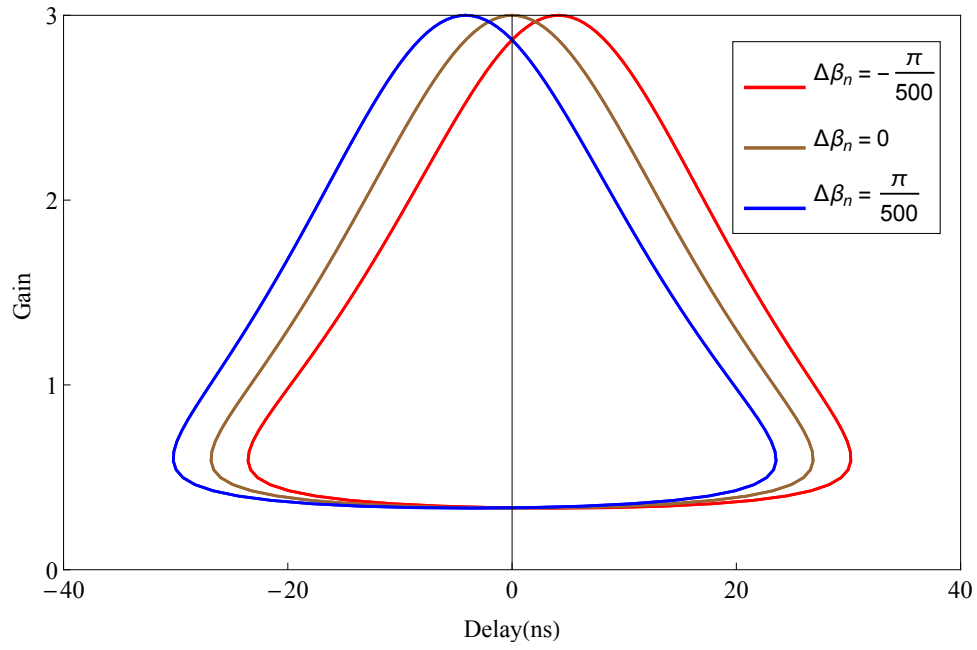
Figure 5.19: Parametric plots of gain versus delay for the phase shift $\Delta\beta_n = -\pi/500$ (red), 0 (brown) and $\pi/500$ (blue), respectively. Other parameters are $G_{\mathrm{PSA}} = 3$, $t_n = 0.95$ and $N = 10$.
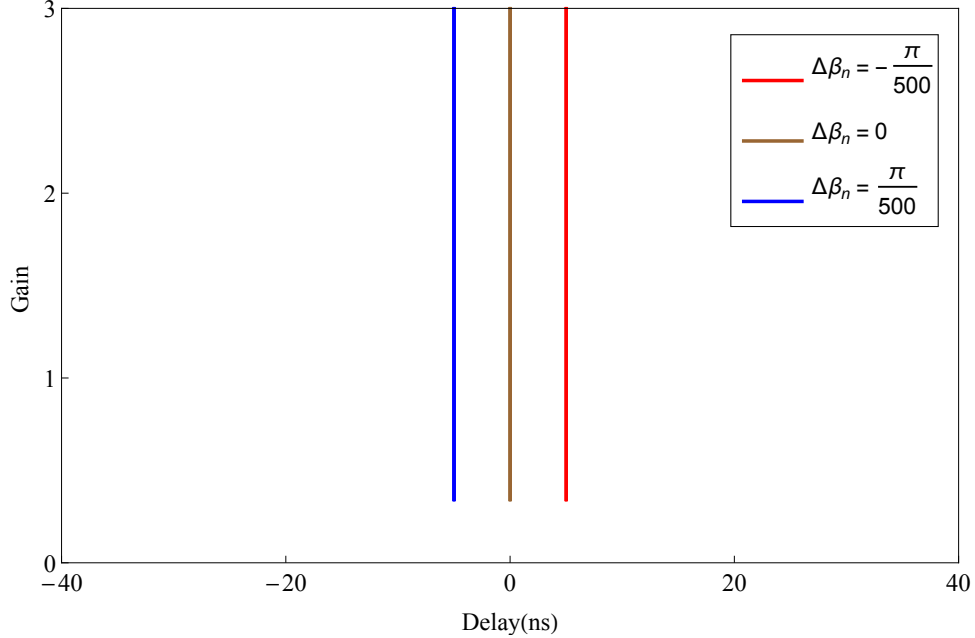
Figure 5.20: Parametric plots of gain versus delay for the phase shift $\Delta\beta_n = \text{-}\pi/500$ (red), 0 (brown) and $\pi/500$ (blue), respectively. Other parameters are $G_{\mathrm{PSA}} = 3$, $t_n = 1$ and $N = 10$.

We now apply our model to fit the experimental data. We use the same data shown in Figs. 5.9(a) and 5.9(b) since the input is a sinusoidally amplitude-modulated classical signal. We fit the theory curves to the data in Fig. 5.21 manually with fitting parameters enumerated in the caption. We find an excellent agreement between the theory and the data with reasonable fitting parameters.

Because of the similarities between the MI data shown in Figs. 5.9(e) and 5.9(f) and the classical modulation data shown in Figs. 5.9(a) and 5.9(b), we can also apply our theory to fit the MI data. Because the theory is developed with a monochromatic classical input, we expect it will not fit the MI data as well as the modulation data since the MI data is analyzed within a frequency bandwidth of 0.5 MHz to 5 MHz. The results are shown in Fig. 5.22 with the fitting parameters enumerated in the
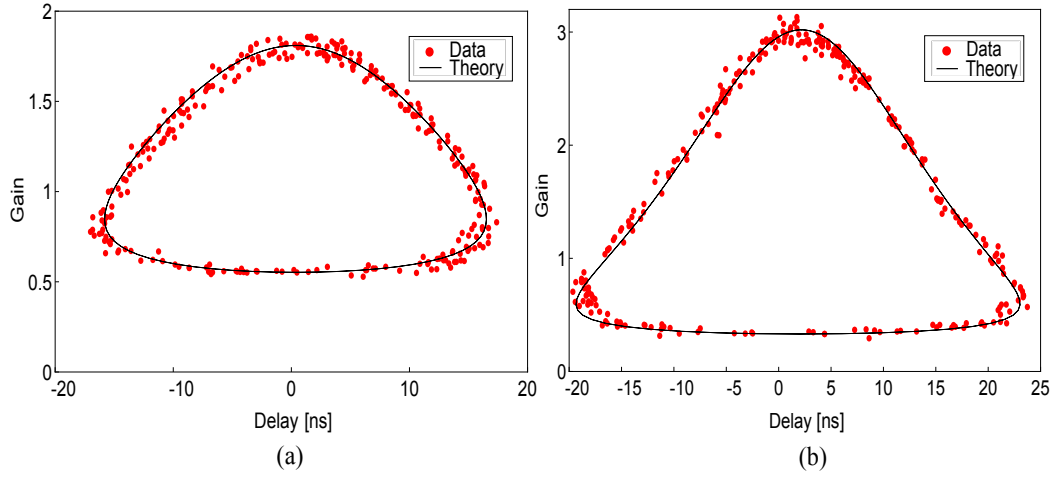
Figure 5.21: Theoretical fits to the data shown in Figs. 5.9(a) and 5.9(b). The fitting parameters for (a) are $G_{\text{PSA}} = 1.81$, $t_n = 0.961$ and $\Delta\beta_n = -\pi/5000$. The fitting parameters for (b) are $G_{\text{PSA}} = 3.02$, $t_n = 0.946$ and $\Delta\beta_n = -\pi/2000$. Both with $A = 0.15$, $\Omega = 1$ MHz and $N = 10$.
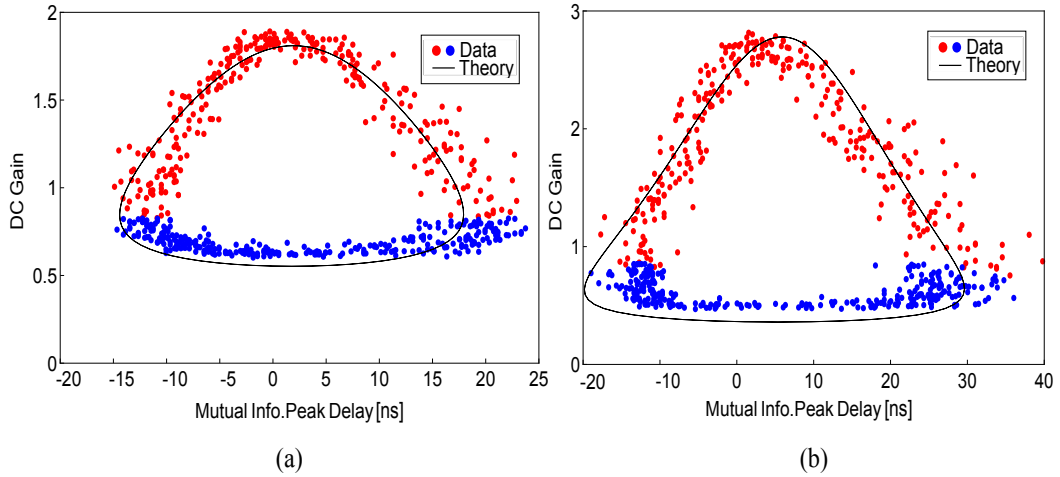
Figure 5.22: Theoretical fits to the data shown in Figs. 5.9(e) and 5.9(f). The fitting parameters for (a) are $G_{\text{PSA}} = 1.81$, $t_n = 0.961$ and $\Delta\beta_n = -\pi/1000$. The fitting parameters for (b) are $G_{\text{PSA}} = 2.82$, $t_n = 0.946$ and $\Delta\beta_n = -\pi/500$. Both with $A = 0.15$, $\Omega = 1$ MHz and $N = 10$.

caption. We see that the fits are decent[17] and the fitting parameters are at least for most of the part quite similar to the ones used in Fig. 5.21.

We can go one step further to fit the data shown in Fig. 5.10. Once we obtain the fits in Fig. 5.22, we gain the knowledge of the MI peak delay as a function of the input phase ϕ (since the gain on the vertical axis is a function of ϕ). Moreover, since the joint probability distribution for the probe and conjugate time traces is a bivariate normal distribution (both of the probe and conjugate marginal distributions are normally distributed), therefore, there is an exact relationship between the MI and the intensity correlation coefficient M_{XC} of the twin beams formulated by Eq. 4.10 in Section 4.4 [129]:

$$I(p;c) = -\frac{1}{2}\log_2(1 - M_{\mathrm{XC}}^2),\tag{5.16}$$

where $I(p;c)$ is the MI in the unit of bits since $\log_2$ is used. The simple quantum-mechanical model developed in Section 4.4 enables us to attain the relationship between the normalized cross-correlation function and the input phase ϕ, then from Eq. 5.16, the relationship between the MI and ϕ can be easily derived as well. Since we now know both the MI and the MI peak delay as functions of ϕ, we thus are able to make a theoretical parametric plot of MI versus MI peak delay by varying ϕ from 0 to 2π and fit it to the data shown in Fig. 5.10. The results are shown in Fig. 5.23. Although the fits exhibit some deviations from the data, e.g., they do not cover the notable asymmetry between the wings of the advance and delay, they do

---

[17]One should not expect the fits to be perfectly working since the data is broadband.
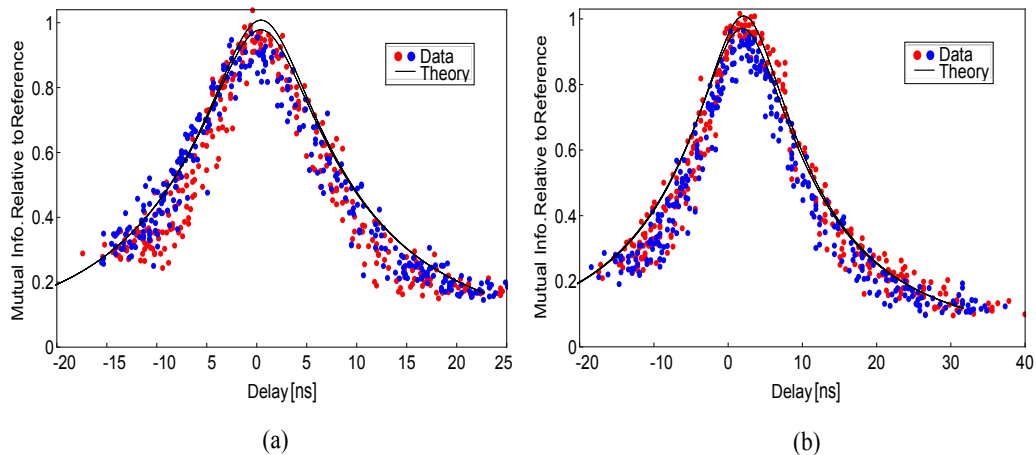
Figure 5.23: Theoretical fits to the data shown in Fig. 5.10. Derivation of the fits is detailed in the text. In order to show the fidelity of the information transfer, all the MI peak heights are normalized to the peak of the reference one, which is 1.75 bits.

capture most of the features of the data.

5.6   Conclusions

We elaborate in this chapter two experiments that explore the fast-and-slow-light effects on the propagation of the mutual information (MI) shared by the twin beams of a two-mode squeezed state produced by a 4WM-based PIA.

The first experiment utilizes a second 4WM-based PIA as a dispersive medium, and the input signal is from a vacuum two-mode squeezed state. We find in this experiment that although the peak of the MI between the modes can be advanced when the PIA acts as a gain-assisted fast-light medium, the degradation of the MI due to the added noise from the phase-insensitive gain appears to prevent an advancement of the leading edge. In contrast, we demonstrate a significant delay of both the leading and trailing edges of the MI when the PIA acts as a gain-assisted

slow-light medium.

The second experiment replaces the second PIA with a 4WM-based PSA as the "dispersive" medium, and instead of using an input signal from a vacuum two-mode squeezed state, we input to the PSA a signal from a bright two-mode squeezed state. Our experimental observations make us speculate that the apparent "dispersive" behavior of the PSA is due to the "mixing of quadratures." Specifically, we find that when the PSA is noiseless, i.e., the entire input signal is encoded in only one of the two "natural" quadratures (the maximally amplifying and maximally deamplifying quadratures) so that the output signal is either purely amplified or deamplified and is at the same quadrature angle as the input, the PSA is also "dispersion-less." However, when the input signal is encoded on a combination of the two"natural" quadratures, the PSA rotates the input signal so that the output signal is a different mix of the two quadratures than at the input. Because of this operation the PSA degrades the MI, and in addition it produces the advance and delay that appears to be a "dispersion" effect.

We also provide a theoretical model capable of explaining our observations. The model adopts the idea that, in addition to the phase shift between the positive and negative frequency sidebands in the case of usual fast-and-slow-light effects, one of the sidebands also sustains a partial transmission during the propagation through the PSA. We demonstrate that it is this partial transmission (or imbalanced gain) of one sideband that gives rise to the apparent "dispersive" behavior of the PSA, and with reasonable fitting parameters, our theory fits the experimental observations very well. We can use our model to describe this "dispersive" behavior as the

frequency-dependent gain or loss as opposed to the frequency-dependent index of refraction in the usual fast-and-slow-light effects.

Chapter 6:   Concluding remarks

In this chapter, we highlight the main results obtained from the work presented in this thesis. We also provide an outlook of some possible investigations that can be implemented in the future as continuations to the research presented here.

6.1   Summary of results

The work presented in this thesis studies the optical properties of a quantum-noise-limited phase-sensitive amplifier (PSA). This PSA is created through the four-wave mixing process in ^{85}Rb vapor, and has already been demonstrated to have the ability of generating multi-spatial-mode single-beam quadrature squeezed states of light [58] and of noiselessly amplifying hundreds of spatial modes [72].

We first take advantage of the phase-sensitivity of the amplifier and study the effects of input amplitude and phase modulation on the output of the PSA. We show that PSA signals can be used as a diagnostic tool for quantifying the phase modulation depth of an input signal and are consistent with established homodyne techniques. We find that both AOMs and optical choppers can inadvertently add phase modulation to a light field in addition to the desired amplitude modulation. This can drastically alter the results in applications using PSAs. In each case, we

demonstrate that the amount of phase modulation can be reduced by adjusting the angle of incidence between the beam path and the modulator.

We then demonstrate the use of an optical PSA to reduce the effect of non-unity quantum efficiency of an intensity detector, which is an important limitation in making continuous variable measurements of quantum states. We show that the use of the PSA allows us to more accurately measure the intensity correlation coefficient and intensity-difference squeezing of a two-mode squeezed state. We also show, in a proof-of-principal experiment, this scheme also works for a homodyne detector. Therefore the system of a PSA operating at a large gain followed by a detector with imperfect quantum efficiency would in principle approach a "perfect detector."

We commit the rest of the thesis to investigate the "dispersive" behavior of the mutual information (MI) of a two-mode squeezed state propagating through the PSA. We speculate that, based on the results from our investigations using a phase-insensitive amplifier as the dispersive medium [29], the added noise which degrades the information also prevents the information from traveling superluminally. Our present experimental observations make us believe that it is the PSA's "mixing of quadratures" that gives rise to the apparent "dispersive" behavior of the PSA. Specifically, we find that when the PSA is noiseless, i.e., the entire input signal is encoded in only one of the two "natural" quadratures (the maximally amplifying and maximally deamplifying quadratures) so that the output signal is either purely amplified or deamplified and is at the same quadrature angle as the input, the PSA is also "dispersion-less." However, when the input signal is encoded on a combination of the two "natural" quadratures, the PSA rotates the input signal so that the output

signal is a different mix of the two quadratures than at the input, and because of this operation the PSA degrades the MI, and in addition it becomes "dispersive." We also find that, the "dispersion" of the PSA behaves the same regardless of whether the input is classical modulations or one mode of a two-mode squeezed state.

A model which is capable of fitting our experimental results reasonably well is also developed. The theory assumes that in addition to the phase shift between the positive and negative frequency sidebands in the case of usual fast-and-slow-light effects, one of the sidebands also sustains a partial transmission during the propagation through the PSA. It is this partial transmission (or imbalanced gain) of one sideband that gives rise to the apparent "dispersive" behavior of the PSA. We can use our model to describe this "dispersive" behavior of the PSA as the frequency-dependent gain or loss as opposed to the frequency-dependent index of refraction in the usual fast-and-slow-light effects.

6.2   Outlook

In regard to the experimental results presented in this thesis, we have some views of the future investigations that one could take on.

6.2.1   The "perfect detector" experiment

In Section 4.5.3 of Chapter 4, we discuss the experiment using homodyne detectors. There, the initial two-mode vacuum squeezing is only -2 dB, after the propagation through the PSA and the engagement of quantum-noise lock-in, the

available vacuum squeezing reduces to -1.5 dB. Moreover, the adverse effect of power imbalance between the twin beams on the vacuum squeezing is not taken care of since there are no time traces recorded. Therefore, there is undoubtedly much room to improve the experiment and to make better and more convincing measurements. Once we succeed in achieving a better measurement of the two-mode vacuum squeezing, we could further pursue a good measurement of the entanglement between the two modes in the presence of loss. An even more challenging but highly rewarding proposal is to use our scheme to overcome detector efficiency limitations in quantum imaging applications since our PSA is capable of operating on multiple spatial modes [72].

6.2.2   The mutual information experiment

During the research on the "dispersive" behavior of the MI of a two-mode squeezed state propagating through the PSA, most of our questions have centered on Fig. 5.7. The most notable difference of this graph from Fig. 5.2 is the MI curves with delayed peaks. In Fig. 5.2, both of the leading and trailing edges of the MI curve are delayed by the phase-insensitive-gain-assisted slow-light system. However, in Fig. 5.7, the trailing edges of the MI curves with delayed peaks are also bounded by the reference one within the experimental uncertainty. Although we have proved that the apparent "dispersive" behavior of the PSA is not a typical fast-and-slow-light effect, we are not so sure whether this trailing edge bounding is due to physical effects or just due to the not-so-great statistics. Since the MI curves in Fig. 5.7 are

calculated from the filtered time traces within 0.5 MHz to 5 MHz (and are further filtered by the detector's roll-off at 4 MHz), the time interval between statistically independent samples is 250 ns, this implies an over-sampling of 125 points given our sampling rate is 2 ns/sample. The total number of points in our time traces is 10^5 (so that the data acquisition time window is 0.2 ms, during which the PSA phase is a constant), which gives the number of statistically independent points of 800 in calculating the MI curves in Fig. 5.7. A straightforward improvement would then be to take the MI data without so much over-sampling during a correlation time and with a better resolution (using a 12-bit digitizer rather than an 8-bit oscilloscope). Certainly, there is plenty left to do.

Appendix A   Calculation of gain and loss inside the PIA (source) cell[1]

The correlation properties of a two-mode squeezed state emitted by a lossless PIA are solely determined by its gain. In the experiment, however, the atomic absorption and scattering from the ^{85}Rb atoms in the PIA cell inevitably introduce loss. Therefore, a complete description of the PIA requires a distributed gain and loss model [127, 128]. Here we adopt a simpler model that assumes an ideal lossless PIA followed by loss as shown in Fig. 4.2(a). To determine the gain of the PIA and the beamsplitter transmissions η_{a1} and η_{b1}, we take auxiliary measurements of laser intensities and component transmissions.

The main issues are that η_{a1} includes losses that occur inside the cell and change as a function of laser detuning, and that the gain required by the model is different from the intensity gain measured in the presence of loss. Previous studies have shown that the losses on the probe beam are much larger than those on the far detuned conjugate beam [101]. Here we assume there is no loss due to the vapor on the conjugate beam. To model the losses in the PIA, we introduce an effective probe

---

[1]This appendix is associated with the theoretical predictions for the intensity cross-correlation and the intensity-difference squeezing of the *bright* twin-beam case in Chapter 4. For the case of two-mode vacuum squeezing discussed in Section 4.5.3, we had not gone through this calculation.

beam transmission, $\eta_{4\mathrm{WM}}$, which contributes to $\eta_{\mathrm{a}1}$ along with the ordinary optical losses, whereas $\eta_{\mathrm{b}1}$ is due simply to ordinary optical losses that can be measured directly. The advantage of this model is that one is able to determine the desired G_{PIA} and $\eta_{4\mathrm{WM}}$ just by measuring the optical powers of the probe and conjugate beams with and without the presence of the pump beam. The detailed derivation is as follows.

We shine a probe beam with optical power P_s into the PIA cell, temporarily blocking the pump beam and detuning the probe so that absorption in the atomic vapor is negligible. The probe beam experiences losses due to reflection from the cell windows, downstream optics, and the non-unity quantum efficiency of the detector. The measured optical power is

$$P_r = P_s \cdot \eta_{\mathrm{a}1}^{\mathrm{off}} \cdot \eta_{\mathrm{a}2}, \tag{A.1}$$

where $\eta_{\mathrm{a}1}^{\mathrm{off}} = 0.92$ is the transmission of the PIA cell windows and the optical elements up to the position where the PSA cell would be inserted, and $\eta_{\mathrm{a}2} = 0.89$ is the product of the transmission of the optics after the PSA insertion point and the quantum efficiency of the detector.

With the pump beam present, and the probe frequency reset to its usual detuning, the probe power gets amplified to P_p and a conjugate beam is generated with power P_c, where

$$P_p = P_s \cdot G_{\mathrm{PIA}} \cdot \eta_{\mathrm{a}1}^{\mathrm{on}} \cdot \eta_{\mathrm{a}2}, \tag{A.2}$$

$$P_c = P_s \cdot (G_{\text{PIA}} - 1) \cdot \eta_{\text{b1}} \cdot \eta_{\text{b2}}, \tag{A.3}$$

and $\eta_{\text{a1}}^{\text{on}} = \eta_{\text{a1}}^{\text{off}} \cdot \eta_{\text{4WM}}$. Here $\eta_{\text{b1}} = 0.94$ is the transmission of the PIA cell windows and the optical elements up to the position of the conjugate detector, and $\eta_{\text{b2}} = 0.90$ is the quantum efficiency of the detector.

Solving for P_s in Eq. (A.1) and plugging it into Eqs. (A.2) and (A.3), one obtains

$$\frac{P_p}{P_r} = G_{\text{PIA}} \cdot \frac{\eta_{\text{a1}}^{\text{on}}}{\eta_{\text{a1}}^{\text{off}}} = G_{\text{PIA}} \cdot \eta_{\text{4WM}}, \tag{A.4}$$

$$\frac{P_c}{P_r} = (G_{\text{PIA}} - 1) \cdot \frac{\eta_{\text{b1}} \cdot \eta_{\text{b2}}}{\eta_{\text{a1}}^{\text{off}} \cdot \eta_{\text{a2}}}. \tag{A.5}$$

The gain of the PIA G_{PIA} and the effective probe beam transmission η_{4WM} are readily calculable from Eqs. (A.4) and (A.5) using the measured optical transmissions and known detector quantum efficiencies, and the measured powers P_p, P_c and P_r.

As noted in the main text, when we adjust the one photon detuning, Δ, to vary the PSA gain, we also adjust the pump power in the PIA to maintain the same measured squeezing level. Following this procedure we find that for $\Delta = 1.4$ GHz the effective PIA parameters are $G_{\text{PIA}} = 3.0$ and $\eta_{\text{4WM}} = 0.92$ and thus $\eta_{\text{a1}}^{\text{on}} = 0.85$. For $\Delta = 1.3$ GHz the effective PIA parameters are $G_{\text{PIA}} = 3.3$ and $\eta_{\text{4WM}} = 0.90$ and thus $\eta_{\text{a1}}^{\text{on}} = 0.83$. With these numbers plugged into the model described in Section 4.4, the correlation properties of the modes a_i and b_i can thus be fully characterized.

In calculating AC noise powers one needs to account, by modifying η_{a2} and η_{b2}, for the finite signal power separations from the electronic noise floors, as discussed in the main text. The intensity-difference squeezing predicted by this theory is -5.6 dB, which is very close to the experimental value of -5.8 dB. This verifies that the approximation of treating the distributed cell loss by a lumped value after the cell is sufficiently accurate for the present purposes.

Appendix B The effect of number of bins on the calculation of the mutual information[1]

In this appendix, we explore the effect of number of bins on the calculation of the mutual information (MI). In Section 5.4 of Chapter 5, we use the classical definition to calculate the MI:

$$I(p;c) = \sum_{1}^{N_p} \sum_{1}^{N_c} P(p,c) \log_2 \frac{P(p,c)}{P(p)P(c)}, \tag{B.1}$$

where $P(p,c)$ is the joint probability of the probe and conjugate AC time traces. $P(p)$ and $P(c)$ are the marginal probabilities for the probe and conjugate, respectively. N_p and N_c are the number of bins for the two time traces. This approach of calculating the MI clearly depends on the choice of the number of bins N_p and N_c. Intuitively, one would think the more the number of bins, the more the information one would gain since more bins implies finer resolution to the small fluctuations in the time traces. However, since every piece of data acquisition equipment has a digitization limit, like an 8-bit oscilloscope has a maximal digitization level of $2^8 = 256$, it is an overkill to bin the traces beyond the digitization limit set by the apparatus. Moreover, the MI is a characterization of the "similarities" between the two beams,

---

[1]This appendix is associated with Section 5.4 in Chapter 5.
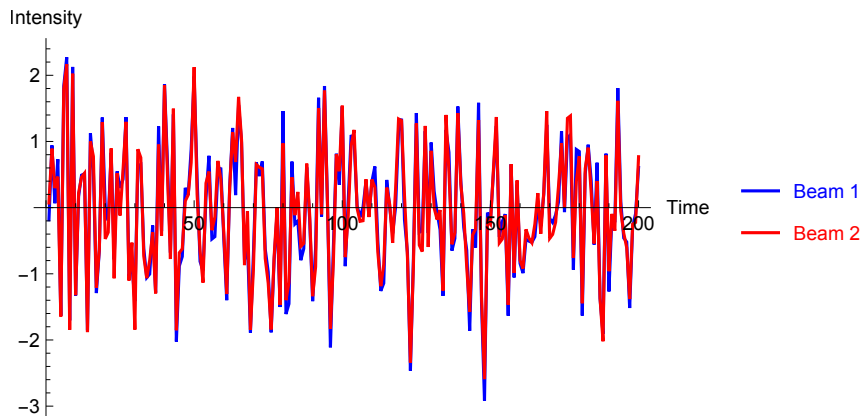
Figure B.1: Simulations of the time traces of the two beams. The standard deviations of the correlated and uncorrelated parts are 1 and 0.125, respectively.

it should be a finite value set by the physical properties of the two beams, increasing the number of bins should not help one to acquire more information once all the "similarities" have been procured. For each individual beam, however, the amount of information (or the Shannon entropy) is a monotonic function of the number of bins.

To better understand this binning effect, let us first make some simulations. We generate a random time trace and make a copy of it, this would be a pair of perfectly correlated beams (or the intensity fluctuations of the beams, to be exact). We then generate two random uncorrelated time traces with a much smaller size and add each one to each beam. The resulting time traces are the mimicries of the time traces we take from the experiment. An example is shown in Fig. B.1 where the standard deviations of the correlated and uncorrelated parts are 1 and 0.125, respectively. Note that the total number of points in the time traces is 10^5, consistent with the experiment, Fig. B.1 only shows the first 200 points.

We now bin these two time traces with different number of bins to calculate
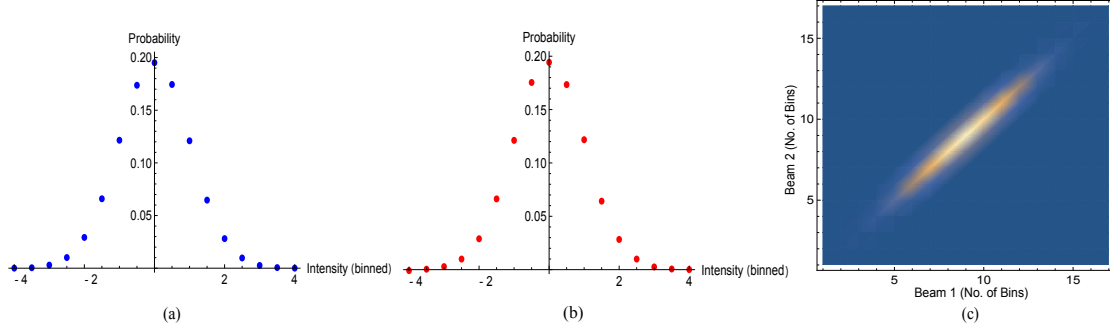
Figure B.2: Probability distributions of each beams, (a) and (b), and the joint probability distribution of the two beams, (c), when binned with 17 bins. The information in each beam is 3.07 bits calculated by the definition of the Shannon entropy. The MI is 1.95 bits.

the MI between them. Figure B.2 is an example with the number of bins of 17. We plot the individual probability distributions of the two beams in Figs. B.2(a) and B.2(b), and plot the joint probability distribution in B.2(c). We can calculate the information contained in each beam binned with N bins from the definition of the Shannon entropy, $H = -\sum_{i=1}^{N} P_i \log_2 P_i$, where N is the number of bins and P_i is the probability of each bin. With the number of bins of 17, the information in each individual beam is 3.07 bits, and the MI between them is 1.95 bits.

In Fig. B.3, we plot the information (both in individual beams and the MI) as a function of the number of bins for two pairs of time traces, one has an uncorrelated part with a standard deviation of 0.25, and the other one has an uncorrelated part with a standard deviation of 0.125. In both cases, the standard deviation of the perfectly correlated part is 1. Figure B.3 depicts that, as the number of bins increases, so do the information in each individual beams, the MI, however, are plateaued out after an initial growth. Also, it can be seen that the MI from the pair with the smaller uncorrelated part reaches the plateau at a greater number of bins than the
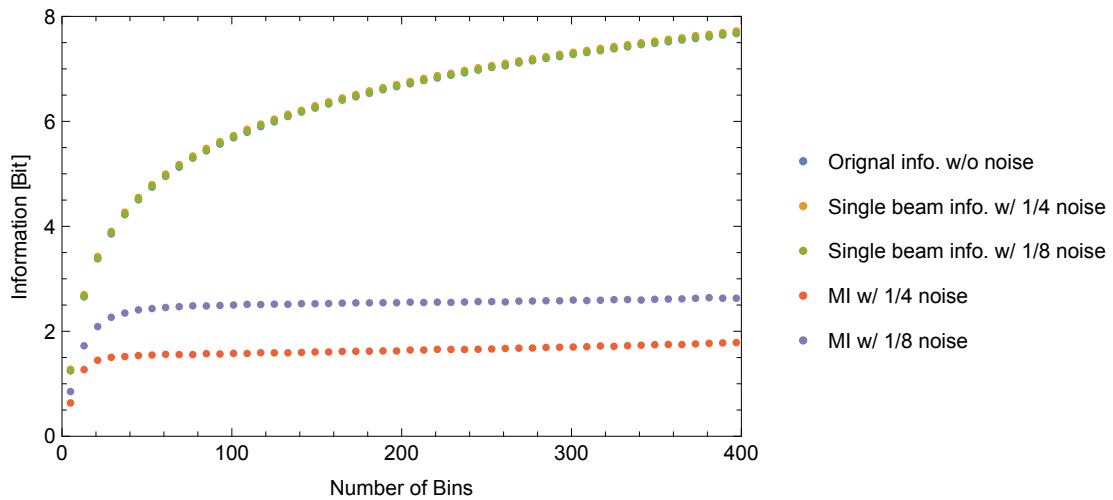
Figure B.3: Information in individual beams and the MI as a function of the number of bins for two pairs of simulated time traces. The "1/4 noise" and "1/8 noise" in the legend denote the standard deviations of the uncorrelated parts are 0.25 and 0.125, respectively. The standard deviation of the perfectly correlated part is 1 in both cases. The overlapping of the three list plots of the single beam information indicates adding a small uncorrelated part to the initial time trace has no appreciable effect on the amount of information it originally possesses. The amount of information of a single beam is solely determined by the number of bins.

one with the greater uncorrelated part, and the plateaued MI value is also higher for the pair with the smaller uncorrelated part. This is because resolving smaller uncorrelated fluctuations requires finer bins with narrower bin width, therefore more bins are needed to fully acquire the MI. The overlapping of the three list plots of the single beam information indicates adding a small uncorrelated part to the initial time trace has no appreciable effect on the amount of information it originally possesses. The amount of information of a single beam is solely determined by the number of bins. Whereas, the MI degrades substantially when even a small amount of randomness is added[2].

In this demonstration, it seems that using a lot of bins (within the digitization limit of the apparatus) is not a terrible idea, if one only cares about the *absolute* amount of the MI, not the one *relative* to the amount of information in each individual beam (increasing monotonically with the number of bins). However, in what follows, we prove that this is actually not a good idea in real life with all kinds of physical limitations.

We now shift the two machine-generated time traces to simulate our analysis of attaining the MI as a function of time shift shown in Fig. 5.14 in Section 5.4.2.4 of Chapter 5. The results of the simulated MI versus time shift calculated with different number of bins are plotted in Fig. B.4 using both Matlab and Mathematica. The number of points in the simulated time traces is 10^5, consistent with the experiment. For all the plots produced by both Matlab and Mathematica, we use the same

---

[2]Note that, if there is no uncorrelated part added to the perfectly correlated pair of time traces, i.e., one is the copy of the other, the MI between them is just the Shannon entropy of the individual beam.
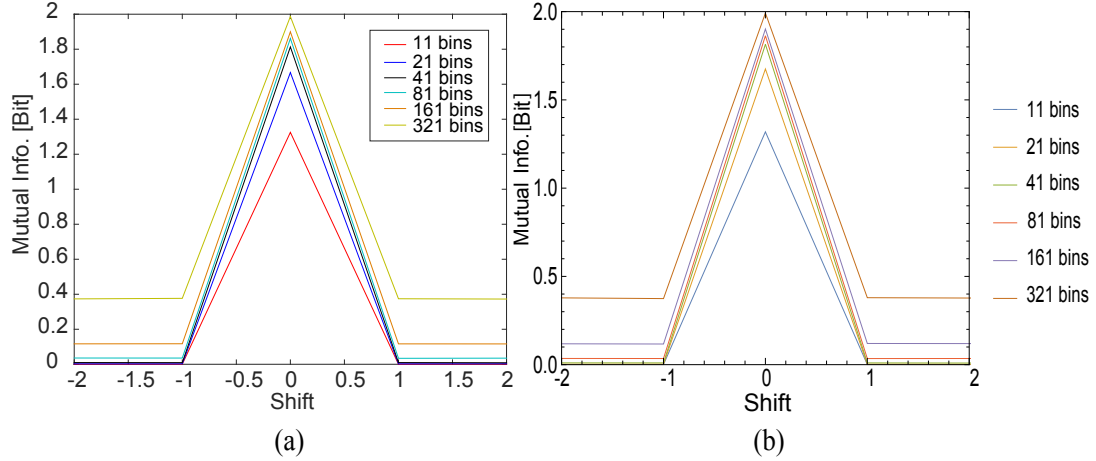
Figure B.4: Simulated MI as a function of time shift calculated with different number of bins using (a) Matlab and (b) Mathematica. The number of points in the simulated time traces is 10^5, consistent with the experiment.

pair of time traces generated by the random number generator in Matlab. In this simulation, the standard deviation of the uncorrelated part is 0.25, and the standard deviation of the perfectly correlated part is kept at 1. We see that as the number of bins increases, both of the MI peak and the baseline increases, but the baseline rises more aggressively than the peak does when the number of bins is large. If we subtract the baseline value from the peak value for each number of bins, we end up with the graph in Fig. B.5 where the results from the Matlab and Mathematica are plotted together. They are in good agreement and both show the reduction of the MI when the number of bins are greater than 81.

Figures B.4 and B.5 clearly tell us that, for time traces containing a finite number of points, using a large number of bins is detrimental to the calculation of the MI, as the nonzero baseline becomes more prominent when the number of bins is large.
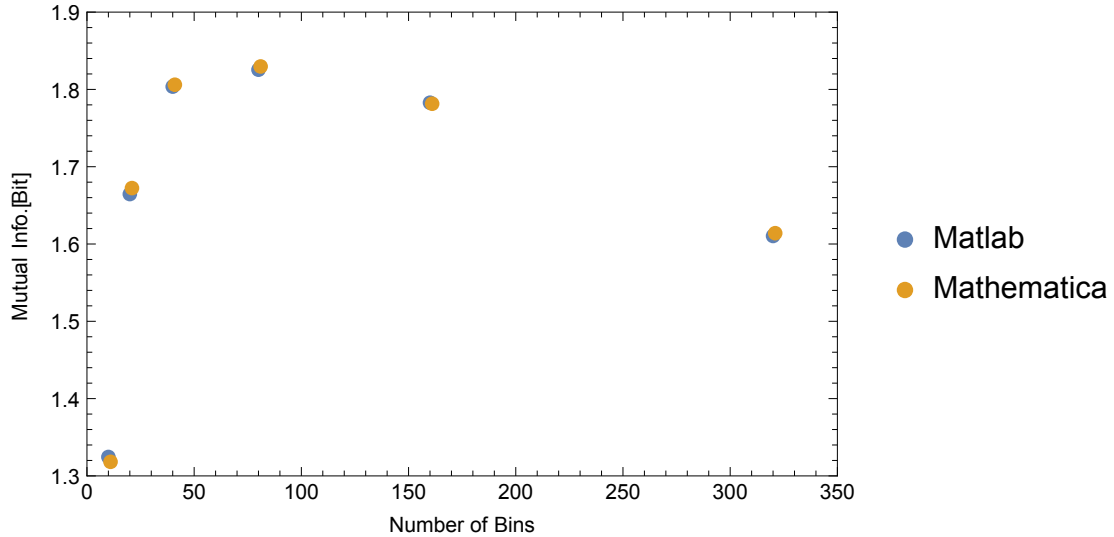
Figure B.5: MI peak value minus the baseline value as a function of the number of bins plotted for both Matlab (blue dots) and Mathematica (brown dots).

Let us now find out the physics and/or mathematics that gives rise to the nonzero baseline. Consider a simpler case where the information is in a single beam. As usual, bin the data to obtain a probability distribution from which the MI is calculated. In Fig. B.6, we plot the probability distribution inferred from various number of bins. The number of data points used here is 10^4. We learn from Fig. B.6 that for a finite number of data points there will be some numerical noise in the probability distribution inferred from the finite data set. This is more of an issue as the number of bins is increased. We blame this numerical noise in the probability distributions for causing the nonzero baselines in Fig. B.4.
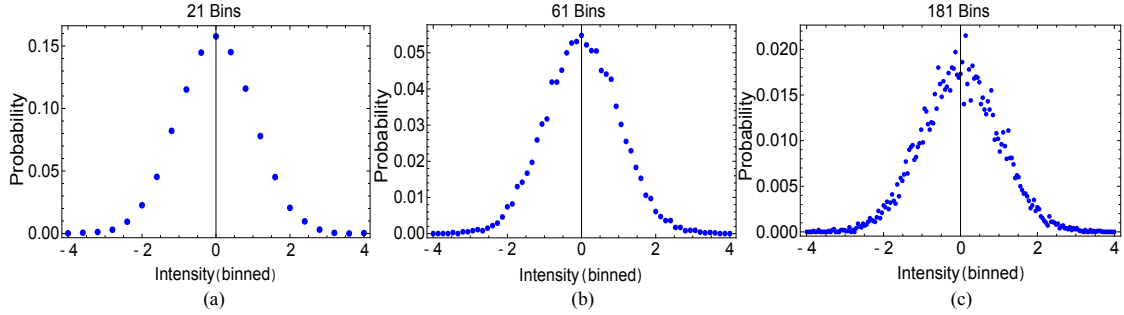
Figure B.6: Probability distributions of a single beam binned with 3 numbers of bins. (a) 21 bins, (b) 61 bins and (c) 181 bins. The number of points in the time trace is 10^4.
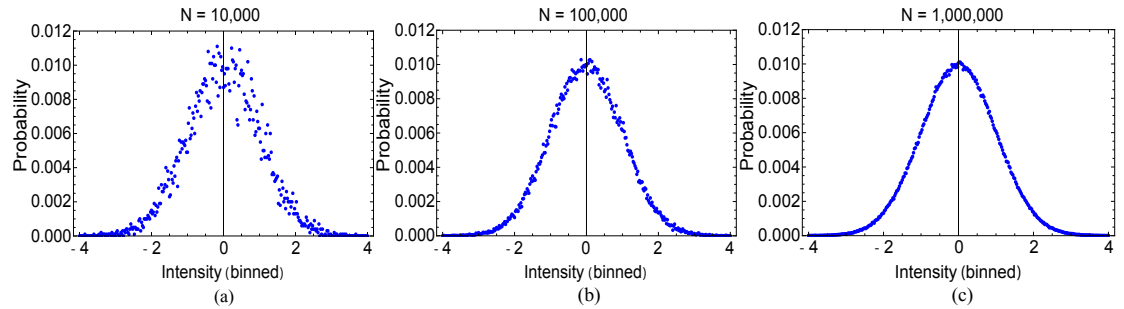
Figure B.7: Probability distributions of a single beam with 3 lengths of data sets. (a) 10^4 points, (b) 10^5 points and (c) 10^6 points. All binned with 361 bins.

To further illustrate this point, we also plot the probability distribution inferred from various length data sets in Fig. B.7. The number of bins (361) used here is large. Figure B.7 tells us that when the number of bins is large, one also needs to use large numbers of data points to reduce the numerical noise in the probability distributions inferred from the binning.

Repeating this for 20 realizations for each length of data set, we find that the information content of the distribution depends on the data set length. Doing an analytic calculation of the probability distribution by expressing the probabilities in each bin in terms of error functions, which are then evaluated numerically, one
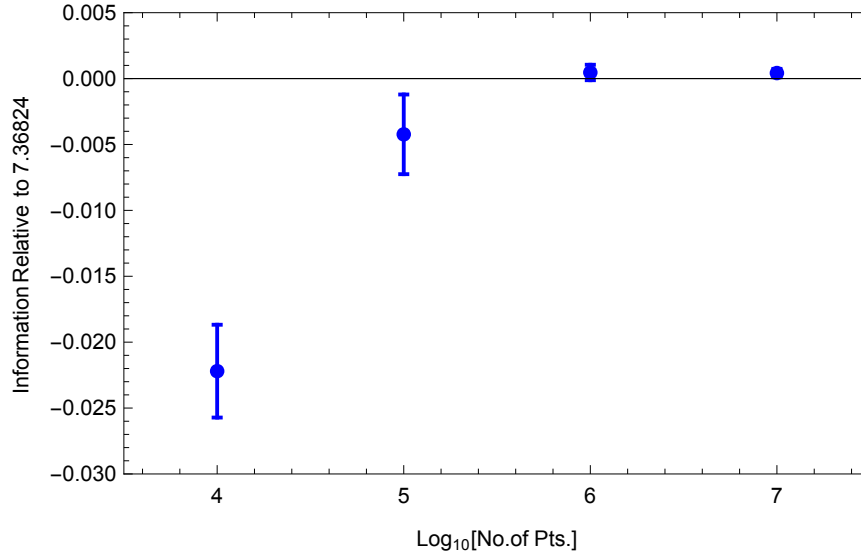
Figure B.8: Numerically derived information values as a function of the data set length, compared to the reference value of 7.36824 bits calculated analytically.

finds the information of this distribution (for this number of bins covering the range shown) should be 7.36824 bits. Figure B.8 shows the numerically derived information values as a function of the data set length, compared to this reference value. The length of the data sets used goes from 10^4 data points to 10^7 data points.

As one can see that, with larger data set length the mean value approaches the expected value derived analytically. The main point is that a finite number of data points in the time traces gives rise to noise in the inferred probability distribution. In Fig. B.8, it also appears that there is a small systematic shift from the mean value as the data set length decreases.

Now, with all the knowledge gained from the simulations, let us consider analyzing the real data from our experiment. The bottom line of choosing a number of bins to calculate the MI is to have enough of them to fully acquire all the MI (i.e., the bin width is sufficiently narrow to resolve the sub-shot-noise fluctuations) but
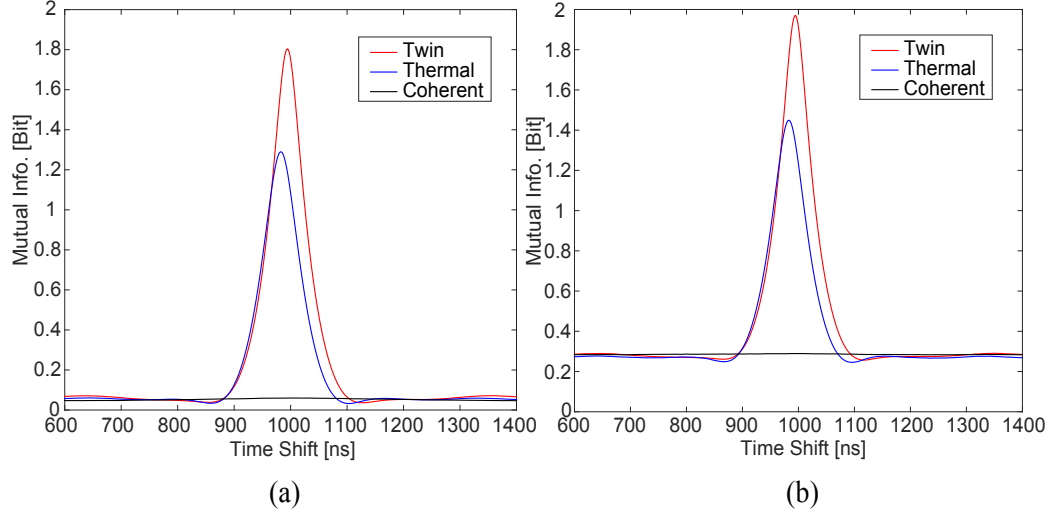
Figure B.9: Comparison of the calculations of MI with 2 numbers of bins for the twin, thermal and coherent beams. (a) 30 bins and (b) 100 bins.

not to introduce too much baseline. In Fig. 5.14, the MI are calculated with 100 bins, and we see the MI of the twin beams peaks at 1.97 bits with a baseline of 0.28 bits. To make a comparison, we recalculate the MI in the three cases with 30 bins and plot them alongside Fig. 5.14 in Fig. B.9. When calculated with 30 bins, we find that although the MI of the twin beams peaks at a lower value of 1.80, the value of its baseline is only 0.07, so the *net* (peak value minus the baseline value) MI is 1.73 bits, higher than the *net* MI of 1.69 bits calculated with 100 bins. Therefore, under current experimental conditions, using 30 bins to calculate the MI is sufficient for our purpose.

Bibliography

[1] P. A. Franken, A. E. Hill, C. W. Peters, and G. Weinreich. Generation of optical harmonics. *Phys. Rev. Lett.*, 7:118–119, Aug 1961. doi: 10.1103/PhysRevLett.7.118. URL `http://link.aps.org/doi/10.1103/PhysRevLett.7.118`.

[2] N. Bloembergen. Conservation laws in nonlinear optics. *J. Opt. Soc. Am.*, 70 (12):1429–1436, Dec 1980. doi: 10.1364/JOSA.70.001429. URL `http://www.osapublishing.org/abstract.cfm?URI=josa-70-12-1429`.

[3] J. F. Reintjes. *Nonlinear Optical Parametric Processes in Liquids and Gases.* Academic Press, Orlando, 1984.

[4] A. Yariv. *Quantum Electronics.* John Wiley and Sons, New York, 1989.

[5] Robert Boyd. *Nonlinear Optics 3rd Edition.* Academic Press, 2008.

[6] R. L. Abrams and R. C. Lind. Degenerate four-wave mixing in absorbing media. *Opt. Lett.*, 2(4):94–96, Apr 1978. doi: 10.1364/OL.2.000094. URL `http://ol.osa.org/abstract.cfm?URI=ol-2-4-94`.

[7] Joseph Nilsen and Amnon Yariv. Nearly degenerate four-wave mixing applied to optical filters. *Appl. Opt.*, 18(2):143–145, Jan 1979. doi: 10.1364/AO.18.000143. URL `http://ao.osa.org/abstract.cfm?URI=ao-18-2-143`.

[8] Tao-Yi Fu and Murray Sargent. Effects of signal detuning on phase conjugation. *Opt. Lett.*, 4(11):366–368, Nov 1979. doi: 10.1364/OL.4.000366. URL `http://ol.osa.org/abstract.cfm?URI=ol-4-11-366`.

[9] Robert W. Boyd, Michael G. Raymer, Paul Narum, and Donald J. Harter. Four-wave parametric interactions in a strongly driven two-level system. *Phys. Rev. A*, 24:411–423, Jul 1981. doi: 10.1103/PhysRevA.24.411. URL `http://link.aps.org/doi/10.1103/PhysRevA.24.411`.

[10] F. E. Becerra, R. T. Willis, S. L. Rolston, and L. A. Orozco. Nondegenerate four-wave mixing in rubidium vapor: The diamond configuration. *Phys. Rev. A*, 78:013834, Jul 2008. doi: 10.1103/PhysRevA.78.013834. URL `http://link.aps.org/doi/10.1103/PhysRevA.78.013834`.

[11] Alexander M. Akulshin, Russell J. McLean, Andrei I. Sidorov, and Peter Hannaford. Coherent and collimated blue light generated by four-wave mixing in rb vapour. *Opt. Express*, 17(25):22861–22870, Dec 2009. doi: 10.1364/OE.17.022861. URL `http://www.opticsexpress.org/abstract.cfm?URI=oe-17-25-22861`.

[12] M. D. Lukin, A. B. Matsko, M. Fleischhauer, and M. O. Scully. Quantum noise and correlations in resonantly enhanced wave mixing based on atomic coherence. *Phys. Rev. Lett.*, 82:1847–1850, Mar 1999. doi: 10.1103/PhysRevLett.82.1847. URL `http://link.aps.org/doi/10.1103/PhysRevLett.82.1847`.

[13] M. D. Lukin, P. R. Hemmer, and M. O. Scully. Resonant nonlinear optics in phase coherent media. In *Advances In Atomic, Molecular, and Optical Physics*, volume 42, pages 347–386. Academic Press, 2000. URL `http://dx.doi.org/10.1016/S1049-250X(08)60190-1`.

[14] C. F. McCormick, A. M. Marino, V. Boyer, and P. D. Lett. Strong low-frequency quantum correlations from a four-wave-mixing amplifier. *Phys. Rev. A*, 78:043816, Oct 2008. doi: 10.1103/PhysRevA.78.043816. URL `http://link.aps.org/doi/10.1103/PhysRevA.78.043816`.

[15] R. E. Slusher, L. Hollberg, B. Yurke, J. C. Mertz, and J. F. Valley. Squeezed states in optical cavities: A spontaneous-emission-noise limit. *Phys. Rev. A*, 31:3512–3515, May 1985. doi: 10.1103/PhysRevA.31.3512. URL `http://link.aps.org/doi/10.1103/PhysRevA.31.3512`.

[16] Mari W. Maeda, Prem Kumar, and Jeffrey H. Shapiro. Observation of squeezed noise produced by forward four-wave mixing in sodium vapor. *Opt. Lett.*, 12(3):161–163, Mar 1987. doi: 10.1364/OL.12.000161. URL `http://ol.osa.org/abstract.cfm?URI=ol-12-3-161`.

[17] M. T. L. Hsu, G. Hétet, A. Peng, C. C. Harb, H.-A. Bachor, M. T. Johnsson, J. J. Hope, P. K. Lam, A. Dantan, J. Cviklinski, A. Bramati, and M. Pinard. Effect of atomic noise on optical squeezing via polarization self-rotation in a thermal vapor cell. *Phys. Rev. A*, 73:023806, Feb 2006. doi: 10.1103/PhysRevA.73.023806. URL `http://link.aps.org/doi/10.1103/PhysRevA.73.023806`.

[18] D. M. Hope, H.-A. Bachor, P. J. Manson, D. E. McClelland, and P. T. H. Fisk. Observation of quadrature squeezing in a cavity-atom system. *Phys. Rev. A*, 46:R1181–R1184, Aug 1992. doi: 10.1103/PhysRevA.46.R1181. URL `http://link.aps.org/doi/10.1103/PhysRevA.46.R1181`.

[19] J. Ries, B. Brezger, and A. I. Lvovsky. Experimental vacuum squeezing in rubidium vapor via self-rotation. *Phys. Rev. A*, 68:025801, Aug 2003. doi: 10.1103/PhysRevA.68.025801. URL `http://link.aps.org/doi/10.1103/PhysRevA.68.025801`.

[20] L. A. Orozco, M. G. Raizen, Min Xiao, R. J. Brecha, and H. J. Kimble. Squeezed-state generation in optical bistability. *J. Opt. Soc. Am. B*, 4(10): 1490–1500, Oct 1987. doi: 10.1364/JOSAB.4.001490. URL `http://josab.osa.org/abstract.cfm?URI=josab-4-10-1490`.

[21] M. Vallet, M. Pinard, and G. Grynberg. Generation of twin photon beams in a ring four-wave mixing oscillator. *EPL (Europhysics Letters)*, 11(8):739, 1990. URL `http://stacks.iop.org/0295-5075/11/i=8/a=008`.

[22] V. Josse, A. Dantan, L. Vernac, A. Bramati, M. Pinard, and E. Giacobino. Polarization squeezing with cold atoms. *Phys. Rev. Lett.*, 91:103601, Sep 2003. doi: 10.1103/PhysRevLett.91.103601. URL `http://link.aps.org/doi/10.1103/PhysRevLett.91.103601`.

[23] C. F. McCormick, V. Boyer, E. Arimondo, and P. D. Lett. Strong relative intensity squeezing by four-wave mixing in rubidium vapor. *Opt. Lett.*, 32(2): 178–180, Jan 2007. doi: 10.1364/OL.32.000178. URL `http://ol.osa.org/abstract.cfm?URI=ol-32-2-178`.

[24] Neil V. Corzo, Quentin Glorieux, Alberto M. Marino, Jeremy B. Clark, Ryan T. Glasser, and Paul D. Lett. Rotation of the noise ellipse for squeezed vacuum light generated via four-wave mixing. *Phys. Rev. A*, 88:043836, Oct 2013. doi: 10.1103/PhysRevA.88.043836. URL `http://link.aps.org/doi/10.1103/PhysRevA.88.043836`.

[25] A. M. Marino, R. C. Pooser, V. Boyer, and P. D. Lett. Tunable delay of einstein-podolsky-rosen entanglement. *Nature*, 457:859–862, Feb 2009. doi: 10.1038/nature07751. URL `http://dx.doi.org/10.1038/nature07751`.

[26] Vincent Boyer, Alberto M. Marino, Raphael C. Pooser, and Paul D. Lett. Entangled images from four-wave mixing. *Science*, 321(5888):544–547, 2008. ISSN 0036-8075. doi: 10.1126/science.1158275. URL `http://science.sciencemag.org/content/321/5888/544`.

[27] Quentin Glorieux, Luca Guidoni, Samuel Guibal, Jean-Pierre Likforman, and Thomas Coudreau. Quantum correlations by four-wave mixing in an atomic vapor in a nonamplifying regime: Quantum beam splitter for photons. *Phys. Rev. A*, 84:053826, Nov 2011. doi: 10.1103/PhysRevA.84.053826. URL `http://link.aps.org/doi/10.1103/PhysRevA.84.053826`.

[28] Ulrich Vogl, Ryan T. Glasser, Quentin Glorieux, Jeremy B. Clark, Neil V. Corzo, and Paul D. Lett. Experimental characterization of gaussian quantum discord generated by four-wave mixing. *Phys. Rev. A*, 87:010101, Jan 2013. doi: 10.1103/PhysRevA.87.010101. URL `http://link.aps.org/doi/10.1103/PhysRevA.87.010101`.

[29] Jeremy B. Clark, Ryan T. Glasser, Quentin Glorieux, Ulrich Vogl, Tian Li, Kevin M. Jones, and Paul D. Lett. Quantum mutual information of an entangled state propagating through a fast-light medium. *Nat.Photon.*, 8:515–519, May 2014. doi: 10.1038/nphoton.2014.112. URL `http://dx.doi.org/10.1038/nphoton.2014.112`.

[30] Yin Cai, Jingliang Feng, Hailong Wang, Giulia Ferrini, Xinye Xu, Jietai Jing, and Nicolas Treps. Quantum-network generation based on four-wave mixing. *Phys. Rev. A*, 91:013843, Jan 2015. doi: 10.1103/PhysRevA.91.013843. URL `http://link.aps.org/doi/10.1103/PhysRevA.91.013843`.

[31] Hailong Wang, Zhan Zheng, Yaxian Wang, and Jietai Jing. Generation of tripartite entanglement from cascaded four-wave mixing processes. *Opt. Express*, 24(20):23459–23470, Oct 2016. doi: 10.1364/OE.24.023459. URL `http://www.opticsexpress.org/abstract.cfm?URI=oe-24-20-23459`.

[32] Ashok Kumar, Hayden Nunley, and A. M. Marino. Direct observation of spatial quantum correlations in the macroscopic regime. *arXiv.org*, 1611.06445v1: 1611.06445v1, Nov 2016.

[33] Hailong Wang, Leiming Cao, and Jietai Jing. Characterization of pairwise correlations from multiple quantum correlated beams generated from cascaded four-wave mixing processes. *Sci. Rep.*, 7:40410, Jan 2017. doi: 10.1038/10.1038/srep40410.

[34] A. MacRae, T. Brannan, R. Achal, and A. I. Lvovsky. Tomography of a high-purity narrowband photon from a transient atomic collective excitation. *Phys. Rev. Lett.*, 109:033601, Jul 2012. doi: 10.1103/PhysRevLett.109.033601. URL `http://link.aps.org/doi/10.1103/PhysRevLett.109.033601`.

[35] Jietai Jing, Cunjin Liu, Zhifan Zhou, Z. Y. Ou, and Weiping Zhang. Realization of a nonlinear interferometer with parametric amplifiers. *Applied Physics Letters*, 99(1):011110, 2011. doi: 10.1063/1.3606549. URL `http://dx.doi.org/10.1063/1.3606549`.

[36] Jia Kong, Jietai Jing, Hailong Wang, F. Hudelist, Cunjin Liu, and Weiping Zhang. Experimental investigation of the visibility dependence in a nonlinear interferometer using parametric amplifiers. *Applied Physics Letters*, 102(1): 011130, 2013. doi: 10.1063/1.4774380. URL `http://dx.doi.org/10.1063/1.4774380`.

[37] F. Hudelist, Jia Kong, Cunjin Liu, Jietai Jing, Z.Y. Ou, and Weiping Zhang. Quantum metrology with parametric amplifier-based photon correlation interferometers. *Nat.Comm.*, 5:3049, Jan 2014. doi: 10.1038/ncomms4049.

[38] J. A. Levenson, I. Abram, Th. Rivera, and Ph. Grangier. Reduction of quantum noise in optical parametric amplification. *J. Opt. Soc. Am. B*,

10(11):2233–2238, Nov 1993. doi: 10.1364/JOSAB.10.002233. URL `http://josab.osa.org/abstract.cfm?URI=josab-10-11-2233`.

[39] Carlton M. Caves. Quantum limits on noise in linear amplifiers. *Phys. Rev. D*, 26:1817–1839, Oct 1982. doi: 10.1103/PhysRevD.26.1817. URL `http://link.aps.org/doi/10.1103/PhysRevD.26.1817`.

[40] Z. Y. Ou, S. F. Pereira, and H. J. Kimble. Quantum noise reduction in optical amplification. *Phys. Rev. Lett.*, 70:3239–3242, May 1993. doi: 10.1103/PhysRevLett.70.3239. URL `http://link.aps.org/doi/10.1103/PhysRevLett.70.3239`.

[41] J. A. Levenson, I. Abram, T. Rivera, P. Fayolle, J. C. Garreau, and P. Grangier. Quantum optical cloning amplifier. *Phys. Rev. Lett.*, 70:267–270, Jan 1993. doi: 10.1103/PhysRevLett.70.267. URL `http://link.aps.org/doi/10.1103/PhysRevLett.70.267`.

[42] JA Levenson, I Abram, T Rivera, J C Garreau, and P Grangier. Quantum Optical Cloning Amplifier. *Physical Review Letters*, 70(3):3–6, 1993.

[43] K Bencheikh, C Simonneau, and J A Levenson. Cascaded Amplifying Quantum Optical Taps : A Robust Noiseless Optical Bus. *Physical Review Letters*, 78(1):34–37, 1996.

[44] Samuel L. Braunstein and Peter van Loock. Quantum information with continuous variables. *Rev. Mod. Phys.*, 77:513–577, Jun 2005. doi: 10.1103/RevModPhys.77.513. URL `http://link.aps.org/doi/10.1103/RevModPhys.77.513`.

[45] S Fossier, E Diamanti, T Debuisschert, R Tualle-Brouri, and P Grangier. Improvement of continuous-variable quantum key distribution systems by using optical preamplifiers. *Journal of Physics B: Atomic, Molecular and Optical Physics*, 42(11):114014, 2009. URL `http://stacks.iop.org/0953-4075/42/i=11/a=114014`.

[46] Sang-Kyung Choi, Michael Vasilyev, and Prem Kumar. Noiseless optical amplification of images. *Phys. Rev. Lett.*, 83:1938–1941, Sep 1999. doi: 10.1103/PhysRevLett.83.1938. URL `http://link.aps.org/doi/10.1103/PhysRevLett.83.1938`.

[47] Lantz, E. and Devaux, F. Numerical simulation of spatial fluctuations in parametric image amplification. *Eur. Phys. J. D*, 17(1):93–98, 2001. doi: 10.1007/s100530170042. URL `http://dx.doi.org/10.1007/s100530170042`.

[48] Alexis Mosset, Fabrice Devaux, and Eric Lantz. Spatially noiseless optical amplification of images. *Phys. Rev. Lett.*, 94:223603, Jun 2005. doi: 10.1103/PhysRevLett.94.223603. URL `http://link.aps.org/doi/10.1103/PhysRevLett.94.223603`.

[49] N. V. Corzo, A. M. Marino, K. M. Jones, and P. D. Lett. Noiseless optical amplifier operating on hundreds of spatial modes. *Phys. Rev. Lett.*, 109:043602, Jul 2012. doi: 10.1103/PhysRevLett.109.043602. URL `http://link.aps.org/doi/10.1103/PhysRevLett.109.043602`.

[50] C. J. McKinstrie and S. Radic. Phase-sensitive amplification in a fiber. *Opt. Express*, 12(20):4973–4979, Oct 2004. doi: 10.1364/OPEX.12.004973. URL `http://www.opticsexpress.org/abstract.cfm?URI=oe-12-20-4973`.

[51] Michael Vasilyev. Distributed phase-sensitive amplification. *Opt. Express*, 13 (19):7563–7571, Sep 2005. doi: 10.1364/OPEX.13.007563. URL `http://www.opticsexpress.org/abstract.cfm?URI=oe-13-19-7563`.

[52] R. Tang, P. Devgan, P. L. Voss, V. S. Grigoryan, and P. Kumar. In-line frequency-nondegenerate phase-sensitive fiber-optical parametric amplifier. *IEEE Photonics Technology Letters*, 17(9):1845–1847, Aug 2005.

[53] Renyong Tang, Jacob Lasri, Preetpaul S. Devgan, Vladimir Grigoryan, Prem Kumar, and Michael Vasilyev. Gain characteristics of a frequency non-degenerate phase-sensitive fiber-optic parametric amplifier with phase self-stabilized input. *Opt. Express*, 13(26):10483–10493, Dec 2005. doi: 10.1364/OPEX.13.010483. URL `http://www.opticsexpress.org/abstract.cfm?URI=oe-13-26-10483`.

[54] Renyong Tang, Preetpaul S. Devgan, Vladimir S. Grigoryan, Prem Kumar, and Michael Vasilyev. In-line phase-sensitive amplification of multi-channel cw signals based on frequency nondegenerate four-wave-mixing in fiber. *Opt. Express*, 16(12):9046–9053, Jun 2008. doi: 10.1364/OE.16.009046. URL `http://www.opticsexpress.org/abstract.cfm?URI=oe-16-12-9046`.

[55] Zhi Tong, C. J. McKinstrie, Carl Lundström, Magnus Karlsson, and Peter A. Andrekson. Noise performance of optical fiber transmission links that use non-degenerate cascaded phase-sensitive amplifiers. *Opt. Express*, 18(15):15426–15439, Jul 2010. doi: 10.1364/OE.18.015426. URL `http://www.opticsexpress.org/abstract.cfm?URI=oe-18-15-15426`.

[56] Z. Tong, C. Lundstrom, P. A. Andrekson, C. J. McKinstrie, M. Karlsson, D. J. Blessing, E. Tipsuwannakul, B. J. Puttman, H. Toda, and L. Gruner-Nielsen. Towards ultrasensitive optical links enabled by low-noise phase-sensitive amplifiers. *Nat.Photon.*, 5:430–436, Jul 2011. doi: 10.1038/nphoton.2011.79.

[57] Mosset, A., Devaux, F., Fanjoux, G., and Lantz, E. Direct experimental characterization of the bose-einstein distribution of spatial fluctuations of spontaneous parametric down-conversion. *Eur. Phys. J. D*, 28(3):447–451, 2004. doi: 10.1140/epjd/e2003-00323-2. URL `http://dx.doi.org/10.1140/epjd/e2003-00323-2`.

[58] Neil Corzo, Alberto M. Marino, Kevin M. Jones, and Paul D. Lett. Multi-spatial-mode single-beam quadrature squeezed states of light from four-wave mixing in hot rubidium vapor. *Opt. Express*, 19(22):21358–21369, Oct 2011. doi: 10.1364/OE.19.021358. URL `http://www.opticsexpress.org/abstract.cfm?URI=oe-19-22-21358`.

[59] John David Jackson. *Classical Electrodynamics*. Wiley, New York, 1962.

[60] Ryan M. Camacho, Michael V. Pack, John C. Howell, Aaron Schweinsberg, and Robert W. Boyd. Wide-bandwidth, tunable, multiple-pulse-width optical delays using slow light in cesium vapor. *Phys. Rev. Lett.*, 98:153601, Apr 2007. doi: 10.1103/PhysRevLett.98.153601. URL `http://link.aps.org/doi/10.1103/PhysRevLett.98.153601`.

[61] Lene Vestergaard Hau, S. E. Harris, Zachary Dutton, and Cyrus H. Behroozi. Light speed reduction to 17 metres per second in an ultracold atomic gas. *Nature*, 397:594–598, Feb 1999. doi: http://dx.doi.org/10.1038/17561. URL `http://dx.doi.org/10.1038/17561`.

[62] Ryan T. Glasser, Ulrich Vogl, and Paul D. Lett. Demonstration of images with negative group velocities. *Opt. Express*, 20(13):13702–13710, Jun 2012. doi: 10.1364/OE.20.013702. URL `http://www.opticsexpress.org/abstract.cfm?URI=oe-20-13-13702`.

[63] J. Keaveney, I. G. Hughes, A. Sargsyan, D. Sarkisyan, and C. S. Adams. Maximal refraction and superluminal propagation in a gaseous nanolayer. *Phys. Rev. Lett.*, 109:233001, Dec 2012. doi: 10.1103/PhysRevLett.109.233001. URL `http://link.aps.org/doi/10.1103/PhysRevLett.109.233001`.

[64] P. W. Milonni. *Fast Light, Slow Light and Left-Handed Light*. CRC Press, 2004.

[65] Michael D. Stenner, Daniel J. Gauthier, and Mark A. Neifeld. The speed of information in a "fast-light" optical medium. *Nature*, 425:695–698, Oct 2003. doi: 10.1038/nature02016. URL `http://dx.doi.org/10.1038/nature02016`.

[66] Daniel J. Gauthier and Robert W. Boyd. *Fast Light, Slow Light and Optical Precursors: What Does It All Mean?* Photonics Spectra, Jan, 2007.

[67] John S. Toll. Causality and the dispersion relation: Logical foundations. *Phys. Rev.*, 104:1760–1770, Dec 1956. doi: 10.1103/PhysRev.104.1760. URL `http://link.aps.org/doi/10.1103/PhysRev.104.1760`.

[68] A. Kuzmich, A. Dogariu, L. J. Wang, P. W. Milonni, and R. Y. Chiao. Signal velocity, causality, and quantum noise in superluminal light pulse propagation. *Phys. Rev. Lett.*, 86:3925–3929, Apr 2001. doi: 10.1103/PhysRevLett.86.3925. URL `http://link.aps.org/doi/10.1103/PhysRevLett.86.3925`.

[69] Horace P. Yuen. Two-photon coherent states of the radiation field. *Phys. Rev. A*, 13:2226–2243, Jun 1976. doi: 10.1103/PhysRevA.13.2226. URL `http://link.aps.org/doi/10.1103/PhysRevA.13.2226`.

[70] M. D. Reid and D. F. Walls. Quantum theory of nondegenerate four-wave mixing. *Phys. Rev. A*, 34:4929–4955, Dec 1986. doi: 10.1103/PhysRevA.34.4929. URL `http://link.aps.org/doi/10.1103/PhysRevA.34.4929`.

[71] Lu-Ming Duan, G. Giedke, J. I. Cirac, and P. Zoller. Inseparability criterion for continuous variable systems. *Phys. Rev. Lett.*, 84:2722–2725, Mar 2000. doi: 10.1103/PhysRevLett.84.2722. URL `http://link.aps.org/doi/10.1103/PhysRevLett.84.2722`.

[72] N. V. Corzo, A. M. Marino, K. M. Jones, and P. D. Lett. Noiseless optical amplifier operating on hundreds of spatial modes. *Phys. Rev. Lett.*, 109:043602, Jul 2012. doi: 10.1103/PhysRevLett.109.043602. URL `http://link.aps.org/doi/10.1103/PhysRevLett.109.043602`.

[73] J.-M. Liu. *Photonic Devices*. Cambridge University, 2005.

[74] Edward A. Whittaker, Manfred Gehrtz, and Gary C. Bjorklund. Residual amplitude modulation in laser electro-optic phase modulation. *J. Opt. Soc. Am. B*, 2(8):1320–1326, Aug 1985. doi: 10.1364/JOSAB.2.001320. URL `http://josab.osa.org/abstract.cfm?URI=josab-2-8-1320`.

[75] Benedict J. Cusack, Benjamin S. Sheard, Daniel A. Shaddock, Malcolm B. Gray, Ping Koy Lam, and Stan E. Whitcomb. Electro-optic modulator capable of generating simultaneous amplitude and phase modulations. *Appl. Opt.*, 43 (26):5079–5091, Sep 2004. doi: 10.1364/AO.43.005079. URL `http://ao.osa.org/abstract.cfm?URI=ao-43-26-5079`.

[76] D.M. Henderson and R.L. Abrams. A comparison of acoustooptic and electrooptic modulators at 10.6 microns. *Optics Communications*, 2(5):223 – 226, 1970. ISSN 0030-4018. doi: http://dx.doi.org/10.1016/0030-4018(70)90143-4. URL `http://www.sciencedirect.com/science/article/pii/0030401870901434`.

[77] Enbang Li, Jianquan Yao, Daoyin Yu, Jiangtao Xi, and Joe Chicharo. Optical phase shifting with acousto-optic devices. *Opt. Lett.*, 30(2):189–191, Jan 2005. doi: 10.1364/OL.30.000189. URL `http://ol.osa.org/abstract.cfm?URI=ol-30-2-189`.

[78] Neil Corzo, Alberto M. Marino, Kevin M. Jones, and Paul D. Lett. Multi-spatial-mode single-beam quadrature squeezed states of light from four-wave mixing in hot rubidium vapor. *Opt. Express*, 19(22):21358–21369, Oct 2011. doi: 10.1364/OE.19.021358. URL `http://www.opticsexpress.org/abstract.cfm?URI=oe-19-22-21358`.

[79] H. A. Bachor and T. C. Ralph. *A Guide to Experiments in Quantum Optics, Second Revised and Enlarged Edition.* Wiley-VCH, 2004.

[80] W. Yam, E. Davis, S. Ackley, M. Evans, and N. Mavalvala. Continuously tunable modulation scheme for precision control of optical cavities with variable detuning. *Opt. Lett.*, 40(15):3675–3678, Aug 2015. doi: 10.1364/OL.40.003675. URL `http://ol.osa.org/abstract.cfm?URI=ol-40-15-3675`.

[81] Michel Pich, Claude Par, and Pierre-Andr Blanger. Conversion of phase modulation to amplitude modulation using a phase conjugate mirror. *Optics Communications*, 65(2):146 – 150, 1988. ISSN 0030-4018. doi: http://dx.doi.org/10.1016/0030-4018(88)90287-8. URL `http://www.sciencedirect.com/science/article/pii/0030401888902878`.

[82] X. S. Yao. Phase-to-amplitude modulation conversion using brillouin selective sideband amplification. *IEEE Photonics Technology Letters*, 10(2):264–266, Feb 1998. ISSN 1041-1135. doi: 10.1109/68.655379.

[83] Kevin Croussore, Inwoong Kim, Cheolhwan Kim, Yan Han, and Guifang Li. Phase-and-amplitude regeneration of differential phase-shift keyed signals using a phase-sensitive amplifier. *Opt. Express*, 14(6):2085–2094, Mar 2006. doi: 10.1364/OE.14.002085. URL `http://www.opticsexpress.org/abstract.cfm?URI=oe-14-6-2085`.

[84] Aleš Kumpera, Rohit Malik, Abel Lorences-Riesgo, and Peter A. Andrekson. Parametric coherent receiver. *Opt. Express*, 23(10):12952–12964, May 2015. doi: 10.1364/OE.23.012952. URL `http://www.opticsexpress.org/abstract.cfm?URI=oe-23-10-12952`.

[85] G. Grynberg, A. Aspect, and C. Fabre. *Introduction to Quantum Optics: From the Semi-classical Approach to Quantized Light.* Cambridge University, 2010.

[86] *Nature Photonics Focus Issue: Quantum Optics, December 2009, Vol. 3, No. 12.* Nature Photonics, 2009.

[87] Carlton M. Caves. Quantum limits on noise in linear amplifiers. *Phys. Rev. D*, 26:1817–1839, Oct 1982. doi: 10.1103/PhysRevD.26.1817. URL `https://link.aps.org/doi/10.1103/PhysRevD.26.1817`.

[88] U. Leonhardt and H. Paul. High-Accuracy Optical Homodyne Detection with Low-Efficiency Detectors: "Preamplification" from Antisqueezing. *Physical Review Letters*, 72(26), 1994.

[89] Marcelo Marchiolli, Salomon Mizrahi, and Victor Dodonov. Signal-to-noise ratio of preamplified homodyne detection in quantum tomography. *Physical Review A*, 57(5):3885–3897, 1998. ISSN 1050-2947. doi: 10.1103/PhysRevA.57.3885.

[90] M. S. Kim. Enhancement of detection efficiencies in homodyne measurements: Comparison between squeezing signal fields and squeezing local oscillator fields. *Journal of Modern Optics*, 44(8):1437–1442, 1997. ISSN 0950-0340. doi: 10.1080/09500349708230748. URL `http://www.tandfonline.com/doi/abs/10.1080/09500349708230748`.

[91] Mashhood Ahmad, Shahid Qamar, and M. Suhail Zubairy. Quantum-state tomography using phase-sensitive amplification. *Phys. Rev. A*, 62:043814, Sep 2000. doi: 10.1103/PhysRevA.62.043814. URL `https://link.aps.org/doi/10.1103/PhysRevA.62.043814`.

[92] S Fossier, E Diamanti, T Debuisschert, R Tualle-Brouri, and P Grangier. Improvement of continuous-variable quantum key distribution systems by using optical preamplifiers. *Journal of Physics B: Atomic, Molecular and Optical Physics*, 42(11):114014—-, 2009. ISSN 0953-4075. doi: 10.1088/0953-4075/42/11/114014. URL `http://stacks.iop.org/0953-4075/42/i=11/a=114014`.

[93] J. Ph. Poizat and P. Grangier. Experimental Realization of a Quantum Optical Tap. *Physical Review Letters*, 70(3):271–274, 1993.

[94] K. Bencheikh, O. Lopez, I. Abram, and J. A. Levenson. Improvement of photodetection quantum efficiency by noiseless optical preamplification. *Applied Physics Letters*, 66(4):399, 1995. ISSN 00036951. doi: 10.1063/1.114201. URL `http://scitation.aip.org/content/aip/journal/apl/66/4/10.1063/1.114201`.

[95] Philippe Grangier, Juan Ariel Levenson, and Jean-Philippe Poizat. Quantum non-demolition measurements in optics. *Nature*, 396:537–542, 1998. ISSN 0036-8075. doi: 10.1038/25059. URL `http://dx.doi.org/10.1038/25059`.

[96] J. A. Levenson, I. Abram, Th. Rivera, and Ph. Grangier. Reduction of quantum noise in optical parametric amplification. *Journal of the Optical Society of America B*, 10(11):2233, nov 1993. ISSN 0740-3224. doi: 10.1364/JOSAB.10.002233. URL `http://www.opticsinfobase.org/abstract.cfm?URI=josab-10-11-2233`.

[97] J A Levenson, K Bencheikh, D J Lovering, P Vidakovic, and C Simonneau. Quantum noise in optical parametric amplification: a means to achieve noiseless optical functions. *Quantum and Semiclassical Optics: Journal of the European Optical Society Part B*, 9(2):221–237, 1999. ISSN 1355-5111. doi: 10.1088/1355-5111/9/2/009.

[98] P. Lam, T. Ralph, E. Huntington, and H.-A. Bachor. Noiseless Signal Amplification using Positive Electro-Optic Feedforward. *Physical Review Letters*, 79(8):1471–1474, 1997. ISSN 0031-9007. doi: 10.1103/PhysRevLett.79.1471.

[99] A.E. Ulanov, Dedorov, Pusjkina, Kurochkin, Timothy C. Ralph, and Ai. Lvovsky. Undoing the effect of loss on quantum entanglement.

Arxiv.Org/Abs/1504.0088, 9(11):1–8, 2015. ISSN 17494893. doi: 10.1038/ nphoton.2015.195. URL http://arxiv.org/abs/1504.0088.

[100] G. Alon, O.-K. Lim, A. Bhagwat, C.-H. Chen, M. Vasilyev, and P. Kumar. Amplification of a squeezed-quadrature using a cascaded traveling-wave phase-sensitive optical parametric amplifier. *the International Quantum Electronics Conference/Conference on Lasers and Electro-Optics (IQEC/CLEO) Pacific Rim, August 28-September 1, 2011, Sydney, Australia, paper 2260-CT-3*.

[101] C. F. McCormick, V. Boyer, E. Arimondo, and P. D. Lett. Strong relative intensity squeezing by four-wave mixing in rubidium vapor. *Optics letters*, 32(2):178–80, jan 2007. ISSN 0146-9592. URL http://www.ncbi.nlm.nih. gov/pubmed/17186056.

[102] Neil Corzo, Alberto M. Marino, Kevin M. Jones, and Paul D. Lett. Multi-spatial-mode single-beam quadrature squeezed states of light from four-wave mixing in hot rubidium vapor. *Opt. Express*, 19(22):21358–21369, Oct 2011. doi: 10.1364/OE.19.021358. URL http://www.opticsexpress.org/ abstract.cfm?URI=oe-19-22-21358.

[103] Tian Li, Brian E. Anderson, Travis Horrom, Kevin M. Jones, and Paul D. Lett. Effect of input phase modulation to a phase-sensitive optical amplifier. *Opt. Express*, 24(17):19871–19880, Aug 2016. doi: 10.1364/OE.24.019871. URL http://www.opticsexpress.org/abstract.cfm?URI=oe-24-17-19871.

[104] N. V. Corzo, A. M. Marino, K. M. Jones, and P. D. Lett. Noiseless Optical Amplifier Operating on Hundreds of Spatial Modes. *Physical Review Letters*, 109 (4):043602, jul 2012. ISSN 0031-9007. doi: 10.1103/PhysRevLett.109.043602. URL http://link.aps.org/doi/10.1103/PhysRevLett.109.043602.

[105] Jürgen Appel, Dallas Hoffman, Eden Figueroa, and A. I. Lvovsky. Electronic noise in optical homodyne tomography. *Phys. Rev. A*, 75:035802, Mar 2007. doi: 10.1103/PhysRevA.75.035802. URL http://link.aps.org/doi/ 10.1103/PhysRevA.75.035802.

[106] Yuishi Takeno, Mitsuyoshi Yukawa, Hidehiro Yonezawa, and Akira Furusawa. Observation of -9 db quadrature squeezing with improvement of phase stability in homodyne measurement. *Opt. Express*, 15(7):4321–4327, Apr 2007. doi: 10. 1364/OE.15.004321. URL http://www.opticsexpress.org/abstract.cfm? URI=oe-15-7-4321.

[107] R. W. Boyd and D. J. Gauthier. *Progress in Optics, edited by E. Wolf*, volume 43. Elsevier, Amsterdam, 2002.

[108] H. J. Kimble. The quantum internet. *Nature*, 453(7198):1023–1030, Jun 2008. URL http://dx.doi.org/10.1038/nature07127.

[109] John David Jackson. *Classical Electrodynamics, Third Edition*. WILEY, 1998.

[110] M. Born and E. Wolf. *Principles of Optics, 7th Edition.* Cambridge Univ. Press, 1999.

[111] C. G. B. Garrett and D. E. McCumber. Propagation of a gaussian light pulse through an anomalous dispersion medium. *Phys. Rev. A*, 1:305–313, Feb 1970. doi: 10.1103/PhysRevA.1.305. URL `https://link.aps.org/doi/10.1103/PhysRevA.1.305`.

[112] L. Brillouin. *Wave Propagation and Group Velocity.* Academic, New York, 1960.

[113] K. E. Oughstun and G. C. Sherman. *Electromagnetic Pulse Propagation in Causal Dielectrics.* Springer-Verlag, Berlin, 1994.

[114] R. Y. Chiao and A. M. Steinberg. *Progress in Optics, edited by E. Wolf*, volume 37. Elsevier, Amsterdam, 1997.

[115] Heejeong Jeong, Andrew M. C. Dawes, and Daniel J. Gauthier. Direct observation of optical precursors in a region of anomalous dispersion. *Phys. Rev. Lett.*, 96:143901, Apr 2006. doi: 10.1103/PhysRevLett.96.143901. URL `https://link.aps.org/doi/10.1103/PhysRevLett.96.143901`.

[116] J.C. Garrison, M.W. Mitchell, R.Y. Chiao, and E.L. Bolda. Superluminal signals: causal loop paradoxes revisited. *Physics Letters A*, 245(1):19 – 25, 1998. ISSN 0375-9601. doi: http://dx.doi.org/10.1016/S0375-9601(98)00381-8. URL `http://www.sciencedirect.com/science/article/pii/S0375960198003818`.

[117] M. D. Stenner, D. J. Gauthier, and M. A. Neifeld. The speed of information in a 'fast-light' optical medium. *Nature*, 425(6959):695–698, Oct 2003. URL `http://dx.doi.org/10.1038/nature02016`.

[118] Asher Peres and Daniel R. Terno. Quantum information and relativity theory. *Rev. Mod. Phys.*, 76:93–123, Jan 2004. doi: 10.1103/RevModPhys.76.93. URL `https://link.aps.org/doi/10.1103/RevModPhys.76.93`.

[119] Samuel L. Braunstein and Peter van Loock. Quantum information with continuous variables. *Rev. Mod. Phys.*, 77:513–577, Jun 2005. doi: 10.1103/RevModPhys.77.513. URL `https://link.aps.org/doi/10.1103/RevModPhys.77.513`.

[120] Christian Weedbrook, Stefano Pirandola, Raúl García-Patrón, Nicolas J. Cerf, Timothy C. Ralph, Jeffrey H. Shapiro, and Seth Lloyd. Gaussian quantum information. *Rev. Mod. Phys.*, 84:621–669, May 2012. doi: 10.1103/RevModPhys.84.621. URL `https://link.aps.org/doi/10.1103/RevModPhys.84.621`.

[121] A. I. Lvovsky, B. C. Sanders, and W. Tittel. Optical quantum memory. *Nat. Photon.*, 3(12):706–714, Dec 2009. URL `http://dx.doi.org/10.1038/nphoton.2009.231`.

[122] Robert W. Boyd. Slow and fast light: fundamentals and applications. *Journal of Modern Optics*, 56(18-19):1908–1915, 2009. doi: 10.1080/09500340903159495. URL `http://dx.doi.org/10.1080/09500340903159495`.

[123] Mark M. Wilde. *Quantum Information Theory*. Cambridge University Press, 2013. URL `https://doi.org/10.1017/CBO9781139525343`.

[124] Alessio Serafini, Fabrizio Illuminati, and Silvio De Siena. Symplectic invariants, entropic measures and correlations of gaussian states. *Journal of Physics B: Atomic, Molecular and Optical Physics*, 37(2):L21, 2004. URL `http://stacks.iop.org/0953-4075/37/i=2/a=L02`.

[125] Ulrich Vogl, Ryan T. Glasser, Quentin Glorieux, Jeremy B. Clark, Neil V. Corzo, and Paul D. Lett. Experimental characterization of gaussian quantum discord generated by four-wave mixing. *Phys. Rev. A*, 87:010101, Jan 2013. doi: 10.1103/PhysRevA.87.010101. URL `https://link.aps.org/doi/10.1103/PhysRevA.87.010101`.

[126] Ryan T. Glasser, Ulrich Vogl, and Paul D. Lett. Stimulated generation of superluminal light pulses via four-wave mixing. *Phys. Rev. Lett.*, 108:173902, Apr 2012. doi: 10.1103/PhysRevLett.108.173902. URL `https://link.aps.org/doi/10.1103/PhysRevLett.108.173902`.

[127] C. F. McCormick, A. M. Marino, V. Boyer, and P. D. Lett. Strong low-frequency quantum correlations from a four-wave-mixing amplifier. *Phys. Rev. A*, 78:043816, Oct 2008. doi: 10.1103/PhysRevA.78.043816. URL `http://link.aps.org/doi/10.1103/PhysRevA.78.043816`.

[128] M. Jasperse, L. D. Turner, and R. E. Scholten. Relative intensity squeezing by four-wave mixing with loss: an analytic model and experimental diagnostic. *Opt. Express*, 19(4):3765–3774, Feb 2011. doi: 10.1364/OE.19.003765. URL `http://www.opticsexpress.org/abstract.cfm?URI=oe-19-4-3765`.

[129] I.M. Gel'fand and A.M. Yaglom. Calculation of amount of information about a random function contained in another such function. *American Mathematical Society Translations: Series 2*, 12:199–246, 1957.